Universitat Autònoma de Barcelona

Stimulation Of Glioma-Associated Microglia/Macrophages Effector Phagocytic Synapse Towards Tumor Clearance In Glioma

Elena SAAVEDRA LÓPEZ

ADVERTIMENT. L'accés als continguts d'aquesta tesi queda condicionat a l'acceptació de les condicions d'ús establertes per la següent llicència Creative Commons: http://cat.creativecommons.org/?page_id=184

ADVERTENCIA. El acceso a los contenidos de esta tesis queda condicionado a la aceptación de las condiciones de uso establecidas por la siguiente licencia Creative Commons: http://es.creativecommons.org/blog/licencias/

WARNING. The access to the contents of this doctoral thesis it is limited to the acceptance of the use conditions set by the following Creative Commons license: https://creativecommons.org/licenses/?lang=en

UNIVERSITAT AUTÒNOMA DE BARCELONA

INSTITUT DE NEUROCIÈNCIES

Biochemistry and molecular Biology Dept.

Stimulation Of Glioma-Associated Microglia/Macrophages Effector Phagocytic Synapse Towards Tumor Clearance In Glioma.

Elena SAAVEDRA LÓPEZ

PhD. Director: Dr. Carlos Barcia González

PhD. Academic Tutor: Dr. José Aguilera Ávila

Doctor of Philosophy Research Thesis

PhD in Neuroscience

Cerdanyola del Vallès, Barcelona

June 17th, 2019

This thesis has been done in the Biochemistry and Molecular Biology Department (*Departament de Bioquímica y Biologia Molecular*) and in the *Institut de Neurociències* of the *Universitat Autònoma de Barcelona*, directed by

Dr. Carlos Barcia González

Elena Saavedra López

Dr. Carlos Barcia González

Cerdanyola del Vallès, 17th June 2019

Disclaimer

I hereby declare that this dissertation is my own original work, and although it has not been submitted before to any institution for assessment purposes, I have submitted some of the results here exposed for publication prospect.

Further, I have acknowledged all sources used and have cited these in the reference section.

_____

Elena Saavedra López

In Pozuelo de Alarcón, at 13th June 2019

Epigraph

“Do the best you can until you know better.

Then when you know better do better."

-Maya Angelou

Index

List of Tables

List of Figures

List of Appendices

List of Abbreviations

2D	Two Dimentional
3D	Three Dimensional
ANOVA	Analysis Of Variance
AP	Anteroposterior
APC	Antigen Presenting Cell
BBB	Blood-Brain Barrier
BDNF	Brain Derived Neurotrophic Factor
BSA	Bovine Serum Albumin
BV	Blood Vessel
CA	California
CD11b	Cluster Of Differentiation 11 B
CD16	Cluster Of Differentiation 16
CD16/32	Cluster Of Differentiation 16/32
CD163	Cluster Of Differentiation 163
CD28	Cluster Of Differentiation 28
CD3	Cluster Of Differentiation 3
CD32	Cluster Of Differentiation 32
CD4	Cluster Of Differentiation 4
CD47	Cluster Of Differentiation 47
CD8	Cluster Of Differentiation 8
CDK6	Cell Division Protein Kinase 6
CNS	Central Nervous System

CR3	Complement Receptor 3
CSF	Cerebrospinal Fluid
cSMAC	Central Supramolecular Activation Cluster
CT	Connecticut
CTLA-4	Cytotoxic T-Lymphocyte–Associated Antigen 4
D	Distal
DAB	Diaminobenzidine
DAG	Diacylglycerol
DAPI	4’,6-Diamino-2-Phenylindole
DMEM	Dulbecco's Modified Eagle Medium
DV	Dorsoventral
FcγR	Fc Gamma Receptor
FDA	Foods and Drugs Administration
FOXP3	Forkhead Box P3
GAMM	Glioma-Associated Microglia/Macrophage
GFAP	Glial Fibrillary Acidic Protein
HA	Hypercellular Area
HS	Horse Serum
I	Intermediate
IκB	Inhibitor of κB
Iba-1	Ionized Calcium-Binding Adapter Molecule 1
Ibu	Ibuprofen
ICAM-1	Intercellular Adhesion Molecule 1
IDH	Isocitrate Dehydrogenase

IFN-γ	Interferon-Gamma
IgG	Immunoglobulin G
IgM	Immunoglobulin M
IHC	Immunohistochemistry
IL-10	Interleukin-10
IL-4	Interleukin-4
iNOS	Inducible Nitric Oxide Synthase
IP_3	Inositol Triphosphate
ITAM	Immunoreceptor Tyrosine- Based Activation Motif
ITIM	Immunoreceptor Tyrosine- Based Inhibition Motif
LFA-1	Lymphocyte Function-Associated Antigen 1
LPS	Lipopolysaccharide
M1	Classically Activated Macrophages
M2	Alternatively Activated Macrophages
MA	Massachussetts
Mac-1	Macrophage-1 Antigen
MASP	Mannose-Binding Lectin-Associated Serin Protease
MBL	Mannose-Binding Lectin
MD	Maryland
MHC	Major Histocompatibility Complex
MHCII	Major Histocompatibility Complex II
ML	Mediolateral
MO	Missouri
MTOC	Microtubule-Organizing Center

NF	Necrotic Focus
NF- κB	Nuclear Factor -Kappa B
NIH	National Institute Of Health
OI	Organosomatic Index
OX42	Rat Cluster Of Differentiation 11b/C
P	Proximal
P/S	Penicillin/Streptomycin
PBS	Phosphate-Buffered Saline
PD-1	Programmed Death 1
PD-L1	Programmed Death 1 Ligand
PFA	Paraformaldehyde
PG	Prostaglandin
PIP_2	Phosphatidylinositol Biphosphate
PLC γ	Phospholipase C gamma
PLD	Phospholipase D
PLL	Poly-L-Lysine
PP	Pseudopalisade
pSMAC	Peripheral Supramolecular Activation Cluster
PtdSer	Phosphatidyl Serine
RNA	Ribonucleic Acid
rpm	Revolutions Per Minute
RPMI	Roswell Park Memorial Institute
SIRP alpha	Signal-Regulatory Protein A
T cells	Thymus-Derived Lymphocytes

T lymphocytes	Thymus-Derived Lymphocytes
TCR	Thymus-Derived Cell Receptor
TNFα	Tumor Necrosis Factor Alpha
TP	Tumor Parenchyma
UAB	Universitat Autònoma de Barcelona
UK	United Kingdom
USA	United States Of America
UV	Ultraviolet

Summary

Glioblastoma (GBM) is the most aggressive form of glioma and currently has no cure. Given that around 30% of the cells within the tumor are microglia/macrophages (glioma- associated microglia/macrophages or GAMM from now on), we decided to study them in order to shed light in possible future immunotherapies.

The first discovery during this investigation was the presence of GAMM in pseudopalisades (PPs) of human GBM. These structures are thought to be very important in the contribution of the tumor invasiveness, therefore the knowledge of the role of GAMMs here might be crucial. Particularly, GAMMs were found to be traveling through the PPs towards the necrotic focus, contrasting with the tumor cells. Moreover, the myeloid cells seem to gain cellular persistence with the hypoxic gradient and travel in a haptotactic manner using the gradient of glioma cells as a cue. When they reach the necrotic focus, they shift their phenotype and phagocytose tumor material, including $GFAP^+$ fragments and nuclei.

Secondly, by means of cell cultures we achieved to translocate p65 NF-κB and promote phagocytosis of tumor glioma cells (C6) by primary microglia. Moreover, using cell lines (BV-2 and GL261) we described the putative steps of phagocytosis of glioma cells and the distribution of some receptors (CD11b and CD16/32) involved in the process of phagocytosis. Importantly, the distribution of Iba-1 in interacting GAMMs was also defined in the animal models.

Finally, we tested two immunotherapeutic strategies in an immunocompetent GBM animal model (C57/BL6 intracraneally inoculated with GL261 cells), and discovered that both immunotherapies have different outcomes: while CD47 neutralizing antibody seemed to be non-effective, neutralizing SIRP1α had a beneficial outcome. This way, anti-CD47 treated animals did not show an increase on survival rate compared to control groups; but they showed decreased bodyweight throughout the experiment, suggesting that the therapy had some systemic side effects. On the other hand, blocking SIRP1α allowed the increase of the bodyweight of the animals throughout the experiment, and decreased the cellularity of the tumor core by increasing the phagocytic activity of GAMM at the peripheral area of tumor invasion without interfering in their infiltration capacity.

In all, this thesis contributes to a better understanding of the role of GAMMs in GBM and the intrinsic phagocytic capacity they can play, possibly helping in the development of immunotherapeutic tools to fight this fatal tumor.

Resumen

Glioblastoma (GBM) es el tumor más agresivo dentro de la clasificación de gliomas y actualmente no tiene cura. Dado que hasta el 30% de las células en GBM son microglia y macrófagos (GAMMs desde ahora, por sus siglas en ingles), decidimos estudiarlos para ayudar en el diseño de posibles futuras inmunoterapias.

El primer gran descubrimiento de esta tesis es la presencia de GAMM en las pseudo-empalizadas (PPs, por sus siglas en inglés) in GBM humano. Estas estructuras se cree que pueden contribuir a la capacidad de invasión del tumor, por lo que el papel de los GAMM en este microambiente puede ser crucial. En concreto, describimos que los GAMMs viajan a través de las PPs hacia su foco necrótico, de forma inversa a las células tumorales. Además, los GAMMs parecen ganar persistencia celular, es decir que viajan de forma directa, bajo las condiciones hipóxicas de las PPs y se desplazan de manera haptotáctica, siendo las fibras $GFAP^+$ su sustrato para avanzar. Al llegar al área necrótica, cambian su fenotipo y fagocitan material del tumor, incluyendo fragmentos $GFAP^+$ y núcleos celulares.

En segundo lugar, en cultivos celulares hemos inducido la translocación al núcleo de NF-κB p65 para aumentar la facogitosis de células de glioma (C6) por parte de microglia primaria de rata. Además, por medio de líneas celulares inmortalizadas (BV-2 y GL261) hemos descrito una serie de supuestos pasos que pueden ser importantes en el proceso de fagocitosis, así como la distribución de determinados receptores (CD11b y CD16/32) durante estas etapas. Asimismo, describimos la distribución de Iba-1 en los procesos de interacción fagocítica en modelos animales de glioma.

Por último, hemos probado dos estrategias de inmunoterapia en un modelo murino de GBM (ratones C57/BL6 inyectados con células GL261 intracranealmente), descubriendo que estas inmunoterapias tienen efectos distintos: mientras la neutralización de CD47 pareció no ser efectiva, neutralizar SIRP1α parece ser beneficioso. Así, los animales del grupo denominado CD47 no mostraban un aumento de su supervivencia comparados con los ratones control, incluso mostraban pérdida de peso, indicador de que la terapia pueda producir efectos secundarios sistémicos. Por otro lado, el bloqueo de SIRP permitió el incremento del peso corporal de los animales durante el experimento, y, de hecho, disminuyó el número de células en el centro del tumor incrementando la capacidad fagocítica de los GAMMs en las zonas periféricas de invasión, sin interferir en su capacidad de infiltrarse en el tumor.

En conclusión, esta tesis contribuye a una mejor comprensión de la función de los GAMMs en GBM y su capacidad fagocítica intrínseca, posiblemente ayudando al desarrollo de nuevas herramientas terapéuticas para luchar contra este tumor.

Acknowledgements

Of course I could not end this process without expressing my gratitude to my thesis director Dr. Carlos Barcia. I cannot imagine having achieved the end of this doctoral thesis without you in the role of director, knowing when to take things seriously and when to joke. Thank you for everything during these six long years: your guidance, your patience, your sageness, your always positive attitude even at what seemed bad results, for the correct proverbs at the correct moment, for almost even encouraging me to do under-cover experiments, for the opportunity to go to scientific meetings. But above all, thank you for trusting me, for instance on the establishment of scientific contacts (Paris, IMPETUX), and on the other hand for letting me develop my own ideas, for listening to them even if they sounded crazy. You know what I mean: microglial intelligence, *micrabglia*, microglial digestion… I really appreciate it. Thank you.

I would like to thank Dr. Jose Aguilera for accepting being my tutor and therefore making this thesis possible, and the members of the follow-up commission: Dr. Beatriz Almolda, Dr. Víctor Yuste and Dr. Cristina Muñoz; for the counseling year after year as well as the appreciation of my hard work.

Thank you Dr. Mª Ángeles Carrillo – de Sauvage and Dr. Carole Escartin for those three months at MirCen and what comprised later on. You worked hard with all the paperwork in order for me to go, I believe it was worth it. I really appreciate your effort and your trust. I would also like to thank my Parisian friends, especially Laurene Abjean for all she happily taught me, Francesco Gubinelli for the good moments shared and Charlotte Duwat for her smile and the Iba-1/Pu.1 protocol. Thanks to Audrey, Anastasie, Camille, PA, the Paulines, Mélissa, Marianne, Océane, Clémence, Susanne and Kelly for your smiles and always making me feel like I belonged there. To Ferrán for those happy mornings at the Colegio de España.

I would also like to thank all the people of the Hospital General Universitario de Valencia who was involved in the extraction, processing and diagnosis of the human tissue used in this thesis, as well as Arnau Farré from IMPETUX for his full disposal for the optical tweezers experiments.

I am extraordinarily grateful to my colleagues and loving friends Paola and Meritxell. We have had very fun moments in the lab, some scientific, others not so much, like the water war (with Meri), or the insect in the box (Paola). Thank you for all those coffee breaks at the sun, and especially for your support when I needed it, inside as well as outside the lab: for lodging me when I didn't have a home, for transporting my things when I found one. I will be ever grateful.

I would also like to thank GP for all the insightful comments at the weekly lab meetings, for always being there when needed, for your always kind words. To the rest of the colleagues in the department and Institut, thanks: Cris, for her guidance and support even if sometimes was in an angry manner; Anita, although we established a closer relationship once you were gone; Abel, for always including me in the plans and for the parties (especially the one in 2015); Arantxa, especially

for the shared workouts; to Míriam, Raquel, Dolo, Carlos, Paula and other past members, such as Montse, Elsa, Santi, Amaia, Vanessa and Victoria (Viztoria) for the happiness, support, the afterworks and the week-ends shared. Thanks to the students that without knowing so have taught me so much, especially Leire, but also Laura, Marta (even though you were not my student), Alba, Cris, Ana or even Rafaela. Thanks to other people in the INc, such as Mar Castillo and Núria Barba, always so helpful; Roser Bastida, for making us participate (and win) at the activities; Quintana's Lab (Machu, Pati and Fabien especially) for the help with the in vivo part of this thesis; and other friends like David, Tatiana, Natàlia, Alba and Guillem.

I cannot finish without acknowledging and thanking Clara, a fundamental pillar in my life since the beginning of my chapter in Barcelona, for that trip to Carcassonne just when I needed it. I extend my gratitude to Cesc, Pablo, and Lidia. To my great friends Irina, Anya and Leia, for your support when I was injured and also the intense moments we have had: trips, conversations…. Thank you Beto and Efraín: some lessons are not teached at work. For the same reason I would like to thank my aikido family, especially the veterans Eva, Antonia, Sebastián and David, the *sensei*. To Lourdes and Judit for your support during these last months, always cheering for me whenever I finished a figure or a section of the manuscript.

To my friends from Madrid: the ones from University (Sofía, Marta, Vir, Dani, Noush, Elena, Ana), for listening to me whenever I need it and always being there for me; and the ones from School (Mariano, Juan, Adriana, Pati, Inés, Isa, Elena, Carmen, Ani) for always being available and ready to meet up whenever I go back.

To my lovely Valencian friends: Mire, Carol, Cris, Álvar. Lauri, although not from Valencia you are included here. Thank you all for your support and for listening to me since the day I met you. I believe it was love at first sight. Thank you also for those crazy weekends whenever I visit you.

But the people I am most grateful to are my family. I thank my *abuelita* Mª Jesús for believing in me and always push me to improve; and my aunts, uncles and cousins, as well as the ones that have already passed away, I wouldn't be who I am without them. I am extremely grateful to my beloved siblings Marina and Adrián, for the support and courage transmitted, for believing in me without doubt, for trusting me; I love you so much. Thank you, Lulu, for your comprehension, your respect and for taking me to once-in-a-life experiences, including the day night you sprained your ankle, and making me godmother of the newborn Ciro. I love you too. Above all, I thank my parents María Jesús López Suso and Luis Saavedra del Río, for always encouraging me to be a better person in every aspect of my life. Thank you for teaching me, for the example you have given me, for all the financial and moral support. Thanks from the bottom of my heart, I love you.

As my wise sister would say, and in the recent years my brother does so too: "Gracias a todos". Thank you all.

Introduction

Glioma: Origin And Prognosis

Gliomas are the most common tumors in the central nervous system (CNS) (2,3). Although they comprise a variety of tumor types proper from the CNS, regarding the histopathological and molecular characteristics they can be classified in two main groups: diffuse gliomas, which grow infiltrating in the CNS parenchyma and are the most frequent intrinsic CNS neoplasms; and non-diffuse gliomas, which have not yet been accurately defined (2). Diffuse gliomas often appear in the brain cortex, and their histological features divide them into four categories, namely astrocytoma, oligoastrocytoma, oligodendroglioma and glioblastoma (GBM) (being this the most aggressive form of glioma, grade IV) which can be re-divided into categories by the genetic testing, as some genes such as isocitrate dehydrogenase (IDH)-1, IDH2 or 1p/19q can be present (mutated or not) or absent (2–4). Nevertheless, since these classifications are currently under debate and the samples used in the studies in this thesis were categorized before this new glioma classification, we do not discriminate the genetic features, and rely mostly on the histological ones, as Histology is still the major tool to define the tumors' categories (2). For instance, grade IV glioma (GBM) samples expose typical features namely mitotic activity, vascular proliferation and glomeruloid vessels, cellular anaplasia, necrosis and pseudopalisading areas (5,6). Despite the suspected importance of the latter for tumor progression, these areas are currently understudied, and the most detailed article about these necrotic pseudopalisades (PPs) suggests that they are constituted by tumor cells which escape from the central blood vessel found in these regions (7). The authors hypothesize that the blood flow in the vessel is suddenly interrupted, the tumor cells sense this abnormality and escape from the hypoxic conditions, invading new areas. In this way, PPs contribute to tumor incursion; but this study was published without detailed regard to immune cells, which were thought not to be present. In the first part of this thesis, we studied the biopsies from six human GBM patients, and together with some in vitro assays, we shed light upon the immune component, especially microglia and macrophages, in this feature which only the most aggressive gliomas display (5,6).

Although glioma origin is starting to be elucidated, for a recent article determined neural stem cells in the subventricular zone carrying genetic mutations may be the cells from which the tumor originates (8); GBM is currently incurable and patients live about one year after diagnosis with no standardized treatment (9). Patients undergo a therapy based on a combination of a maximal surgical resection, radiotherapy and chemotherapy mostly with temozolomide (3,10). However, some cancer cells are characterized for being radio and chemo resistant (11,12). It was already known that GBM cells communicate through the sending of microvesicles with RNA (13), but recently it has been demonstrated that apoptotic cancerous cells are able to send spliceasomes through extracellular vesicles to non-dying tumoral cells, making them more resistant to treatments (14). Moreover, at a molecular level, it has been described a modification of SUMO1 which stabilizes CDK6 protein, driving them through G1/S transition, that is, mitosis (15). For these reasons the prognosis is of over a year, as the tumor oftentimes returns (3,4,10). Although some professionals still blame this relapse on surgical resection of the tumor (16), whatever the reason is, it remains clear that current treatments are not effective, hence to find a new way to fight the tumor is crucial.

Immunotherapy As A Promising Option

In this regard, increasing numbers of published reports suggest that immunotherapy could be a very promising treatment for brain cancer. Especially in gliomas, in order to increase the effectiveness and efficiency of the immune response against the tumor while limiting autoimmune toxicity, it is necessary to understand the immunological characteristics of the brain in healthy and tumorigenic conditions, as well as the microenvironment created by the tumor. Hereof it is widely accepted that the CNS is immune privileged, or even immune-isolated, giving almost all the credit to the Blood-Brain-Barrier (BBB) (17,18). However, it is noteworthy that many authors have misinterpreted and miscited the first articles describing different stainings and lack of them in the brain (19,20) ; work carried out by Ehrlich, Goldmann and others. Those who erred on the citations, talk about a BBB that Ehrlich himself he denied, as he could not confirm the existence of a barrier in the brain different from any others found in other organs (21); while Goldmann was also doubtful of his own work as he

might not have used the correct settings in his experiments (22). Moreover, recently, it has been once again demonstrated that the human brain is not as isolated as popularly believed, as functional lymphatic vessels are present, transporting a variety of substances such as antigens and immune cells (23). This system has been called glymphatic system, and it had already been described in mice (24,25) and rats (25). In addition, misfolded proteins and antigens can drain mainly by diffusion, from the cerebrospinal fluid (CSF) to cervical lymph nodes (26,27), where antigen presenting cells can utilize them to activate thymus-derived lymphocytes (T cells) (28). Furthermore, diverse immune cells are able to extravasate from blood vessels and infiltrate the brain, especially in a diseased CNS (29–32). Studies on glioma specify that microglia/macrophages account for up to 30% of the total cell density in the tumor (33,34), while other immune cell types such as T lymphocytes, are less common but also essential, as their presence correlates with the malignancy of the tumor (35) .

Thus, microglia/macrophages could be an interesting target to tackle tumor expansion. These cells are able to change phenotypes from pro-inflammatory to immunosuppressor and vice versa. First off, microglial cells are immune cells present in the brain since the embryonic development: they are derived from the yolk sac and they arrive to the CNS as the resident macrophages (36,37). In humans, at 4.5 weeks of gestation can already be detected in the brain (38), while in mice they start their settlement at embryonic days 8 to 10 (39). Once in the brain, they are constantly surveying the brain parenchyma in the search of damage and dangerous antigens, by the constant movement of their processes (40). Additionally, we can find in the brain peripheral macrophages, which are present in case of brain injury when peripheral immune cells are summoned to the CNS and skewed (34,37,41) through the release of diverse molecules such as interferon-gamma (IFN-γ) or interleukin-4 (IL-4) (42–44). Blood monocytes are able to extravasate and then differentiate to become monocyte-derived brain macrophages (41). Once in the brain, they receive the stimuli like the local microglia, hence polarizing identically, often being indistinguishable one from another by surface markers (45–47), although not genetically, as pointed out in humans (48) or in mice (45,49). Despite this, when something harmful is detected, microglia and macrophages become activated, they change their morphology and furthermore they initiate an immune response (50–53).

They can react by producing a variety of cytokines, chemokines, free radicals and trophic factors, such as IFN-γ, nitric oxide, brain derived neurotrophic factor (BDNF) or tumor necrosis factor alpha (TNFα); which have different functions, from attracting or repelling other cells (51,53–55), to directly damaging bystander cells (56). Essentially, the response the cells produce depends on the stimuli they receive, and the different stimuli can result in a variety of different phenotypes originally described in vitro, which go from the classically activated phenotype (M1), to the alternatively activated phenotype, or M2 (44,57). Albeit simplistic, this M1-M2 classification is very useful, especially when studying tumors, as M1 are considered to be anti-tumoral and M2 to be pro-tumoral. However, we must bear in mind that microglia and macrophages in physiological conditions may receive several and even contradictory stimuli, and thus what started to be in vitro a dichotomic classification, has ended up being a continuum in the actual tissue, where it is now often to talk about M1 or M2 spectrum phenotype.

By the administration of IL-4 and -10 M2 cells release anti-inflammatory cytokines and are able to remodel the tissue they are in and repair it, for example with their angiogenic capacity (58). As the molecules inducing each of these phenotypes are different, the signaling cascades triggered are also different. For instance, M2 cells activate the signaling pathway of the p50/p50 NF-κB homodimer (59), reaching the pro-tumoral or anti-inflammatory phenotype, expressing markers such as CD163 (60). This is especially interesting in tumors, as this kind of cells can be found in hypoxic areas and the tissue around blood vessels (61). In glioma specifically, blood vessels are utilized by tumor cells to invade new areas by co-option, displacing the astrocytes' endfeet and travelling along the endothelium (62). Thus, M2-spectrum cells might facilitate tumor expansion.

In contrast with this, M1 cells were described when being activated with IFN- γ and/or lipopolysaccharide (LPS) (63), a compound naturally found on the external membrane of gram negative bacteria (64). LPS can activate the canonical p65/p50 NF- κB pathway (65), in which the heterodimer translocates to the nucleus, finally signaling nitrate production, phagocytosis, etc. (66), and expressing proteins essential for these functions, namely iNOS or HLA-DR (63), a human form of major histocompatibility complex II (MHCII). In this manner, M1-spectrum function is pro-inflammatory, as this cells are able to produce toxicity, cell death and the forenamed

phagocytosis (67–70), which is important for the elimination of cells, including damaged (46,56) or tumorigenic (70,71); and the contribution to repairing the tissue, as phagocytosis of debris is necessary for the protection of healthy undamaged cells (reviewed in (72,73)).

Deciphering Phagocytosis

Logically, microglia and macrophages must first contact their target, and once it is recognized as a potential threat (for example because it is opsonized), they must bind it and phagocytose it. Therefore, these microglia-target contacts, also described as gliapses (74), are crucial to understand in order to be able to potentiate them and make them more effective; or inhibit them, depending on the desired result. For instance, in the tumorigenic context, it would be ideal if we could promote the phagocytic contacts between microglia/macrophages and tumor cells. Generally, in the gliapses that end in phagocytosis, the receptors of the phagocyte are used to categorize the phagocytic processes.

This way, molecularly, the most studied type of phagocytosis is the one mediated by fragment-crystallizable γ receptors (FcγR) (**Figure 1 A**). Four classes of FcγR exist: FcγR I, II (e.g. CD32), III (e.g. CD16) and FcγR IV, all of them being opsonic receptors (75–79). For this kind of phagocytosis to take place, the first thing happens is the binding to the IgG on the opsonized target (75–77,79–81). Next, FcγR cluster near the kinases and if the overall signals indicate engulfment must take place, then this would be the ultimate step (75,78,82). Receptor clustering triggers the signaling cascade which, among other things, provokes the polymerization of actin (83–85) and the formation of the phagocytic synapse, where we can find, for example, FcγR I or FcγR II forming “activation rings” (78,79), resembling the supramolecular activation clusters (SMAC) described in T cells , when establishing phagocytic synapses with beads, bacteria and opsonized glass slides (78,86). Moreover, FcγRs at the phagocytic synapse are sometimes coupled with integrins and receptors, like FcγR III, that binds the integrin CD11b (demonstrated in neutrophils and fibroblasts in (87,88)), or FcγR I, which is associated to Signal-regulatory protein alpha (SIRPα) (78). When activated, immunoreceptor tyrosine- based activation motif (ITAM) of the

FcγRs is exposed (77,89) and, as well as the γ chain, it is phosphorylated by proteins of the Src family (77), namely Lyn (90), Hck (90) and Fgr (91,92). In order to internalize the phagosome, Syk family members are activated (77,93–95) and recruit phospholipase C γ (PLCγ) (77,89,96), enzyme which catalizes the hidrolization of phosphatidylinositol biphosphate (PIP_2) into diacylglycerol (DAG) and inositol triphosphate (IP_3), what contributes to actin clearance, an essential step in the phagocytosis of large molecules (77,81). In macrophages specifically, phospholipase D (PLD) has also been described to have an essential part on the formation of the phagocytic cup (97,98).

Importantly, an immunoreceptor tyrosine- based inhibition motif (ITIM) is also present on FcγR II (76,77), and on the afore-mentioned SIRPα (78,89), and when phosphorylated, it activates phosphatases which prevent phagocytosis, for example by inhibiting myosin II (77), which is normally found in the phagocytic synapse (99). In summary, FcγR phosphorylation can promote (FcγR I, III and IV in mice; and FcγR IA, IIA and IIIA (76)) or halt (FcγR IIB) phagocytosis, depending on the receptors involved.

In addition, Dectin-1 has been described to be a phagocytic receptor when phagocytosing fungi (55) (**Figure 1 B**). Bearing a motif similar to ITAM in FcγR, Dectin-1 also signals through the Src kinases (Syk is activated) and finally provokes actin remodeling in the cytoskeleton and phagocytosis (55).

Finally, we find complement-mediated phagocytosis (**Figure 1 C**). Three different pathways exist: the classical pathway, the alternative pathway, and the lectin pathway (reviewed in (100–103)). All of them require the C3 protein, which generates C3a and C3b when activated by the C3 convertases (100,102,103). C3b can then do several things: to opsonize the target, to activate the C3 convertase and amplify the signal, and to activate the C5 convertases which turn C5 into C5a and C5b (100,102,103). C5a contributes to chemotaxis (101–103); while C5b associates with other complement proteins to create pores in the membrane, what can provoke target cell lysis (103,104). The classical pathway can be activated by apoptotic cells and usually requires IgG or IgM to bind C1q before the whole complement cascade is activated (102). The alternative pathway occurs by direct binding to pathogens, normally useful for amplification of the other pathways, as the master molecule of the complement, C3, is created and cleaved again (102,103). The lectin pathway

requires mannose to bind lectin in order to activate the Mannose-binding lectin (MLB)-associated serin proteases (MASP) (102,103). Although there are several types of MASP, they end up with the formation of C3 convertases (102), therefore also activating C3 and creating C3a and C3b. Importantly, opsonic C3b can be inactivated by healthy host cells, while some damaged cells are not able to do so, and consequently the complement stays attached to the target (103). To interact with opsonic complement proteins, microglia and macrophages also express other complement receptors, like Macrophage-1 antigen (Mac-1 or CR3) (103), which is formed by two integrins: the afore-mentioned CD11b integrin and CD18 (102). When they become activated, a signaling cascade involving Rap1 ends with the conformational change of the receptors, increasing their affinity for the ligand (77). Interestingly, CR3 and FcγR may interact synergically to burst phagocyte effector functions as reported in human neutrophils (105).

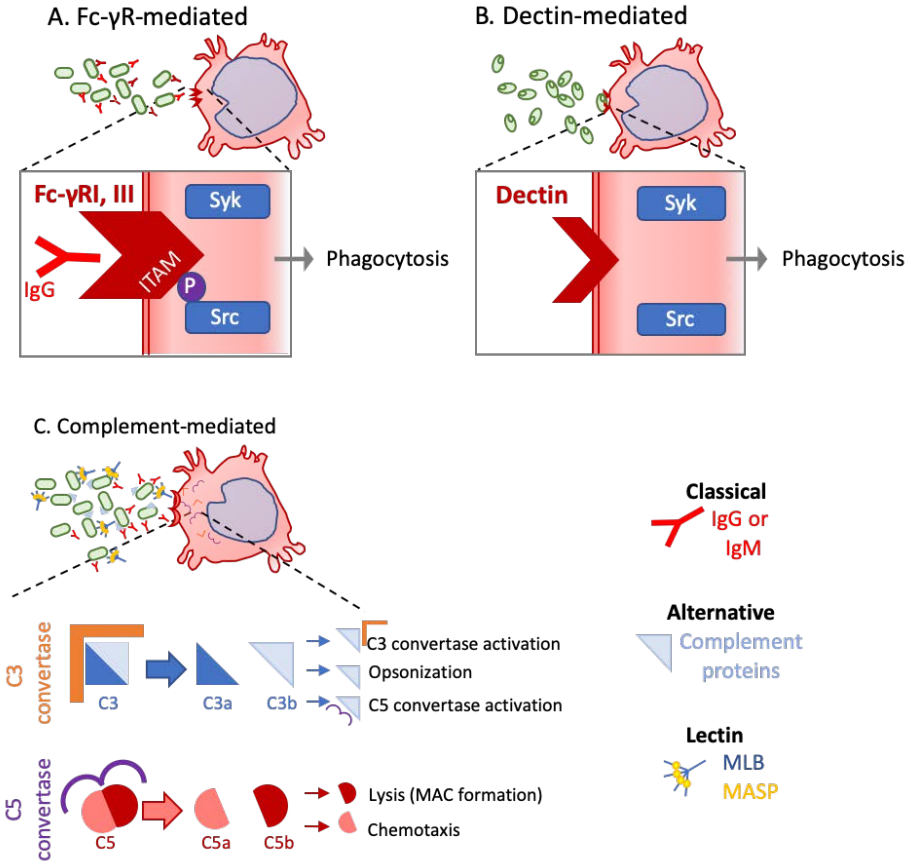

Figure 1. Molecular classification of Phagocytosis. A. Fragment-crystallizable γ receptor (FcγR)-mediated phagocytosis. It involves these opsonic receptors binding IgGs and exposing their immunoreceptor tyrosine-based activation motif (ITAM) to be phosphorylated by Src. Other proteins like Syk or phospholipases C and D (not shown) are also activated and recruited in order for phagocytosis to take place. B. Dectin-mediated phagocytosis. Dectin has been described to be involved in the phagocytosis of fungi by also clustering and exposing a motif similar to ITAM, finally also activating Src and Syk signalling pathways. C. Complement-dependent phagocytosis. It also requires opsonization of the target, and involves a cascade of activation of convertases. Importantly, although they can be activated at the same time, there are different pathways depending on the opsonizing particle, namely the classical, alternative and lectin pathways.

In contrast, phagocytosis classification can be done not by the receptors involved, but by the viability of the cell being phagocytosed. Brown and Neher's classification (106) describes phagocytosis as being primary or secondary. Primary phagocytosis is the process in which a cell dies in direct consequence of being phagocytosed, and they have renamed this term "phagoptosis". Secondary phagocytosis or "efferocytosis" occurs when a cell dying by apoptosis or necrosis is phagocytosed by microglia (72,107). The dying cell expresses "find-me" and "eat-me" signals, such as sphingosine 1-phosphate or phosphatidyl serine (PtdSer), respectively, which indicate the phagocyte they must destroy the cell expressing it (107,108). Particularly during efferocytosis, the target's membrane organization is altered: PtdSer, a very negatively-charged protein (109) which contributes to about 30% of the charge of the cell membrane (110) is highly expressed (72,107,110). This, together with the depolarization of the phagocyte (111), makes attraction and binding stronger. Moreover, some molecules in the target are tethered, and its cytoskeleton is reorganized, what may also contribute to the exposition of internal molecules to the outside, what can contribute to opsonization, or could even be recognized by the phagocytic cells, ultimately leading to phagocytosis (107).

In any case, in order to phagocytose the target, microglia and macrophages must first reach and recognize their target, and evidently, cytoskeletal actin and tubulin rearrangement is critical for this to be carried out. (81,83,84,86) (**Figure 2 A**). Phagocytes produce actin-rich structures which actively protrude (81) and these structures facilitate the binding of multiple receptors even if they do so with low affinity (112,113). Once the target is securely engaged, lateral clustering and mobilization of receptors occur (107,114), forming the flat interface (described in vitro in a 2D model), where we can find different receptors, such as SIRPα, or CD32 forming concentric activation rings (78) (**Figure 2B**). After the attachment takes place, polarization is stabilized by the microtubule organizing center (MTOC) (115), forming a phagocytic synapse, before encapsulating it and digesting it enzymatically. Once digested, antigens are presented to, for example, T cells, through another immunological synapse which is also of interest in order to understand the immune response (50,116,117) (**Figure 2 C**).

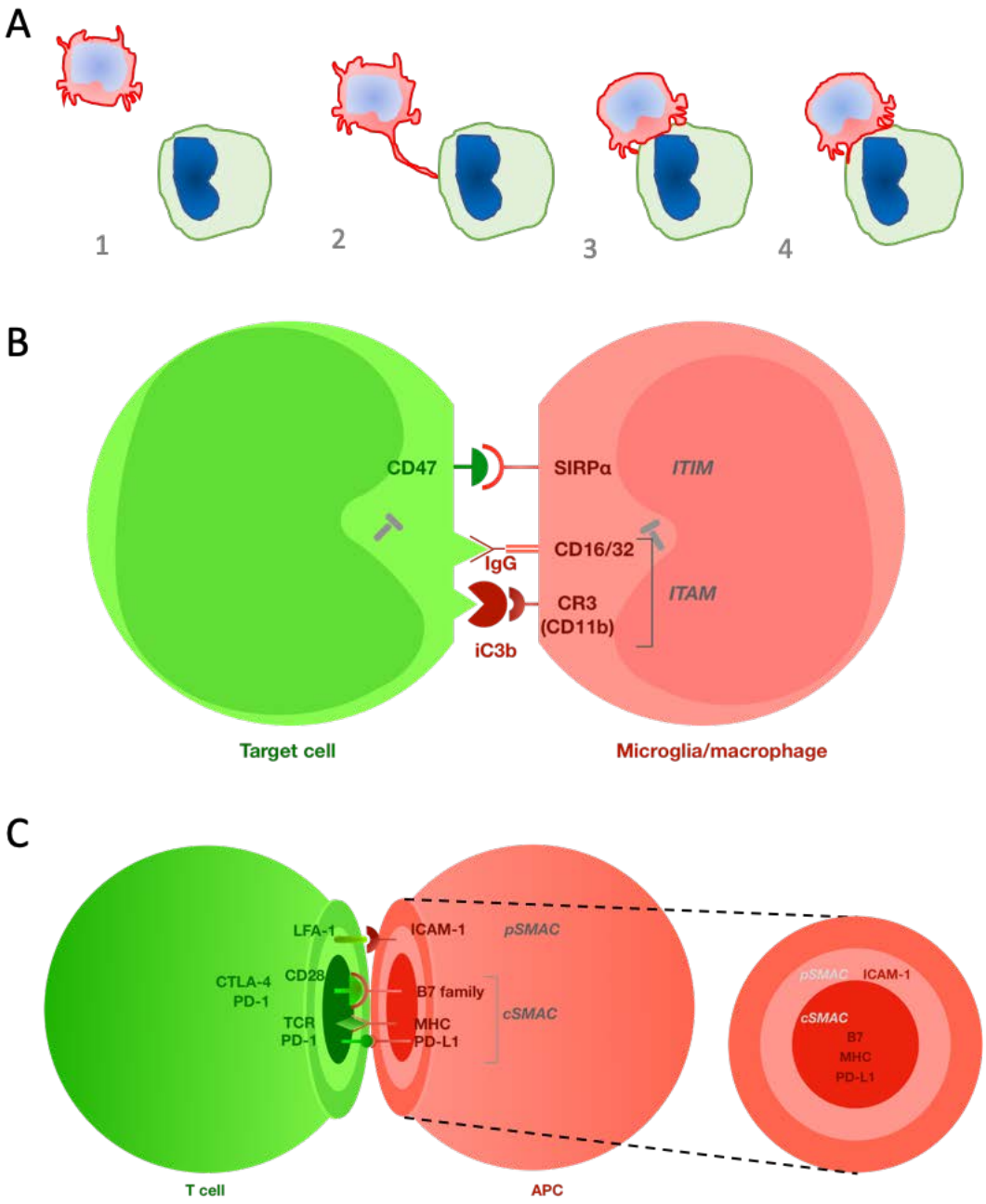

Figure 2. Antigen recognition by microglial/macrophage receptors. A. Diagram of the microglial/macrophage target recognition. Microglia/macrophages are "resting" while scanning the environment (1); and when they sense their target (2) they polarize towards it and attach with a flat interface (3) before forming the phagocytic cup (4). B. Phagocytic Synapse. CD16/32 and CR3 (CD11b) receptors are involved in the recognition of the target and they activate the signalling cascade through their ITAM motif ending up in phagocytosis; while SIRPα, as it bears an ITIM motif, signals the inhibition of phagocytosis. C. Immunological synapse. Once phagocytosis has taken place, microglia/macrophages act as antigen-presenting cells (APC) and communicate with T cells through immunological synapses. These consist in a flat interface with concentric supramolecular activation clusters (SMAC), and oriented nuclear indentation and MTOC location. A frontal SMAC detail would reveal in the APC's membrane, ICAM-1 receptor in the peripheral SMAC (pSMAC) and proteins like the B7 family proteins, MHC or PD-L1 in the central SMAC (cSMAC).

It is noteworthy the fact that most of the phagocytic studies have been done with peripheral blood cells, such as neutrophils (79,92,97,101) or macrophages, predominantly in vitro (55,68,78,93,95,97,111,118) although some in vivo (119), but

very little is known about the process of phagocytosis by microglia (31,85,106,120), especially in the human brain. In this thesis, we will try to illuminate to the understanding of this critical process that could potentially lead to tumor clearance.

Although plausible, this approach is not easy, as tumor cells are naturally able to evade phagocytosis. They do so by the expression of “don’t-eat-me” molecules, such as the transmembrane protein CD47 a marker of self, which binds SIRPα, therefore inhibiting phagocytosis (78,118,119,121–124). Thus, wouldn’t these “don’t eat me” signals be the perfect target for immunotherapy? Precisely, many researchers have thought of this, but one drawback is that these molecules are also expressed by cells of hematopoietic origin, such as erythrocytes (125), therefore blocking them could theoretically result in anemia. Specifically, there are several research groups that pursue the idea of blocking CD47, of tackling the overexpression of CD47 by tumor cells, so that microglia and macrophages, which express the CD47 ligand SIRPα, can phagocytose the cell which has no longer CD47 reachable (118,119,123,126–131). Some studies state that CD47 blockade in xenograph and immunocompetent models results in tumor destruction by T cells (128); while others state the foreseeable anemia (129). Hence, the future of these therapies could be to cause this blockade in a more localized manner. For instance, instead of blocking CD47 in general, another strategy could be block SIRPα, which is only expressed by the myeloid cells, and as in GBM these account for up to 30% of the tumor, in this way we could act primarily inside the tumor, at the level of the phagocytic synapse. Precisely, in this thesis we have aimed both strategies, to block CD47 and to block SIRPα in a mouse model by means of monoclonal neutralizing antibodies.

Other Important Players In Cancer Immunotherapy

As aforestated, after phagocytosis, microglia/macrophages become antigen presenting cells (APCs), expressing MHC, but currently it has not been fully defined how antigens are presented to T cells in the human brain (132). Under non-pathogenic conditions, such as learning and spatial memory, T cells in the brain are of vital importance, as demonstrated in rats (133). In pathogenic conditions, it has been demonstrated that upon activation in the lymph nodes, T cells are able to

extravasate to the deceased CNS (85,134,135) and even be homed after the injury (136). Detailed studies in other environments describe that FOXP3$^+$ T cells establish less immunological synapses. These cells are considered regulatory and in the tumor context they are anti-inflammatory, promoting tumor growth. This is why, in this regard, immunotherapies with T cells are becoming increasingly popular, and although none are currently efficient to battle glioma, there are under analysis in clinical trials. Existing T cell therapies include the administration inmunoglobulins which block checkpoint protein receptors within the immunological synapse, in this case being the space between the T cell and the target cell. T cell receptors (TCR) engage the MHC of the APC (116,117,137–141), what induces a signaling cascade ultimately determining the rearrangement of the cytoskeleton by the MTOC and the activation of the effector cell (116,140,142). Moreover, when establishing this immunological synapse, homologous to the microglia-target contacts with the "activation rings", proteins from both contacting cells (the APC and the T cell) bind each other and microanatomical changes happen **(Figure 2B**). For instance, lymphocyte function-associated antigen 1 (LFA-1) from the T cell binds the APC's intercellular adhesion molecule 1 (ICAM-1), finally creating a ring-shaped area called peripheral supramolecular cluster (pSMAC) (116,140,142), which surrounds an accumulation of TCRs interacting with MHCs which altogether conform the central supramolecular cluster (cSMAC) (116,140,142). Also in the immunological synapse (hypothetically in the pSMAC), we can find CD28 binding B7.1 or B7.2 present in activated APCs (141,143–145). This has been described in vitro, in vivo, and in some human tumors, but very little is known about this antigen presentation in glioma. This is of great concern, as current cancer immunotherapies involve these molecules. For instance, we can mention anti-cytotoxic T-lymphocyte–associated antigen 4 (CTLA-4), approved for the treatment of advanced melanoma with the name of ipilimumab; or anti-programmed death 1 (PD-1), used against melanoma and lung cancer, with the names nivolumab and pembrolizumab (146). Moreover, recently, a combination of nivolumab and ipilimumab has been approved by the Foods and Drugs Administration (FDA) in the United States of America for intermediate or poor-risk advanced renal cell carcinoma based on a study by (147). While the outcome of blocking these proteins is similar, the mechanism of action is different. Both CTLA-4 and PD-1 are present in the T cells and belong to the B7 receptor superfamily (141). When activated, their function is similar: to reduce T-cell proliferation, glucose

metabolism, cytokine production and survival, ultimately having a suppressive function (141). However, CTLA-4, a homolog of CD28, acts by binding a B7 protein and not letting CD28 act, therefore acting only downstream this signaling pathway, while PD-1 acts later in the immune response. It is of great importance also the differences in the expression of the ligands. CTLA-4 ligands are expressed by antigen-presenting cells (APCs) mainly in the lymph nodes; whereas PD-1 ligands (PD-L1 and PD-L2) are expressed in peripheral tissues by a variety of cells (146), including other T cells, B cells, myeloid cells and other less convenient cells, such as tumor cells (146). Precisely, PD-L1 expression has been found to correlate with poor prognosis in cancer patients, as it is responsible of leaving T cells unresponsive, exhausted (146). Even though there are clinical trials with these approaches to eradicate GBM, to date there are no effective therapies (3,9). This could be due to the variations in the T cells in the tissue. For instance, some tissues are more rich in PD-L1 than others, but after all, little is known about the distribution and function of T cells in glioma, as about their protein expression profile (148), and thus about the effectiveness of the immunotherapies targeting these cells. This is why we believe it is better to target microglia/macrophages in glioma, which account to up to 30% of the cells in the tumor, they are in theory able to directly kill cells, and mediate the T cell response in the tumor, what could help increase the effector cells against the malignant cells. Although very interesting and subject of an article from our research group (1) (**Appendix 2**), T cells will not be subject of this thesis, where we will elucidate the role of immune cells (mainly microglia/macrophages) in PPs, we will uncover phagocytosis in human GBM, and examine if phagocytosis in a glioma murine model can be promoted by means of immunotherapy, shedding light upon this emerging field.

Objectives

GBM remains incurable, the main hope for future patients being an effective therapy. As many immune cells infiltrate the tumor immunotherapy appears to be a very promising option. The most numerous cell type which is hypothetically able to destroy tumor cells is GAMMs, which by stablishing a cell-to-cell interaction, the phagocytic synapse or gliapse if cells are of glial origin, they can potentially kill the target by phagoptosis. With this rationale, we hypothesize that glioma cells evade the immune response by turning microglia/macrophages to an anti-inflammatory phenotype which impair their phagocytic capacity. Thus, the specific objectives in this thesis were:

- To determine the phenotype of GAMMs in the different microenvironments within human GBM.
- To elucidate the role of GAMMs in the understudied PPs in human GBM
- To prove the ability of microglia/macrophages to carry out phagoptosis of tumor cells in vitro.
- To demonstrate the phagocytic activity of microglia/macrophages in human GBM, in the murine model of C57BL6 mice injected with GL261 cells, and in vitro.
- To promote the phagocytic phenotype of GAMMs in vivo by neutralizing checkpoint blockers such as CD47 and SIRPα.

Materials and Methods

In order to facilitate the comprehension of the practices, I will divide materials and methods according to their nature.

Studies in Human Samples

Patients and samples

I used biopsies from six patients admitted to the General Hospital of Valencia and diagnosed with GBM, the most aggressive form of glioma. All protocols were approved by the two institutions involved, concerning the Ethics Committee on Animal and Human Research of the Universitat Autònoma de Barcelona (Bellaterra, Barcelona, Spain) and the Research Committee of the General Hospital of Valencia (Valencia, Spain), which included the informed consent of the patients. After extraction with minimal manipulation of the tissue, the procedure requires the immediate fixation of biopsies in 4% paraformaldehyde (PFA), allowing the preservation of the microstructure. After fixation, samples were cryo-protected and sectioned in a cryostat (Leica Microsystems, Wetzlar, Germany). Part of each sample was used for routine neuro-pathological examinations and diagnosis, while the samples used from this thesis came from 2.5 ml of the tissue, which were submerged during one week in 4% PFA before being washed with phosphate-buffered saline (PBS) 0.1M/L, pH 7.4, and stored in PBS with 0.1% sodium azide (NaN_3) until being sectioned by vibratome (Leica Microsystems, Germany) into 60 µm slices.

The pathology department of the hospital provided the diagnosis and grade, including the Ki67 proliferation index. Samples showed the typical features of glioma, such as high GFAP and Vimentin reactivity, marked cellularity with hyperchromatism and pleomorphism, gemistocytic differentiation, aberrant mitoses, glomeruloid vessels, necrosis and, importantly, a clear presence of PPs.

Histochemistry

Thionine staining was performed to analyze the anatomical structure of the tissue, detect the nuclei of the cells and visualize the cell-division status of each tumor. For each sample we were able to see the classical GBM histopathological features, including the presence of PPs. For this, thionine (acetate) (Certistain; Merck KGaA; Darmstadt, Germany) solution (25mg/100ml acetate buffer pH: 4.6) in acetate buffer solution (Stem solution A, sodium acetate 0.1 M; Stem solution B, Acetic acid 0.1M) was used. All the samples were first mounted on gelatinized slides, dried and then rinsed in distilled water, stained in thionine solution for 5 minutes, washed in distilled water; and dehydrated in increasing concentrations of ethanol and Xylene. Then, sections were cover-slipped to be analyzed at the conventional light microscope (Eclipse 80i microscope, Nikon), taking the required pictures with a digital camera connected to the microscope (DXM 1200F Digital Camera, Nikon).

Immunohistochemistry

Free-floating immunohistochemistry by diaminobenzidine (DAB) detection was performed on tumor sections to visualize immune-cell markers, glial-tumor-cell markers, and the signaling molecule NF-κB. In order to identify GAMMs in GBM, antibodies against antigens commonly expressed by macrophages were used: M2-like GAMMs were identified by positive immunostaining of the M2-spectrum cell-surface marker Cluster of Differentiation 163 (CD163), whereas the panGAMM marker used was Ionized calcium-binding adapter molecule 1 (Iba-1) (also named AIF-1). HLA-DP, -DQ, -DR (major histocompatibility complex II or MHCII) was also used to see the myeloid cell population within the M1-spectrum. Specifically, primary antibodies used were those to recognize: Iba-1 (1:500, polyclonal rabbit immunoglobulin (Ig) G; Wako Pure Chemical Industries, Ltd.; Osaka, Japan), CD163 (1:150, monoclonal mouse IgG; Abcam; Cambridge, United Kingdom (UK)), MHCII (1:100, mouse IgG1; Dako Cytomation; Glostrup, Denmark); and NF-κB p65 (1:100, rabbit IgG; Cell Signaling Technology, Danvers, MA, USA). Samples were first treated with citrate (10mM, pH 6, 60ºC, 20 minutes) to ameliorate antibody binding by antigen retrieval. At that point, 0.3% hydrogen peroxide was used to block endogenous peroxidase, and sections were blocked for 1 hour with 0.5% Triton X-100 with 10% horse serum (HS10%) (Sigma-Aldrich; St. Louis, MO, USA) before

incubating overnight with primary antibody diluted in Trizma Base Saline (TBS)-0.5% Triton X-100, 1% horse serum and 0.1% sodium azide. The primary antibodies used are described above. Secondary antibodies were biotinylated goat anti-mouse or biotinylated goat anti-rabbit (1:1000; Dako; Denmark), diluted in 0.5% Triton X-100 with 1% horse serum and 0.1% sodium azide, accordingly to the host of the primary antibodies. Secondary antibodies were detected by the Vectastain Elite ABC horseradish peroxidase method (Vector Laboratories; CA, USA). Sections were mounted on gelatinized glass slides and were dehydrated through graded ethanol solutions (70%, 80%, 90% and 100%) and submerged in Xylene before coverslipping.

In the case of NF-κB staining, a double immunohistochemistry was performed. The afore-mentioned standard protocol was done with the sole modifications of the citrate buffer solution temperature (80ºC) and the secondary antibody dilution (1:500 in 1% horse serum). After Vectastain Elite ABC horseradish peroxidase method (Vector Laboratories; CA, USA) was carried out, instead of mounting the sections, sections were washed in PBS and incubated with anti-MHCII primary antibody and the standard protocol was once again followed. This time, the Vectastain Elite ABC horseradish peroxidase method (Vector Laboratories; CA, USA) was used with two drops of the nickel solution included in the kit. This way, MHCII $^{+}$ cells will be visualized in a black color while NF-κB is displayed in brown. Like in the standard protocol, the sections were mounted on gelatinized glass slides and were dehydrated through graded ethanol solutions (70%, 80%, 90% and 100%) and submerged in Xylene before coverslipping to later on be analyzed at the microscope (Eclipse 80i microscope, Nikon), taking the required pictures with a digital camera connected to the microscope (DXM 1200F Digital Camera, Nikon).

Immunohistofluorescence

Free-floating immunofluorescence was performed on tumor sections for multiple stainings to visualize Iba-1^{+} and MHCII^{+} cells either with their MTOC, or combined to also see GFAP^{+} cells and the cells' relation to blood vessels. Antigen retrieval and blocking was done as previously mentioned before incubating during 48 hours with the primary antibodies diluted in 1% HS. The primary antibodies used were anti-human Iba-1 as described for the immunohistochemistry (1:500, rabbit polyclonal;

Dako Cytomation; Glostrup, Denmark); anti-MHCII (1: 100, mouse IgG1; Dako Cytomation; Glostrup, Denmark); anti-GFAP (1:500, chicken IgY; Abcam, Cambridge, UK); anti- γ-tubulin (to detect the MTOC) (1:500, mouse IgG1; SIGMA; Saint Louis, MO, USA); anti-CD31 (1:200, mouse monoclonal IgG1; Abcam, Cambridge, UK); anti-collagen IV (1:200, rabbit polyclonal; Abcam, Cambridge, UK); and anti-CD3 (1:100; rabbit polyclonal; ; Dako Cytomation; Glostrup, Denmark). Secondary fluorescent antibodies diluted in 1% HS were used accordingly with the host of the primary antibodies. For the study of the cells' directionality, we used AlexaFluor 488 Goat anti-Rabbit 1:1000 (Life technologies; Carlsbad, CA, USA) (also used to detect anti-collagen IV) and AlexaFluor 555 Goat anti-mouse IgG1 1:1000 (Life technologies; Carlsbad, CA, USA) (likewise for CD31); and on the other hand, 488 Goat anti-Rabbit 1:1000 (Life technologies; Carlsbad, CA, USA) and AlexaFluor 555 Goat anti-Chicken 1:500 (Life technologies; Carlsbad, CA, USA) to see the cells' interactions. When MHCII was combined with GFAP, the secondary antibody used for the detection of MHCII was AlexaFluor 647 anti-mouse IgG 1:500 (Life technologies; Carlsbad, CA, USA); and when staining CD3, the secondary antibody used was AlexaFluor 647 Goat anti-rabbit 1:1000 (Life technologies; Carlsbad, CA, USA). Then 4',6-diamino-2-phenylindole (DAPI) (1:1000; Life technologies; Carlsbad, CA, USA) was used for 30 minutes to stain the nuclei of the cells. Sections were mounted on glass slides and coverslipped using Prolong antifade reagent (Invitrogen; Carlsbad, CA, USA).

Confocal microscopy, analysis and quantification

Human biopsies stained by immunofluorescence were imaged with a confocal laser-scanning microscope (LSM 700, Carl Zeiss) utilizing a Plan-Apochromat 40x/1,3 Oil DIC M27 objective lens (Carl Zeiss) and processed with the ZEN 2010 software (Carl Zeiss). Three-dimensional reconstructions were generated using the α blending softwares ZEN 2010, Imaris (BitPlane, South Windsor, USA) and iLlucida FX (iLlucida LLC, Los Angeles, USA). Z-stacks were acquired to cover the depth of the tissue (25-30 images/stack) with a 0.5 μm step size, and the images for quantification were always taken with the necrotic focus on the upper part of the image (Figure 5), considering that the scanning field could be rotated and oriented. Raw images were imported into both Imaris (Bitplane, Zurich, Switzerland) and Image J (version 1.4.3.67, NIH, USA) softwares, where they were further processed for morphometric

analyses and cell counts. For the cells' directionality, in order to better visualize the MTOC, zoom 1.7X was used, while the Iba-1/GFAP staining was visualized with zoom at 1.0X. On the former, the Iba-1 channel composing the Z-stack was iso-surfaced using Imaris Surpass, in order to view a three-dimensional representation of the Iba-1+ cells. To detect the MTOC within the cells, the module Spots was used. Within the Cell module, the nuclei were detected and then the MTOC were imported as vesicles (vesicle tool). The Iba-1 surfaces were imported as the cells' cytoplasm (surfaces tool). α blending software Imaris, (Bitplane, Zurich, Switzerland) and iLlucida FX (iLlucida LLC, Los Angeles) allowed the free rotation of the three-dimensional reconstructions of 21 images from all tumors, the which were analyzed to see Iba-1 cells' directionality by the observation of the distribution of the MTOC of interest within the cells. The same procedure was performed when analyzing the cells at the different positions within the PPs. This time, seven PPs were divided into three equidistant horizontal frames, which we called "proximal" (P), "intermediate" (I) or "distal" (D), corresponding to the relative distance of the zones to the NF, as shown in Figures 2 and 5.

In the case of the Iba-1/GFAP staining, a grid was drawn on the image with Image J software on 23 palisade images from 5 tumors. This grid was made of nine centered 1600 μm^2 squares, which determined three areas, which we again called P, I and D, corresponding to the relative distance of the zones to the NF. Of the nine squares, only the central column was taken into account, and only one central slice of each palisade was analyzed to obtain the values of the amount of nuclei, the different types of phagocytic events and the kind of intercellular contacts (longitudinal or perpendicular), which were then extrapolated in order to obtain values per mm^2. To see the amount of contacts in general, by means of the ImageJ software, a cross grid with an area of 800 μm2 per point was drawn. An intermediate optical slice of each Z-scan per palisade was chosen, and Iba-1^+ cells hitting the crosses were analyzed to see the amount of contacts with $GFAP^+$ cells in the depth of the z-stack. This way we were able to estimate the contacts between Iba-1^+ cells and $GFAP^+$ material in the different areas of the palisade, as two rows of crosses corresponded to each of the "P", "I" or "D" zones, as we resolved before.

An animation of the 3D rendering was also generated to better show the disposition of the Iba-1^+ cells in the palisade, their interaction with $GFAP^+$ cells, and to see in

detail phagocytosis in the human tissue. The same reconstructions that were used to quantify the cells directionality and the contacts with $GFAP^+$ cells were used for this. After the iso-surfaces were done, the video was created with the Key Frame Animation function and further edited with iMovie software (Version 10.1.10, Apple Inc, Cupertino, CA, USA). In order to reveal the phagocytosis of a $GFAP^+$ cell, an image of the human tissue staining against MHCII and GFAP (counterstained with DAPI) was also reconstructed by means of the Imaris (BitPlane, South Windsor, USA) software. Again, MHCII channel composing the Z-stack was iso-surfaced using Imaris Surpass, in order to view a three-dimensional representation of the phagocyte. The same was done for the GFAP and the DAPI channels. Finally, a video of the cells was done with the Key Frame Animation function and further edited with iMovie software (Version 10.1.10, Apple Inc, Cupertino, CA, USA).

Cell culture studies

Cell lines

Cell culture and treatment

Murine cell lines BV-2 (microglia) and GL261 (glioma) (from the Cell Cultures unit at the *Universitat Autònoma de Barcelona*'s (UAB) *Institut de Neurociències* and purchased from the National Cancer Institute at Frederick, respectively) were maintained in RPMI-1640 medium (Sigma Aldrich, Saint Louis, MO) supplemented with 10% heat-inactivated fetal bovine serum (FBS), 0.1% Penicillin/Streptomycin (P/S) at 37ºC and 5% CO2 in a humidified incubator. In order to do immunostainings, cells were seeded on coverslips pre-treated with poly-L-lysine (PLL) at a concentration of 25 µg/mL and washed twice with PBS.

In regard to seeing how glucose deprivation affected cells, both cell lines were seeded into 24-well culture plates one day before treatment at a density of 50,000 cells/mL, and the day of the experiment the medium was changed for fresh medium, either glucose-free RPMI-1640 supplemented with 0.1% P/S, or the same medium but also supplemented with L-glucose at a final concentration of 2g/L. After 24h, cells were fixed with 4% PFA before immunostaining.

For the hypoxia experiment, both cell lines were seeded into 24-well culture plates one day before treatment as previously described, and the day of the experiment the medium was replaced with fresh supplemented RPMI-1640 medium and cells were incubated in either the humidified incubator with normoxic (21% oxygen) conditions or the hypoxic (Baker Ruskinn InvivO2 200) workstation, always at 37ºC and 5% CO2. After 24h, cells were fixed with 4% PFA before immunostaining.

Microfluidic plates (CellASIC™ ONIX M04G-02-5PK, EMD Millipore Corporation; Hayward CA) were used to record the natural movement of BV2 and GL261 cells, thus under normoxic and normoglycemic conditions. For this, after treating the plate with PLL (25 ug/mL) and washing it, cells were plated at a low density to avoid confluence during the experiment. After 24h in the humidified incubator, flows of normally supplemented RPMI-1640 were created, what permitted us to record the cells in an always fresh medium.

Microfluidic plates (CellASIC™ ONIX M04S-02, Merck) were also used to see how BV2 and GL261 cells reacted to a hypoxic gradient. Hence, after treating the plate with PLL (25 µg/mL) and washing it, cells were plated at a low density to avoid confluence during the experiment. Creating flows of Normoxic RPMI-1640 medium normally supplemented and the same medium but bubbled with N_2 in order to displace the O_2 in it (hypoxic medium), we achieved the creation of a gradient in the chambers where the cells were seeded.

In pursuance of having a positive control of p65 NF-κB translocation in microglial cells, BV-2 cells were seeded on PLL-treated coverslips in a 24-well plate at a density of 20,000 cells/mL. After 24h in the incubator (37ºC, 5% CO_2), cells were treated either with the pro-inflammatory compound LPS (500 ng/mL), with the anti-inflammatory Ibuprofen (200 uM) or with both at the same time. After 24h with these treatments in the incubator, cells were fixed with 4% PFA.

In order to see the interaction between microglial and glioma cell lines, we stained the cells while alive in the culture plates. First of all, when confluent, BV-2 cells were tripsinized and resuspended at a density of 10^6 cells/mL in PBS, moment at which CellMask™ Orange Plasma Membrane stain (ThermoFisher Scientific) was added (1:1000). After incubation for 5 minutes at 37ºC, cells were once again centrifuged (2 minutes, 1,500 rpm) and resuspended in RPMI culture medium (supplemented with

10% FBS, 0.1% P/S) at a density of 50,000 cells/mL to be seeded in a 6-well plate, to be time-lapsed when co-cultured with GL261 cells, and in a 24-well plate to be later on fixed and immunostained without being time-lapsed; both plates were kept in the incubator at 37ºC and 5% CO_2 overnight. The next step was to stain the GL261 cells before co-culturing them with the BV2 cells. Confluent GL261 cells were tripsinized and brought to a concentration of 10^6 cells/mL for staining, first with the NucBlue stain from ReadyProbes™ Cell Viability Imaging kit (ThermoFisher Scientific), which stains the nuclei of the cells to be seen in the UV spectrum, by adding 2 drops/mL and incubating the cells at 37ºC for 5 minutes. After this, cells were centrifuged (1500 rpm, 2 minutes) and resuspended in PBS again at 10^6 cells/mL. Part of this resuspension was destined to be stained with CellMask™ Deep Red Plasma Membrane stain (1:1000, ThermoFisher Scientific), for 15' at 37ºC, before dilution to 100,000 cells/mL in RPMI medium; and the other part was centrifuged to be taken to a concentration of 100,000 cells/mL without CellMask™ Deep Red Plasma Membrane stain but with NucGreen™ Dead 488 ReadyProbes™ Reagent to be time-lapsed for 2h in the Eclipse TE2000 inverted microscope. In the case of the cells cultured in the 24-well plate, NucGreen™ Dead 488 ReadyProbes™ Reagent was also added at a concentration of 2drops/mL, but only in four wells in order to see if the target cells are dead before being phagocytosed or after. The coverslips in the 24-well plate were fixed at 1h since co-culture. with PFA 4% for 20 minutes, and after washing twice with PBS, the coverslips were mounted on glass slides with Prolong antifade reagent (Invitrogen; Carlsbad, CA, USA) in the case of the wells with the NucGreen™ Dead 488 ReadyProbes™ Reagent, but immunostained against CD11b and CD16/CD32 in the other cases, to see the role of these receptors in the phagocytic synapses and phagocytic cups of glioma cells by microglia.

Immunocytofluorescence

In the case of the hypoxic and hypoglycemic experiments, the cells were stained to see their morphology. After cell fixation, PFA was washed with PBS and cells were treated for antigen retrieval with PBS with 0.02% saponine for 7 minutes. After washing this solution, a mild blocking solution was added (PBS with 0.01% saponine, 10mM Glycine) for 15 minutes before blocking with a more concentrated solution for 1h (PBS with 0.01% Saponine, 10 mM Glycine, 5% BSA). The primary antibody anti-γ-tubulin (1:500, mouse IgG1; Dako Cytomation; Glostrup, Denmark) was diluted in

PBS with 0.01% Saponine, 1% BSA, and left in a humidity chamber overnight at 4ºC. AlexaFluor 555 Goat anti-mouse IgG1 1:1000 (Life technologies; Carlsbad, CA, USA) was used as a secondary antibody for 45 minutes, and after washing, Alexa Fluor 647 Phalloidin (Life technologies; Carlsbad, CA, USA) was used for the analysis of the protrusions and Alexa Fluor 488 Phalloidin (Life technologies; Carlsbad, CA, USA) was used for the morphometric analyses, both at 1:40 for another 45 minutes. Nuclei were counterstained with DAPI for 5 minutes before washing with PBS and mounting the coverslips on glass slides using Prolong antifade reagent (Invitrogen; Carlsbad, CA, USA). NF- κB translocation was studied by staining microglia's tubulin cytoskeleton with the primary antibodies to detect α-tubulin (1.100, mouse IgG1; Sigma-Aldrich, St. Louis, MO, USA) and p65 NF- κB (1:100, rabbit IgG, Cell Signaling, Danvers, MA, USA), and the secondary antibodies AlexaFluor 555 Goat anti-mouse IgG1 1:1000 (Life technologies; Carlsbad, CA, USA) and AlexaFluor 488 Goat anti-Rabbit 1:1000 (Life technologies; Carlsbad, CA, USA), respectively; following the same protocol explained for the hypoglycemic and hypoxic experiments.

The interactions between BV-2 and GL261 cells was further characterized by immunostaining CD11b (1:100, rat monoclonal IgG2b; AdB Serotec, Bio-Rad laboratories, Hercules, CA, USA) and CD16/CD32 (1:100, rat monoclonal IgG2b κ; Becton, Dickinson and Company, Eysins, Switzerland). After washing the primary antibodies, the secondary antibody AlexaFluor 488 goat anti-Rat 1:1000 (Life technologies; Carlsbad, CA, USA) was used to visualize CD11b and CD16/CD32. Washing the coverslips and counterstaining with DAPI for 5' was done before mounting the samples in microscope slides.

Microscopy, analysis and quantification

BV2 and GL261 cells stained to see their MTOC and actin in 647 were sampled with the confocal laser-scanning microscope (LSM 700, Carl Zeiss) and a Plan-Apochromat 40x/1,3 Oil DIC M27 objective lens (Carl Zeiss), to be processed with the ZEN 2010 software (Carl Zeiss). Three-dimensional reconstructions were generated using the α blending softwares ZEN 2010, Imaris (BitPlane, South Windsor, CT) and iLlucida FX (iLlucida LLC, Los Angeles). Z-stacks were acquired to cover the entire mono-layer of the culture (20-25 images/stack) with a 0.5 μm step size. One picture was taken for each replicate, being done triplicates.

In order to analyze the cells' morphology, and the translocation of NF-kB in BV-2 cells, all replicates were sampled homogeneously using a fluorescence (Nikon Eclipse 90i) microscope attached to a DXM 1200F digital camera. Pictures were taken at a 20X objective using the software ACT1 version 2.70 (Nikon corporation).

Regarding the cells' kinetic activity, we imaged the cells in the microfluidic plates with an Eclipse TE2000-E inverted microscope, taking pictures at 10X every 15 minutes for 24h. Three time-lapse videos per condition were analyzed to track the cells in hypoxic gradient, using the Chemotaxis Tool Plugin in ImageJ (version 1.4.3.67, NIH, USA).

About the interactions between BV-2 and GL261 cells, once again the confocal laser-scanning microscope (LSM 700, Carl Zeiss) and the Plan-Apochromat 40x/1,3 Oil DIC M27 objective lens (Carl Zeiss) was used. Three-dimensional reconstructions were generated using the α blending softwares ZEN 2010, Imaris (BitPlane, South Windsor, CT) and iLlucida FX (iLlucida LLC, Los Angeles). Z-stacks were acquired to cover the entire mono-layer of the culture (20-25 images/stack) with a 0.5 μm step size.

These interactions were also studied while the cells were still alive. Again, with the Eclipse TE2000-E inverted microscope, pictures at 10X were taken every 5 minutes for 2h.

For the BV-2 /GL261 co-culture using the light-momentum method, a microscope slide was pre-treated with PLL at 25 ug/mL for one hour, before seeding BV-2 cells (50,000 cells/mL, on the slide) which were obtained by trypsinization when confluent. The slice was incubated overnight in a petri dish (37ºC; 5% CO_2). On the next day, a coverslip was framed with double-sided tape and in the center were placed GL261 cells (which were also tripsinized). The medium of the BV-2 cells was withdrawn and the slide was sticked to the coverslip, to take it to the TE-2000E inverted microscope coupled to an optical tweezers platform (SENSOCELL™, Impetux Optics S.L.). Here, the tweezers trapped a GL261 and it was manually approached to a BV-2 cell adhered to the glass slide while recording the interaction.

Primary cell cultures

New born Sprague Dawley rats (post-natal days 0-2) were sacrificed in order to obtain the glia from their cortex. The animals were obtained from the animal facility of the UAB, where the experiments were carried out, following the protocol approved by the Ethics Committee on Animal and Human Research of the UAB. Five solutions were used throughout the culture, and all of them were filtered (0.2 µm filter) prior their use: Solution 1 consisted in 50 mL Krebs buffer (120 mM NaCl, 4.8 mM KCl, 1.2 mM KH2PO4, 25 mM NaHCO3, 14.3 mM Glucose), with 0.15 g BSA (Sigma-Aldrich, St. Louis, MO, USA) and 0.4 mL MgSO4 3.8%. Solution 2 was created with 10 mL solution 1 and 2.5 mg trypsin (Sigma-Aldrich, St. Louis, MO, USA). To make solution 3, 10 mL of solution 1 were mixed with 0.8 mg DNase (Sigma-Aldrich, St. Louis, MO, USA), 5.2 mg of trypsin inhibitor (Gibco) and 0.1 mL MgSO4 at 3.8%. Solution 4 consisted in 8.4 mL solution 1 and 1.6 mL solution 3. Finally, solution 5 was a mix of 5 mL solution 1, 40 uL MgSO4 3.8% and 6 ul $CaCl_2$ 1.2%. After the whole brain was extracted, the meninges were discarded and the cortex was separated from the rest of the brain. It was cut in small sections and resuspended in 15 mL solution 1. This was followed by centrifugation (30 seconds, 1500 rpm) and the pellet containing the cells was resuspended in the solution 2 and incubated 10 minutes at 37ºC, with gentle mixing every 2-3 minutes to better digest the tissue. This enzymatic digestion was stopped when adding solution 4 and everything was centrifuged again at 1500 rpm. The pellet was resuspended in 3 mL solution 3 and mechanical disaggregation was performed by gently pipetting up and down with a Pasteur pipette 10 times. The cells were isolated into a uniform single-cell suspension by the use of a cell strainer and gently pipetting again up and down 10 times. All this cell suspension was added to the tube with solution 3 before centrifuging 5 minutes at 1000 rpm. Again, the supernatant was discarded and the pellet was resuspended in 10 mL DMEM supplemented with 1% P/S and 10% FBS, medium in which the cells were later on cultured. After resuspension, cells were counted to be cultured at the desired density, 300,000 cells/mL, in a culture flask or 24-well plates at 37ºC and 5%CO_2.

For the co-culture of activated microglia with either primary astrocytes or C6 cells, the medium was changed once a week; and three weeks after, the flasks were shaken for 2h at 300 rpm, in order to extract the microglia, which was again cultured, this time at 100,000 cells/mL in 24-well plates with 50% conditioned media. To activate

this microglia, we added IFN-γ (25 ng/mL) and LPS (10 ng/mL), and we had three control groups: an untreated one, one only treated with IFN-γ (25 ng/mL) and another one treated with just LPS (10 ng/mL). After 24h, we collected the supernatant for the griess assay and astrocytes or early-passage C6 cells were collected by tripsinization and co-cultured with the microglia at 100,000 cells/mL.

On the other hand, for the culture of the primary mixed glia with pro-inflammatory and anti-inflammatory stimuli in different order prior to C6 presentation, the 24-well plates had their media changed once a week and three weeks after seeding they were treated. In this case, experimental groups were: untreated control group; control of LPS (100 ng/mL) / IFN-γ (100 ng/mL) activation; controls of IL-4 at different concentrations (20 ng/mL and 100 ng/mL) and the combinatory treatments with LPS (100ng/mL) and IFN-γ (100 ng/mL) with either IL-4 at a low dose (20ng/mL) or at a high one (100 ng/mL).

Griess method

In order to detect the nitrites in the supernatant of the cells by spectrophotometry, when the medium in which cells grew was changed, the old medium was frozen (-80ºC) until used. On the one hand, a calibration curve was done with $NaNO_2$, at concentrations ranging from 100 uM to 0.78125 uM. Then, 100 uL of each of these and each of the samples were plated on a 96-well plate and 100 uL of sulfanilic acid (Griess reagent, Sigma-Aldrich ,St. Louis, MO, USA) (4 mg/mL) were added and incubated for 15' before reading the absorbance at 540 nm to detect the amount coloured azoic formed in the reaction. The amount of nitrites was then intrapolated from the calibration curve. This protocol was developed by Griess (149) but later modified (150).

Immunocytofluorescence

The primary cells (and rat glioma cells, C6) were stained to see their morphology and be able to count them. After cell fixation, PFA was washed with PBS and cells were treated for antigen retrieval with PBS with 0.02% saponine for 7 minutes. After washing this solution, a mild blocking solution was added (PBS with 0.01% saponine, 10mM Glycine) for 15 minutes before blocking with a more concentrated solution for 1h (PBS with 0.01% Saponine, 10 mM Glycine, 5% BSA). The primary antibodies

used were: anti- OX42 (to stain the microglial cells) (1:500, mouse IgG2a; Abcam; Cambridge, UK) anti-p65 NF-κB (1:100, rabbit IgG, Cell Signaling, Danvers, MA, USA) and anti-GFAP (1:500, chicken IgY; Abcam, Cambridge, UK). They were diluted in PBS with 0.01% Saponine, 1% BSA, and left in a humidity chamber overnight at 4ºC. AlexaFluor 647 Goat anti-mouse IgG2a 1:1000 (Life Technologies; Carlsbad, CA, USA) was used as a secondary antibody to detect $OX42^+$ cells; while AlexaFluor 488 Goat anti-Rabbit 1:1000 (Life Technologies; Carlsbad, CA, USA) was used to detect p65 NF-κB; and AlexaFluor 488 anti-chicken 1:500 (Life Technologies; Carlsbad, CA, USA) to see C6 cells and astrocytes. The secondary antibodies were incubated for 45 minutes. Nuclei were counterstained with DAPI for 5 minutes before washing with PBS and mounting the coverslips on glass slides using Prolong antifade reagent (Invitrogen; Carlsbad, CA, USA).

Microscopy, analysis and quantification

These samples were examined with the confocal laser-scanning microscope (LSM 700, Carl Zeiss) and a Plan-Apochromat 40x/1,3 Oil DIC M27 objective lens (Carl Zeiss), to be processed with the ZEN 2010 software (Carl Zeiss). Three-dimensional reconstructions were generated using the α blending softwares ZEN 2010, and iLlucida FX (iLlucida LLC, Los Angeles). Ten Z-stacks were acquired to cover the entire mono-layer of the culture (20-25 images/stack) with a 0.5 μm step size; and used to see the translocation of p65 to the nuclei; while single snaps were taken to see the area occupied by OX42 and count the amount of cells. To know the percentage of C6 and astrocytes, we divided the number of these by the total number of cells in the culture.

In vivo studies

Mice

Mice were initially purchased from Janvier at an age of 3 weeks, and subsequently maintained under standard housing conditions (12 h light/dark cycle and fed ad libitum) for two weeks, in groups of five mice per cage, before tumor implantation. All 30 mice used were males (studies with females are planned for the near future), their strain being C57BL/6. Two independent studies were carried out, one using anti-

CD47 antibody (see specifications below), and another one using anti-SIRPα antibody (see specifications below). All procedures were identical, only changing the functional blocking antibody administered.

Tumor implantation and treatment

Firstly, mice were anaesthetized with a mixture of ketamine (Imalgene) (Merial laboratorios, Barcelona, Spain), at a dose of 100 mg/kg; and Medetomidine (Medetor) (Ecuphar, Barcelona, Spain), at a dose of 0.5 mg/kg. Surgery was performed on a heat mat for thermoregulation. Tumors were then generated in the striatum by stereotaxically inoculating during two minutes 0.5 µl of GL261 cells at early passages (2-6), at a concentration of 20,000 cells/µl. More specifically, the coordinates used in relation to Bregma were Anteroposterior (AP): + 0.5 mm; Mediolateral (ML): + 2.1 mm; Dorsoventral (DV): - 3 mm. After inoculation, the needle was left in place for two more minutes before slowly removing it and stitching back together the skin in the head of the mice. Once recovered, animals were randomly assigned into cages in groups of five mice per cage (day 1) and weight daily throughout the course of the experiment.

For the treatments, at day 7 animals were once again randomly assigned a group, in which they could receive the vehicle solution (PBS) (n=5 in each experiment), the control isotype rat antibody (rat IgG2b) (n=5 in each experiment), or the treatment anti-CD47 (Biolegend, San Diego, CA, USA) or anti-SIRPα (Biolegend, San Diego, CA, USA) (n=5 in each case). The administration of these substances was done intraperitoneally, injecting 100 µg/mouse. At day 14, the mice received a second dose of treatment identical to the first one (control group likewise received 100 µl of PBS). Animals were euthanized when they met the behavioral endpoint established and approved by the Ethics Committee on Animal and Human Research of the Universitat Autònoma de Barcelona (Bellaterra, Barcelona, Spain), where the experiments were carried out.

We extirpated the mice's spleens in order to weigh and measure them as a proof of the animals' general immune state. In the case of the SIRP α experiment. After splenic excision, mice were intracardiacally perfused with 4% PFA and brains were then collected to be post-fixed in 4% PFA for two days before being submerged in a

PBS solution with 0.1% sodium azide until being sectioned by vibratome (Leica Microsystems, Germany) into 60-µm slices.

Sectioning

After post-fixation and storage, olfactory bulbs were discarded and 0.5 cm of the most rostral part of the brains were sectioned by vibratome (Leica Microsystems, Germany) into 60 µm slices, to have a total of six series of the 0.5 cm long tissue. The speed used for this sectioning was 0.225 mm/s and the vibration frequency 50 Hz. Once sectioned, the tissue was stored again in PBS + 0.1% sodium azide until its staining.

Histochemistry and tumor volume

Thionine (Nissl) staining was performed to analyze the volume of the tumors. We followed the same protocol as we did with the thionine staining in the human samples. After mounting and coverslipping, the microscope slides were scanned using HP photosmart B11a (Model CN245B#BEK, Hewlett-Packard, Palo Alto, California, USA) and the volume was calculated by Cavalieri's principle and Delesse stereological formula, by manually measuring the area in each slide with Image J 's polygon selection tool, and multiplying the area by the width of the sections (60 µm) and the number of series (six) when the sectioning was carried out, obtaining the value of the tumor volume in mm^2.

Immunohistofluorescence

Free-floating immunofluorescence was performed on murine brain sections for stainings to visualize Iba-1^+ cells and see their phagocytic capacity. To distinguish between the myeloid nuclei and the ones being phagocytosed, these stainings were combined with a PU.1 staining, which marks the nuclei of cells of myeloid origin. Antigen retrieval and blocking was done as previously mentioned (with citrate solution and HS, respectively) before incubation during 24h hours with anti-PU.1 (1:500, rabbit IgG; Cell Signaling technology; Danvers, Massachusetts, USA) primary antibody diluted in 1% HS. Next, AlexaFluor 555 Goat anti-rabbit 1:1000 (Life Technologies; Carlsbad, CA, USA) was incubated for 1h, then rinsed and again incubated for 24h. Anti-Iba-1 primary antibody (1:500, rabbit polyclonal; Dako Cytomation; Glostrup, Denmark) diluted in 1% HS was incubated for another 24h and

the secondary antibody to recognize anti-Iba-1 was AlexaFluor 488 Goat anti-Rabbit 1:1000 (Life Technologies; Carlsbad, CA, USA), which was also incubated for 24h. Finally, DAPI (1:1000; Life technologies; Carlsbad, CA, USA) was used to stain the nuclei of the cells. Sections were mounted on glass slides and coverslipped using Prolong antifade reagent (Invitrogen; Carlsbad, CA, USA).

Confocal microscopy, analysis and quantification

As with the human samples, mouse brain tissues stained by immunofluorescence were imaged with a confocal laser-scanning microscope (LSM 700, Carl Zeiss) utilizing a Plan-Apochromat 40x/1,3 Oil DIC M27 objective lens (Carl Zeiss) and processed with the ZEN 2010 software (Carl Zeiss). Three-dimensional reconstructions were generated using the α blending softwares ZEN 2010, Imaris (BitPlane, South Windsor, USA) and iLlucida FX (iLlucida LLC, Los Angeles, USA). Z-stacks were acquired to cover the depth of the tissue (25-30 images/stack) with a 0.5 μm step size. Raw images were imported into both Imaris (Bitplane Zurich, Switzerland) and Image J (version 1.4.3.67, NIH, USA) softwares, where they were further processed for morphometric analyses and cell counts. To better understand the gliapses, engulfments and phagocytic cups, Z-stacks were iso-surfaced using Imaris Surpass, this way we achieved three-dimensional representations of the microglia/macrophages and their targets.

In order to count the phagocytic events, 1 random slice per stack stained with Iba-1/PU.1/DAPI was imaged, randomly taking 5 confocal pictures per tumor. The images were imported to Image J (version 1.4.3.67, NIH, USA) to count the total number of cells, the amount of Iba-1$^+$ cells and its percentage (Iba1$^+$ cells/total cells), the and the amount of phagocytoses and its percentage (phagocytoses/Iba-1$^+$ cells) per slice.

Statistics

Regarding the human tissue, the number of cells in the palisades, the contacts and the phagocytic events were calculated from over 20 3D reconstructed multicolor z-stacks of the PPs along the tumor samples (Total 3D stacks, n=23). The detailed analysis of the cells' directionality, 3D individual cell-reconstructions, isosurface

rendering, morphology and MTOC position within PPs was scrutinized from 25 cells (n=25). In vitro, experiments for the study of the MTOC position with respect to the protrusion, and the cells' morphology were performed twice, while the time-lapsed cells tracked were 30 cells each experiment (n=30). Student's T test was used for dependent/independent samples and Mann-Whitney U test was used to compare data between groups. For instance, the cells' directionality was manually observed, and T-tests were performed to see if there was a statistical difference between the number of cells going towards or away from the necroses. The cells' perimeter and diameter in the tumors were given by the Imaris software when selecting individual cells, and the results were submitted to Kruskal-Wallis test with Dunn's multiple comparisons test, as the data did not follow a normal distribution. For the same reason, the number of nuclei, phagocytic events and the intercellular contacts in the human tissue, and all the parameters in the primary cultures were submitted to Kruskal-Wallis tests with Dunn's multiple comparisons test. The results of the microglial cells' morphology within PPs, as the kinetic differences between BV2 and GL261 lines, were analyzed by Student's T-test. Cells' persistence when time-lapsed was determined by Rayleigh test, where $p \leq 0.05$ indicated directionality.

On the in vivo experiments, the animals' survival was compared using Prism 6, by the survival curve comparison; while the comparison of the spleens' length, weight and organosomatic index, a Kruskal-Wallis test was carried out. As the N was limited (n=5/group), differences between the volume of the tumor under each treatment was also compared by a Kruskal-Wallis test, with Dunn's multiple comparisons test to see the differences between the groups. For the cells quantifications, when comparing Control, Isotype and treated groups a Kruskal Wallis test was performed; when comparing CD47 and SIRP groups, we carried out Student's T-test.

In all cases, $P \leq 0.05$ was considered significant. Graphs show the mean values obtained ± standard error of the mean. All statistical analyses were performed using Prism 6 software (GraphPad Software), except the Rayleigh test which was performed by ImageJ's chemotaxis plugin.

Results

Microglia/macrophages vary their distribution within microenvironments in GBM

We selected GBM samples from a cohort of biopsies obtained from patients who underwent surgery in the General Hospital of Valencia. While the Hospital provided us the Ki-67 proliferation index often correlated with the clinical course of the disease (**Appendix 1**), we counted the amount of vimentin in each of the samples, and ascertained by means of the Bland- Altman plot that both results did not differ from each other, meaning that more aggressive GBMs with a higher Ki-67 index, contain more vimentin **(Figure 3A)**. Once we knew this, we were able to correlate the amounts of Iba-1$^+$, CD163$^+$ and MHCII$^+$ cells by immunostaining these markers. This way, although we did not find more aggressive GBMs significantly displayed more cells of any type by means of Spearman's correlation ($p>0.05$), we did see a tendency of increasing numbers of immune cells in more aggressive GBMs **(Figure 3B)**. In order to see if this tendency was maintained in each microenvironment within the tumor, we classified images as belonging to one of the next microenvironments: perivascular, perinecrotic, pseudopalisading or, if none of these applied, as tumor parenchyma (TP). Precisely in the TP, the amount of anti-inflammatory CD163$^+$, Iba1$^+$, and pro-inflammatory MHCII$^+$ cells did not increase in a statistically significant way **(Figure 3C)**, although an increasing tendency was clear in the case of the pro-inflammatory marker. In areas near blood vessels, correlations between aggressiveness and number of cells showed a decreasing trend of Iba1$^+$ cells in more aggressive tumors ($r= -0.82$; $p<0.05$ vs. Vimentin; and $r=-0.79$ $p<0.05$ vs. Ki67 expression), and while MHCII expression was lowered in more aggressive tumors, CD163 increased but not significantly **(Figure 3D)**. Finally, in necrotic areas, again the aggressiveness of the tumor did not significantly vary the expression of these immune cell markers **(Figure 3E)**. In all, these results may indicate that the microenvironment exerts a high influence in the number and marker expression of immune cells, as the amount of each cell type varies differently depending on the microenvironment. Detailed statistic results are shown in **supplementary tables 1 and 2**. Nevertheless, given that the PPs contain a high number of cells and that the

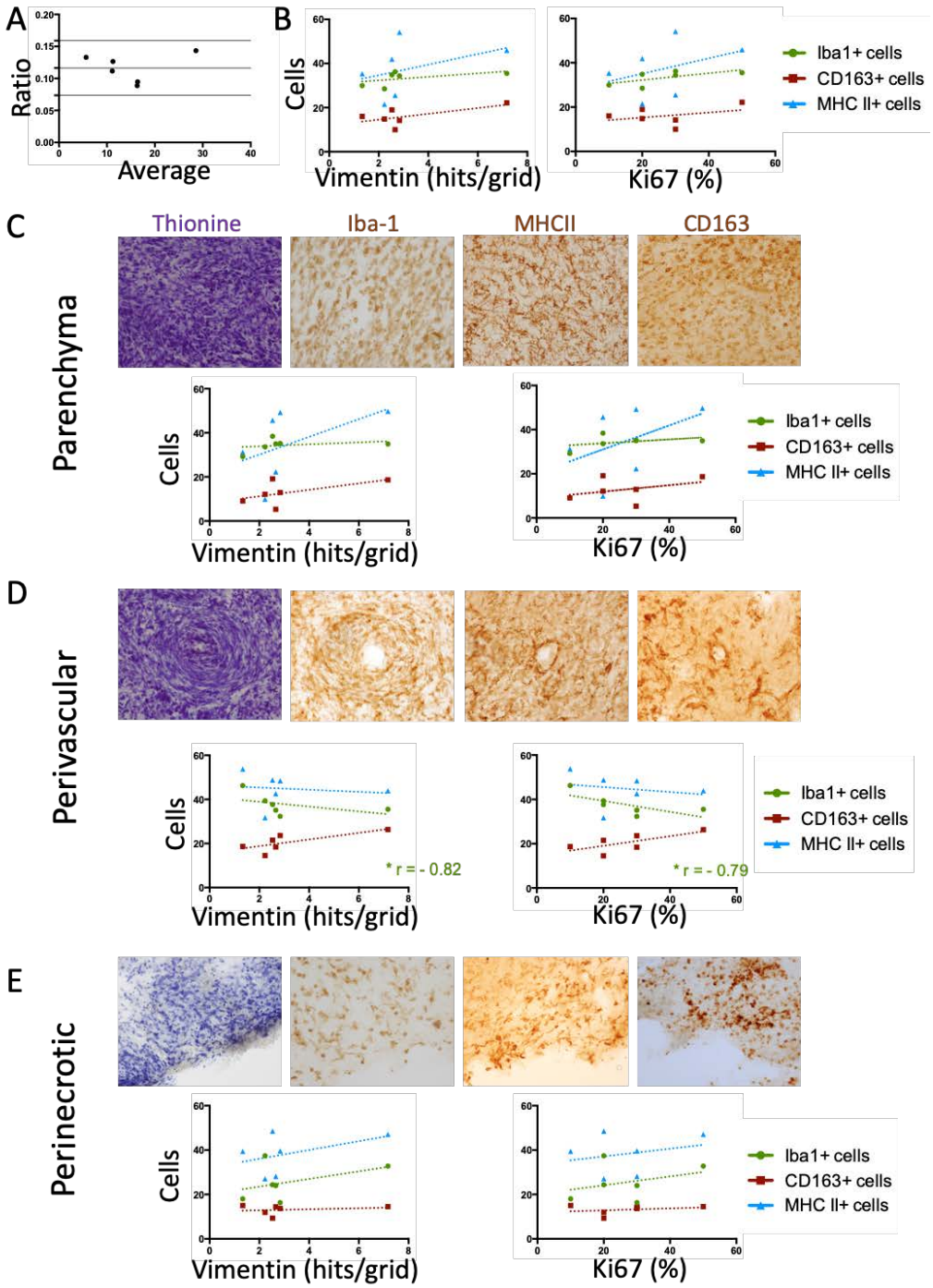

Figure 3. GAMMs subpopulations vary depending on the microenvironment. A. Bland-Altman plot evidencing no statistical difference between the quantifications of Vimentin and Ki-67 in the samples. B. Scatter plots with linear regressions show the correlation between the number of Iba1+, CD163+ and MHCII+ cells and the aggressiveness of the tumor, scored by the expression of vimentin and Ki-67 provided by the clinicians as neuropathological criterion. C. Parenchymatous areas were classified as tumor areas without necrosis, blood vessels, or pseudo-palisades. Typical hyperchromatism and pleomorphism is revealed by the thionine staining, while free-floating immunohistochemistry allowed us to estimate the number of Iba1+, CD163+ and MHCII+ cells in the area. Scatter plots with linear regression revealed the relationship between the number of Iba1+, CD163+ and MHCII+ cells and the aggressiveness of the tumors. D. Iba1+, CD163+ and MHCII+ cells were also counted in areas where we could find blood vessels, which often were glomeruloid; and correlated with the aggressiveness of the tumor (vimentin and Ki-67), r indicating a negative and significant (*p<0.05) correlation. E. Necrotic areas were tagged when there was a lack of consistency in the tissue and/or there were erythrocytes without being a blood vessel nearby, as shown in with the thionine staining. Again, immune cells were counted and correlated with the aggressiveness of the tumor (vimentin and Ki-67 index).

individuality is lost if regarded by simple brightfield microscopy, we did a more exhaustive analysis by immunostaining the cells with fluorescent secondary antibodies.

Microglia/macrophages densely populate PPs in human GBM

First off, since PPs are considered as a critical environment for the invasion of the tumor, from the selected GBM samples, and based on the histological features, we confirmed the presence of canonical PPs in the tissue sections by Nissl staining **(Figure 4A)**. Necrotic PPs were identified by a hyper-cellular area (HA), well organized and distributed surrounding a necrotic focus (NF) with a central blood vessel expressing the basement membrane marker collagen IV. By staining the nuclei, the HA was revealed, where there were also GFAP immuno-reactive cells demonstrating the presence of malignant cells **(Figure 4C)**. Serial sections of the tumors with identifiable PPs were stained for several microglial/macrophage markers (Iba-1, CD163 and MHCII), as well as for a general marker for T lymphocytes (CD3). Iba-1 and CD163 immunohistochemistry showed cells clearly belonging in the PPs at the HA, demonstrating the big proportion of the immune component of the PPs **(Figure 4 B, D)**. However, MHCII staining did not reveal an evident palisade outline, being patent outside the HA at the necrotic borders (**Figure 4 D**). In addition, T cells were only limited to the blood vessel surroundings but absent from the HA of the PPs (**Figure 4 H**).

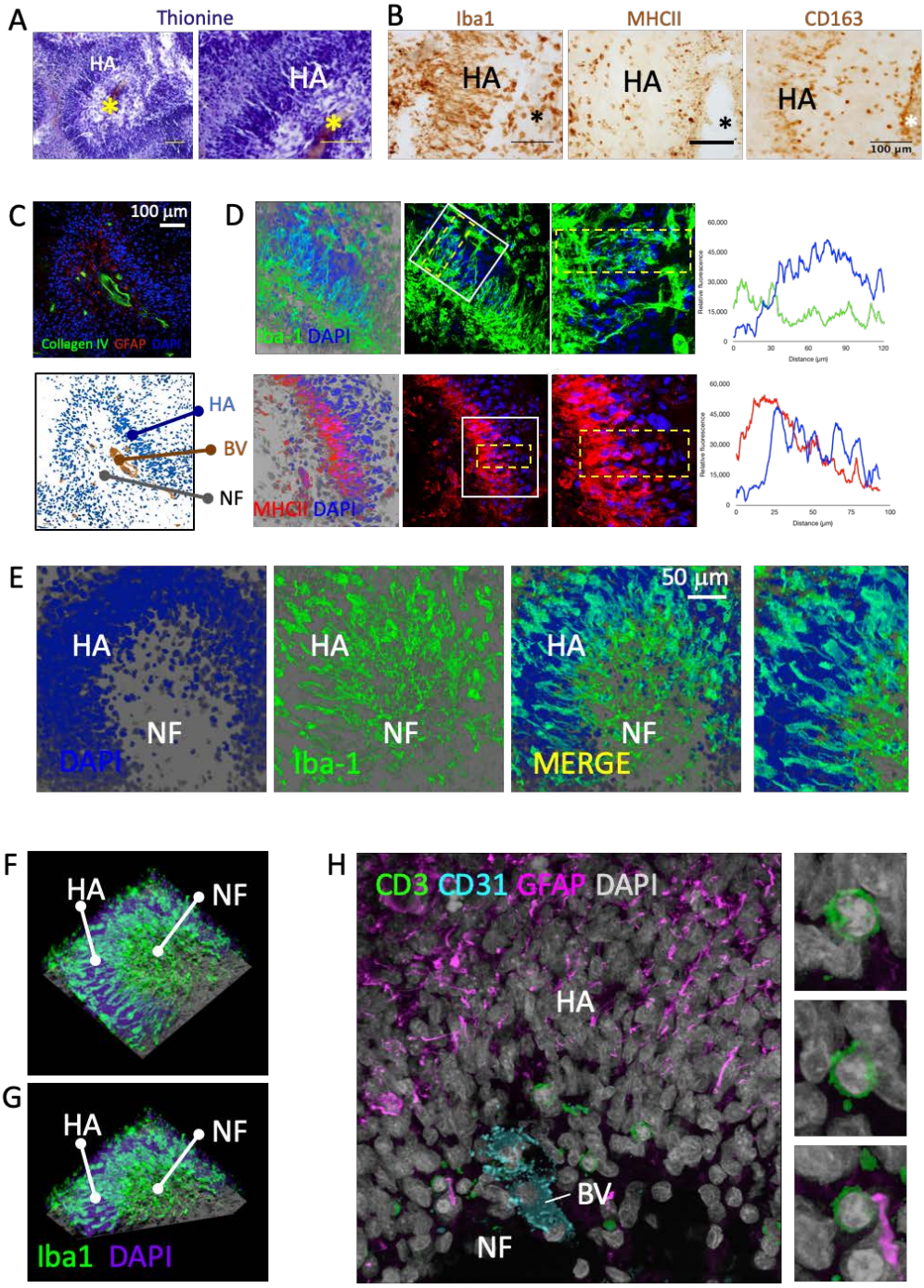

Figure 4. GAMM abundantly populate PPs in GBM. A. Thionine-based Nissl staining evidences necrotic PPs with central blood vessel (*) in GBM samples. Scale bar= 100 um. B. Adjacent histological sections show a dense population of elongated Iba-1$^+$ and CD163$^+$ in addition to MHCII$^+$ staining. Elongated GAMMs within the anti-inflammatory spectrum (CD163$^+$) can be seen at the HA as opposed to the low frequency of the pro-inflammatory spectrum (MHCII). C. Confocal image and diagram of a classic PPs structure, containing hypercellular area (HA), central blood vessel (BV) and necrotic focus (NF). [Diagram based on confocal image with characteristic architecture of a PP]. BV identified by Collagen IV (green) is located at the center of the NF. Malignant tumor cells, identified by GFAP (red) appear in a centrifuging manner, escaping from the necrotic area. A clear accumulation of DAPI$^+$ nuclei (blue) can be appreciated forming the palisading arrangement. D. Maximum projections of PPs containing either Iba-1$^+$ (green) of MHCII$^+$ (red) cells. Fluorescence profile plots of rotated zoom-ins show that while Iba-1 expression remains constant throughout the PP, MHCII expression emerges at the P of the HA. E. Confocal image reconstruction shows that the area of high density of DAPI$^+$ nuclei (blue) (HA) is densely populated by Iba-1$^+$ microglia/macrophages. F. 3D reconstruction of the PP (shown in panel E) displays elongated Iba-1$^+$ cells at the HA. G. 3D reconstruction from E with a central clipping plane to better visualize elongated cells at the HA. H. Representative confocal image of a human PP to visualize CD3$^+$ T cells (green), GFAP$^+$ tumor cells (magenta), and DAPI$^+$ cell nuclei (grey), surrounding the vascular NF. CD31 was used for visualizing the BV. T cells appeared limited to the surroundings of BV at the NF and no T cells were identified at the HA.

Transparent 3D reconstructions of the tissue blocks allowed the visualization of elongated GAMMs crossing the HA areas (**Figure 4 E-G and Supplementary Video 1**). Furthermore, we compartmentalized the HA of the PPs in three regions: proximal (P) to the NF; intermediate (I); and distal (D), the latter appearing close to the malignant TP; and quantified the proportion of Iba-1$^+$ GAMMs and GFAP$^+$ malignant cells (**Figure 5**). This way, we observed a differential distribution of cells within the HA, being the density of GAMMs higher at the P region contrasting with malignant cells, which were more scarce in this area (**Figure 5 and Supplementary Video 2**).

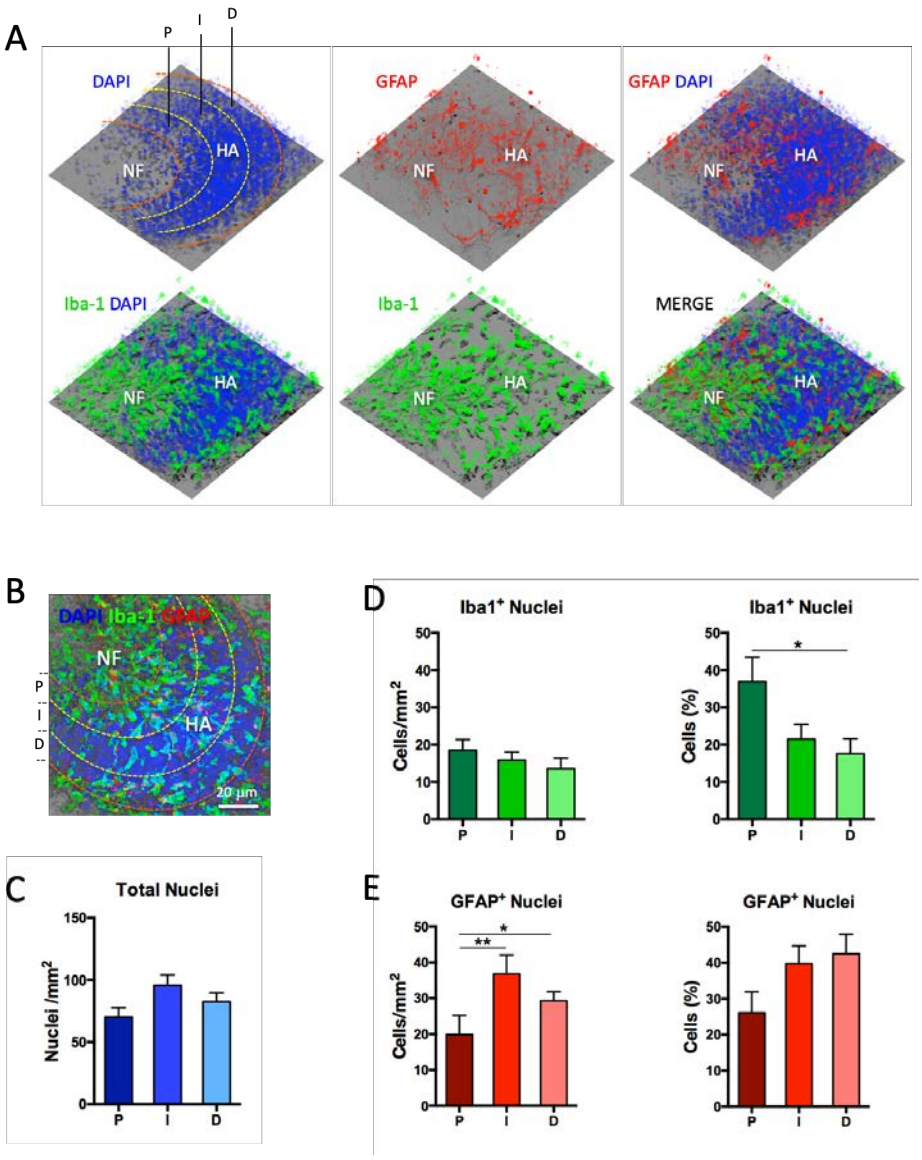

Figure 5. Differential distribution of microglia/macrophages and tumor cells within PPs. A. 3D reconstructions of a representative human tissue block at a PP. Images were captured containing the necrotic focus (NF) and hypercellular area (HA), which was divided in proximal (P), intermediate (I), and distal (D) regions. B. Zenithal view of the reconstruction and areas of quantification. C. Estimation of nuclei per stereological dissector in the HA of PPs. D. Estimation of Iba-1$^+$ nuclei (left) and percentage from the total nuclei (right). E. Estimation of GFAP$^+$ nuclei (left) and percentage from the total nuclei (right).

Microglia/macrophages become elongated in hypoxic conditions.

Since GAMMs at the HA showed elongated morphology distinct from an amoeboid morphology found elsewhere (**Figure 6 A and B**), we hypothesized that this environment, essentially characterized by hypoxia (7), yet coexistent with hypoglycemia, might induce the morphological change. Thus, we set up an *in vitro* experiment with microglial and glioma cell lines to analyze morphometric parameters of the two cell types under these conditions. Our experiments revealed that microglial cells, in contrast with glioma cells, become patently elongated in hypoxic environments suggesting a different motility pattern in these settings, compatible with the palisade-like arrangement (**Figure 6 B-G**). Contrarily, after hypoglycemic conditions, although GL261 glioma cells did become elongated, no changes in elongation were seen in microglial cells (**Figure 7**). Thus, we focused on hypoxic conditions for studying microglial kinetics. In order to know whether elongated morphology coincides with cell motility, we analyzed in time-lapse the behavior of microglia. Importantly, microglial cells in movement adopt a particular shape when traveling, characterized by an extended structure, the formation of a protruding leading lamella and a trailing uropod (**Figure 8 A-C and Supplementary Video 3**). F-actin staining evidenced the actin-rich lamella and the kinetic shape of microglial cells. Quantification and detailed analyses revealed an apparent increase of kinetic morphology of microglia under hypoxic, in contrast with hypoglycemic conditions (**Figure 8 E-F**). Differently, no significant changes were seen in glioma cells (**Figure 9**). Since the position of the microtubule-organizing center (MTOC) is potentially oriented towards the leading edge in migrating cells (151–153), we also labeled the MTOC, rich in γ-tubulin, to analyze its positioning with respect to the leading protrusion (**Figure 8**). We observed that the positioning of the MTOC in kinetic cells was preferentially located adjacent to the leading edge in contrast to opposite (back) position (**Figures 8 D, G-H and 9**), indicating that the motility of microglial migrating cells encompasses this MTOC positioning. Importantly, this location was maintained under hypoxic conditions suggesting that the motility and directionality of microglia is run by this centriole position.

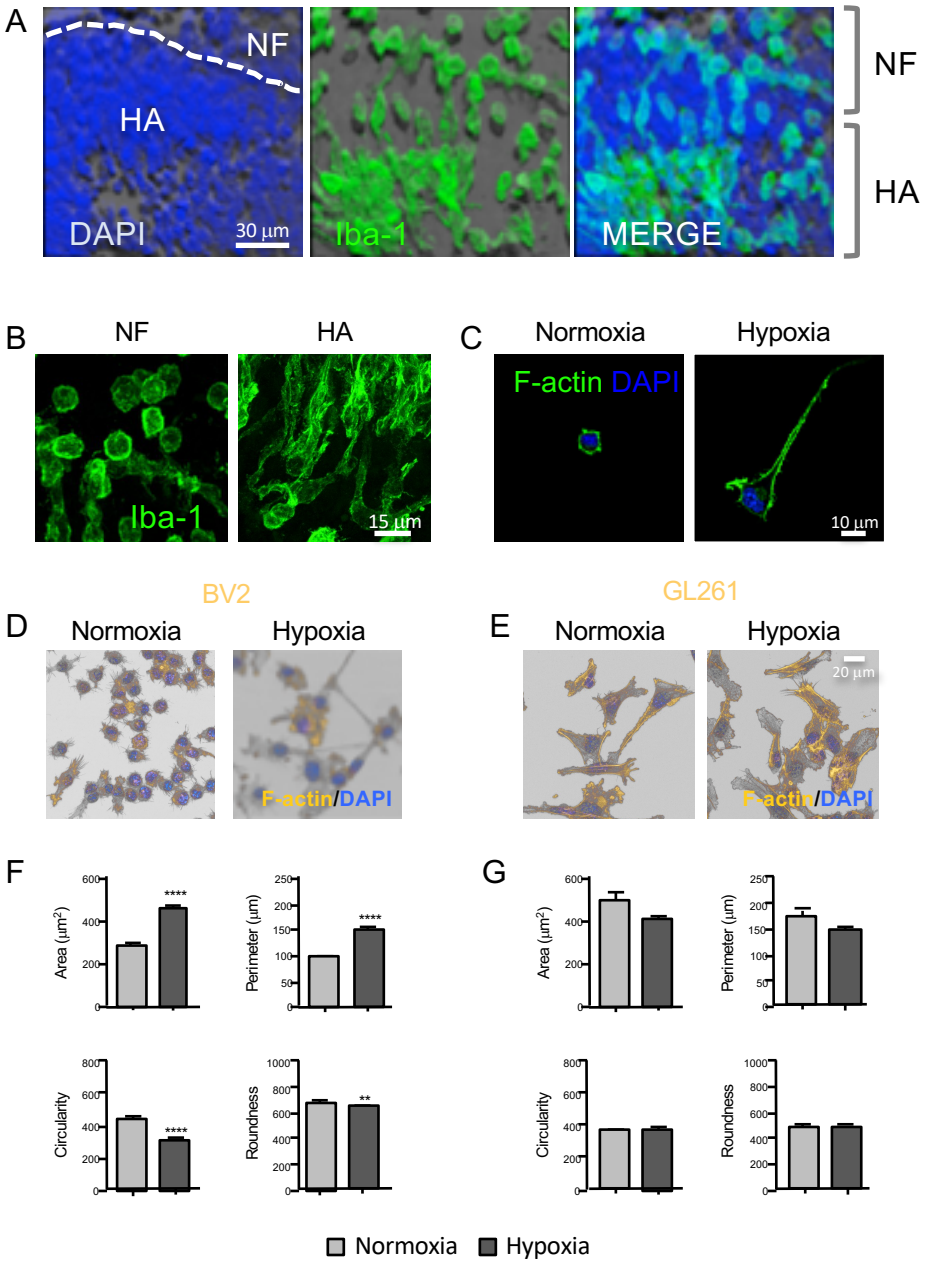

Figure 6. Microglia adopt elongated morphology in hypoxic conditions. A. 3D reconstruction of a human GBM PP containing Iba-1^{+} TAMM within the palisading hypercellular area (HA) and necrotic focus (NF). B. Detail of morphological differences between Iba-1+ cells from NF and HA from human GBM. C. BV-2 microglial cells show elongated shape under hypoxic conditions. D. Representative confocal images of BV-2 cells in normoxia and hypoxia. E. Representative images of glioma cells in normoxia and hypoxia. F. BV-2 microglial cells, in contrast with non-myeloid GL261 cells, show increase in cell size, perimeter and elongated morphology 24 h after hypoxic treatment. G. No significant differences in morphometric parameters were seen in glioma cells.

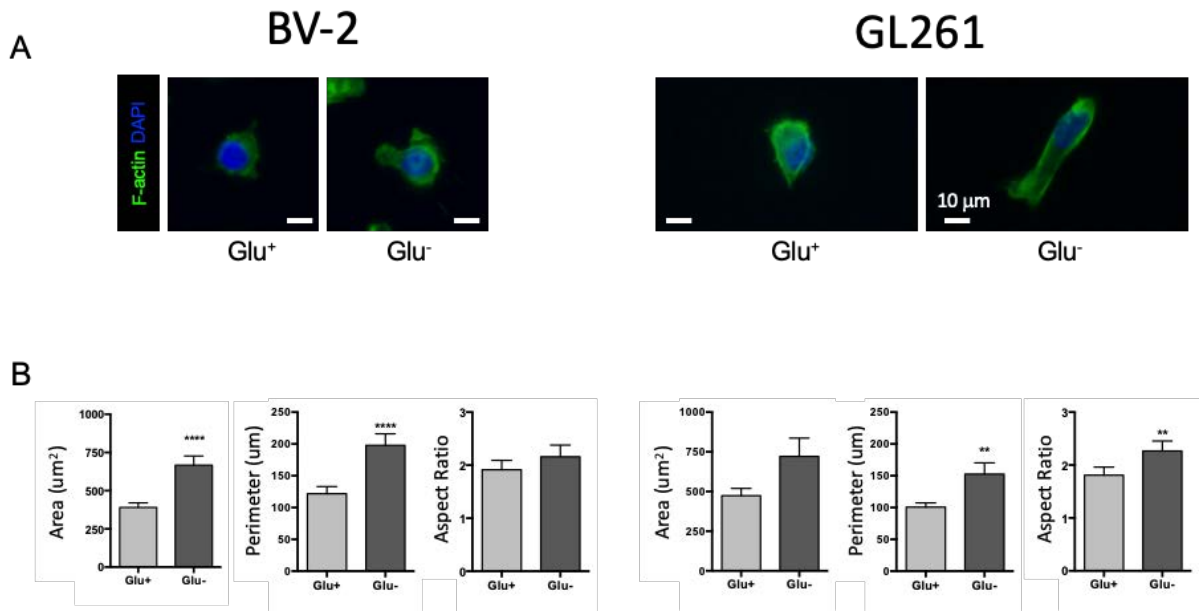

Figure 7. Microglia is not elongated under hypoglycemic conditions. A. Representative epifluorescence images of BV-2 and GL261 cells cultured in normoglycemic (Glu^+) and hypoglycemic conditions (Glu^-); stained for F-actin and nuclei counterstained with DAPI used for the quantification of morphometric parameters. Scale bar= 10 µm B. Quantification of area, perimeter and aspect ratio did not reveal significant changes in the elongation (Aspect Ratio) in microglia when exposed to the absence of glucose. Slight but significant changes were seen in glioma cells.

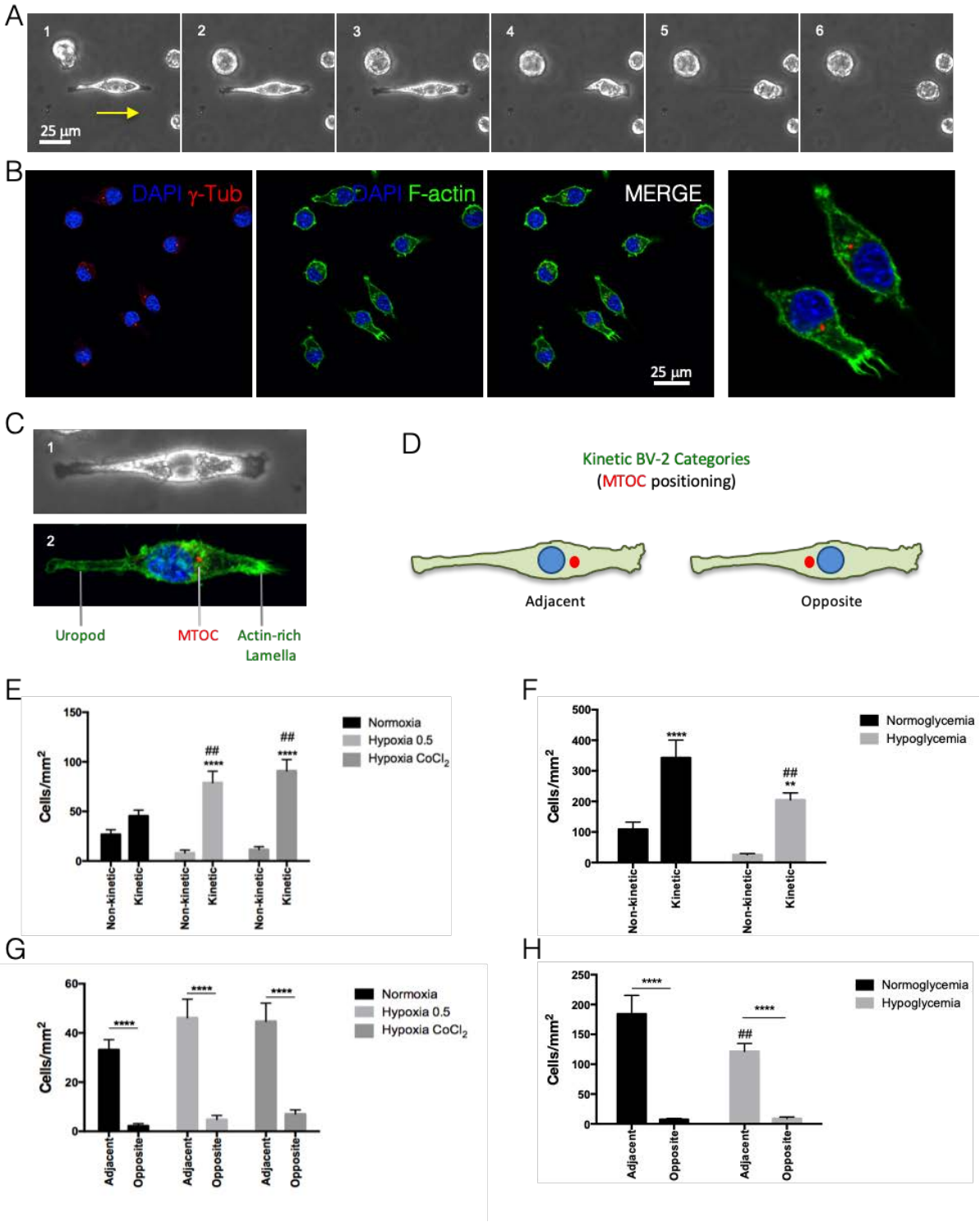

Figure 8. Hypoxia induces oriented kinetic morphology on microglia. A. Time-lapse video reveals the steps that microglial cells undergo when migrating in contrast with neighboring static cells. B. Confocal analysis of microglial kinetic morphology evidenced by F-actin (green), g-Tubulin (red) and nuclei counterstained with DAPI (blue). C. (1) Microglial cell in kinetic movement from time-lapse video frame. C. (2) Maximum intensity projection of kinetic microglia showing an actin-rich lamella, a trailing uropod and the g-Tubulin-rich MTOC. D. Categories of MTOC position (Adjacent or Opposite) in relation to nucleus and leading lamella in kinetic microglia with an aspect ratio over 2. E. Quantification of non-kinetic and kinetic microglia in normoxia versus hypoxia. **** p<0.001 vs. non-kinetic; ## p<0.01 vs. kinetic in Normoxia. F. Quantification of kinetic and non kinetic morphology in hypoglycemic and normoglycemic conditions. Asterisks indicate significance if compared with non-kinetic in the same conditions; and octothorps with kinetic in normoglycemia (four symbols p<0.001; two symbols p<0.01) G. Quantification of MTOC position in kinetic cells in normoxia and hypoxia. **** p<0.001. H. Quantification of MTOC positioning in kinetic microglia in glucose-rich medium versus hypoglycemia. **** p<0.001 comparing adjacent vs. opposite; ## p<0.01 comparing adjacent in both conditions.

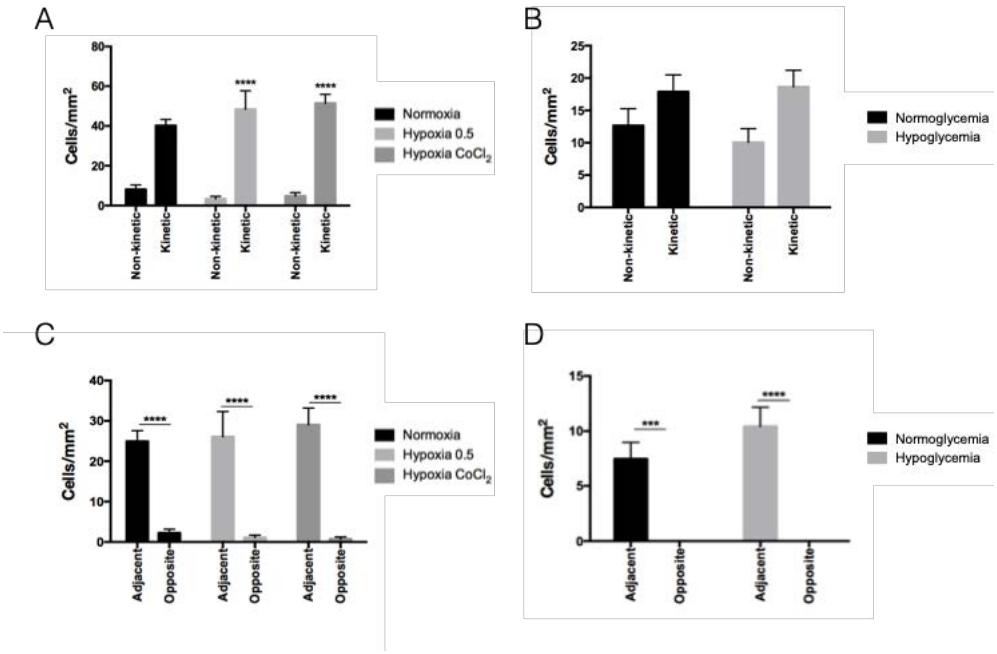

Figure 9. Hypoxia and hypoglycemia do not vary the proportion of GL261 with kinetic morphology. GL261 glioma cells maintain similar morphological ratio of kinetic and non-kinetic morphologies under hypoxia, when compared to normoxic conditions (A), and under hypoglycemia, when compared to normoglycemic conditions (B). The MTOC position is kept adjacent to the protruding lamella in all conditions, including hypoxia (C) and glucose deprivation (D). **** p<0.001; *** p<0.005 between categories in the same conditions.

Microglia/macrophages in PPs show preferential cellular orientation towards necrosis location.

Once knowing the leading MTOC position adopted in kinetic-elongated microglial cells under hypoxic conditions, we analyzed in 3D the location of MTOC in GAMMs within the PPs of human GBM samples to unravel their preferential orientation. We analyzed with high resolution and Z-depth the HA of the PPs separating P, I, and D regions, according to the NF position (**Figure 10 A**). We generated specific 3D isosurfaces and spots in imaging software to locate the orientation of the MTOC (**Figure 10 and Supplementary Video 4**). Our 3D reconstructions show that GAMMs become bigger at the I area (**Figure 10 D**) and preferentially orienting the MTOC towards the NF at I and D regions (**Figure 10 and Supplementary Video 5**), indicating that GAMMs preferentially migrate to the NF. Interestingly, GAMMs at the P area do not show a preferential directionality suggesting that they may have reached their target location (**Figure 10 F**).

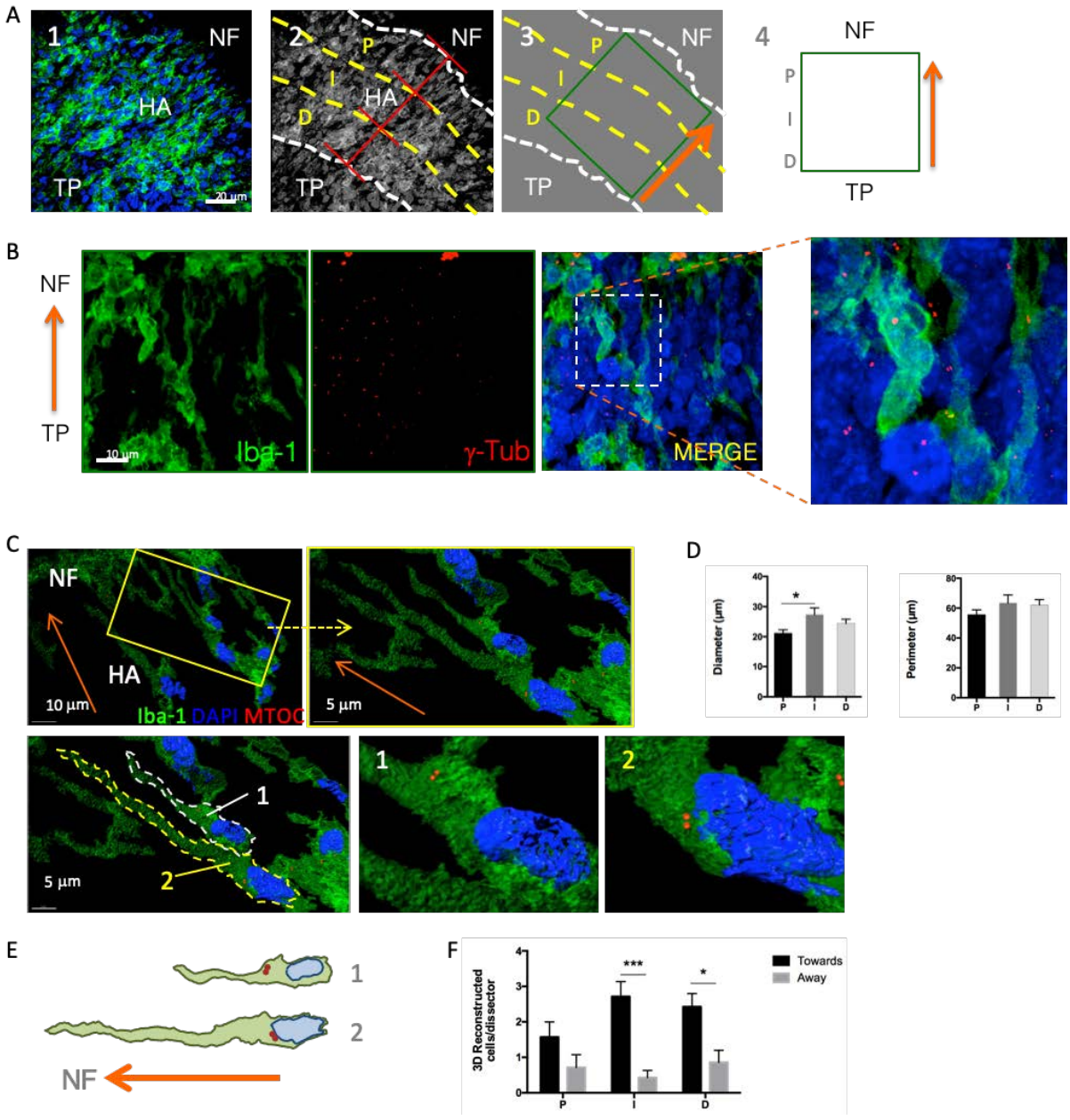

Figure 10. Analysis of MTOC position in GAMMs in relation to the NF within PPs. Human samples stained for Iba-1 and g-Tubulin were analyzed with 3D-high resolution confocal microscope. A. Confocal image of a representative HA of a necrotic PP between the TP and NF limits (1). Separation of P, I, and D areas in relation to NF proximity (2). The scanning field at HA was set up rotating the x and y axis of the system (green square) according to the NF and TP orientation (orange arrow) (3). Images were analyzed with this criteria of orientation (4). B. Representative confocal image of microglia/macrophages labeled with Iba-1 (green), g-Tubulin (red) and DAPI+ nuclei (blue) within the HA of the PPs. At the higher magnification of the MERGE the MTOC can be identified as g-Tubulin accumulations. C. Cells could be rendered in 3D to visualize the shape and MTOC position regarding the nucleus and NF location. Representative cells are indicated by 1 and 2. D. Quantification of diameter and perimeter of Iba-1 cells at the PPs show a significant increase of the size at the intermediate area compatible with elongated shape seen in vitro. E. Diagram of representative cells (1 and 2) with prevalent MTOC orientation. F. We defined the MTOC position towards the NF or the TP in proximal (P), intermediate (I) and distal (D) areas. The quantification of the percentage of cell orientations shows that the majority of cells are oriented towards the NF except in the P area. *p<0.05; ***p<0.005.

Microglia show cellular persistence under hypoxic gradient.

Since the directionality of GAMMs at the HA in human PPs is mostly leading towards the NF, we set up an *in vitro* gradient experiment to know if a hypoxic gradient induces changes in microglial migratory behavior. We observed that hypoxia induces a significant escape of glioma cells towards normoxic media as previously demonstrated by others (7), which corroborates the centrifugal characteristics of glioma invasion. In contrast, microglial directionality is not changed either towards normoxia or hypoxia although their motility seems to be affected by the set up gradient (**Figure 11, Supplementary Videos 6-9**), as cells migrate in a different way. Microglial cells appear clearly elongated and navigate in a straighter manner, defined by the significant increase of the Euclidean distance ($p<0.05$). Thus, microglial cells increase their cellular persistence when exposed to a hypoxic gradient, which explains the elongation at this setting and clarifies the non-centrifugal behavior at the PPs.

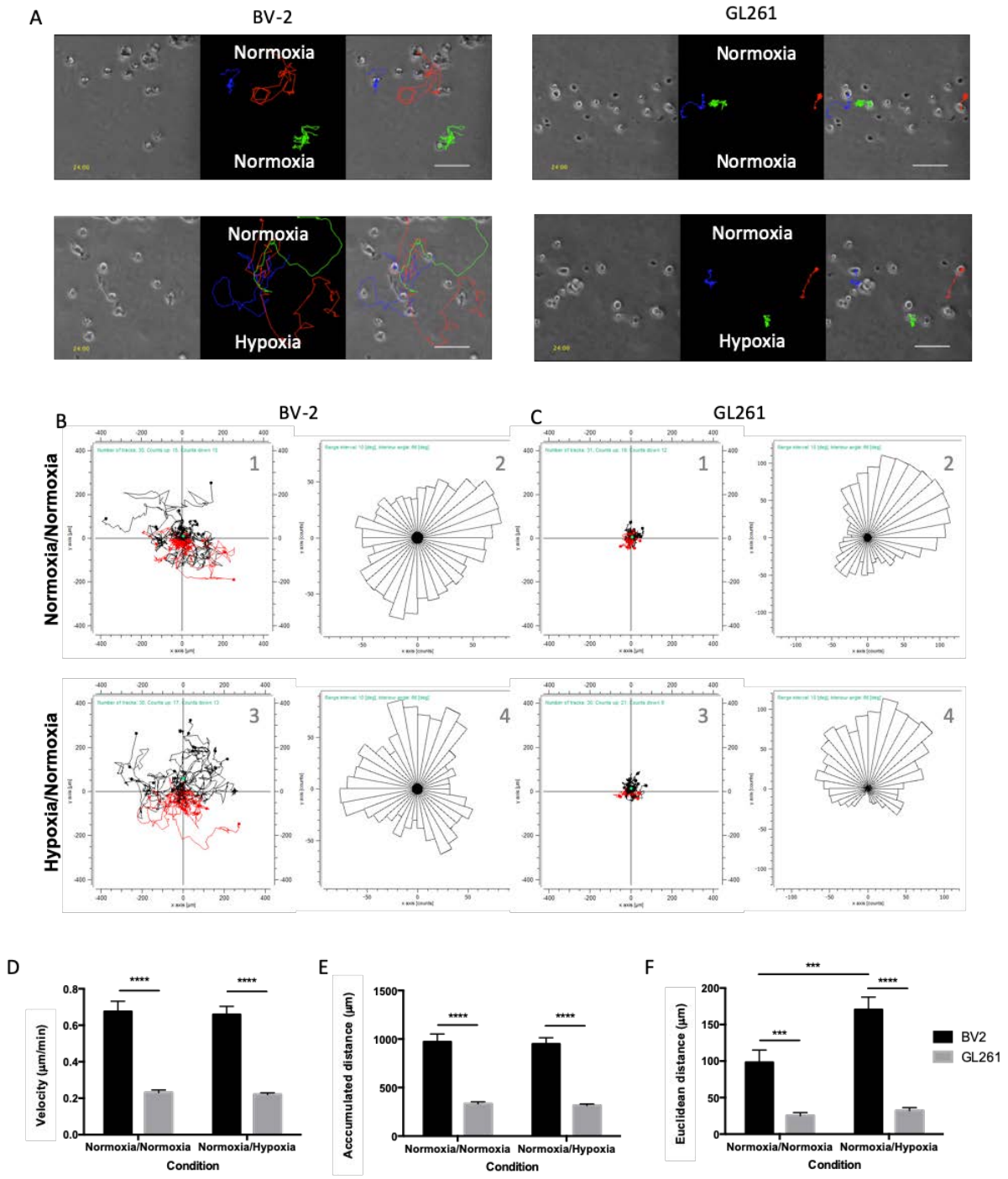

Figure 11. Microglia does not escape from hypoxia and navigates straightly. A. Contrast images of microglia and malignant tumor cells under normoxic non-gradient conditions and under a hypoxic gradient were taken every 5 minutes for 24h, the final frame is shown in the left panel. 30 cells per condition were followed and the path or three representative cells is exposed in the middle panel, and merged in the third panel for each condition and cell line. Scale bar = 50 um. B. Microglia behave similarly when exposed for 24h to normoxic (representative cell trajectories in plot graph 1, and distribution of migrating angles in rose graph 2) and hypoxic conditions (analogous representation of cell tracks in 3, and rose graphs in 4). Black tracks are cells ending in the upper quadrant while red tracks are cells ending in the lower quadrant. C. Glioma cells migrate away from hypoxic conditions. When comparing the exposure to normoxic media (1 and 2) and hypoxic gradient (3 and 4) during 24h, glioma cells move away from the hypoxic source. Green dots in the graphs (1 and 3) represent the center of mass. Rayleigh test for directionality revealed a significant directionality only for glioma GL261 cells ($p<0.01$ [$p = 0.00282$) towards normoxia in contrast with microglial BV-2 cells. In all cases, microglia show higher motility, migrating with higher velocity (D) and traveling longer distances (E) than glioma cells. F. Although hypoxia-normoxia gradient does not modify the velocity and accumulated distance, microglia show higher Euclidean distance, meaning that they migrate straighter when there is a hypoxic gradient.

Microglia/macrophages interact haptotactically with malignant cells

To further understand the strategy of microglial cells to navigate the HA of the PPs, we analyzed the potential interactions of GAMMs with malignant cells. We analyzed in 3D and high-resolution detail, the combined GFAP/Iba-1 immunofluorescence staining. We observed $GFAP^+$ cells displaying a fibrous anisotropic nature at the PPs (**Figure 12 A**), in contrast with the isotropy found in other areas, and GAMMs frequently contacting $GFAP^+$ material at the HA, sharing a similar anisotropic orientation (**Figure 12 and Supplementary Video 10**). These intercellular contacts appeared higher at the I area (**Figure 12 E**), implying the haptotactic traveling of GAMMs through the HA. These intercellular appositions seem to be critical since 100% of GAMMs at the I of the HA were interacting with GFAP fibers (**Figure 12 G and Supplementary Videos 11 and 12**). Interestingly, the interactions were established with the tumorigenic GFAP fibers both perpendicular and longitudinal to the NF (**Figure 12 I**). Quantifications revealed that longitudinal appositions were significantly longer than the perpendicular ones demonstrating the joined anisotropic orientation of GAMMs and $GFAP^+$ malignant fibers (**Figure 12 and Supplementary Video 12**). These results imply that GAMMs may utilize the elongated $GFAP^+$ fibers of the PPs to migrate towards the NF and together with the differential $GFAP^+$ density along the HA (previously shown in **Figure 5**), suggests that haptotaxis could be a crucial strategy of cell motility in this microenvironment.

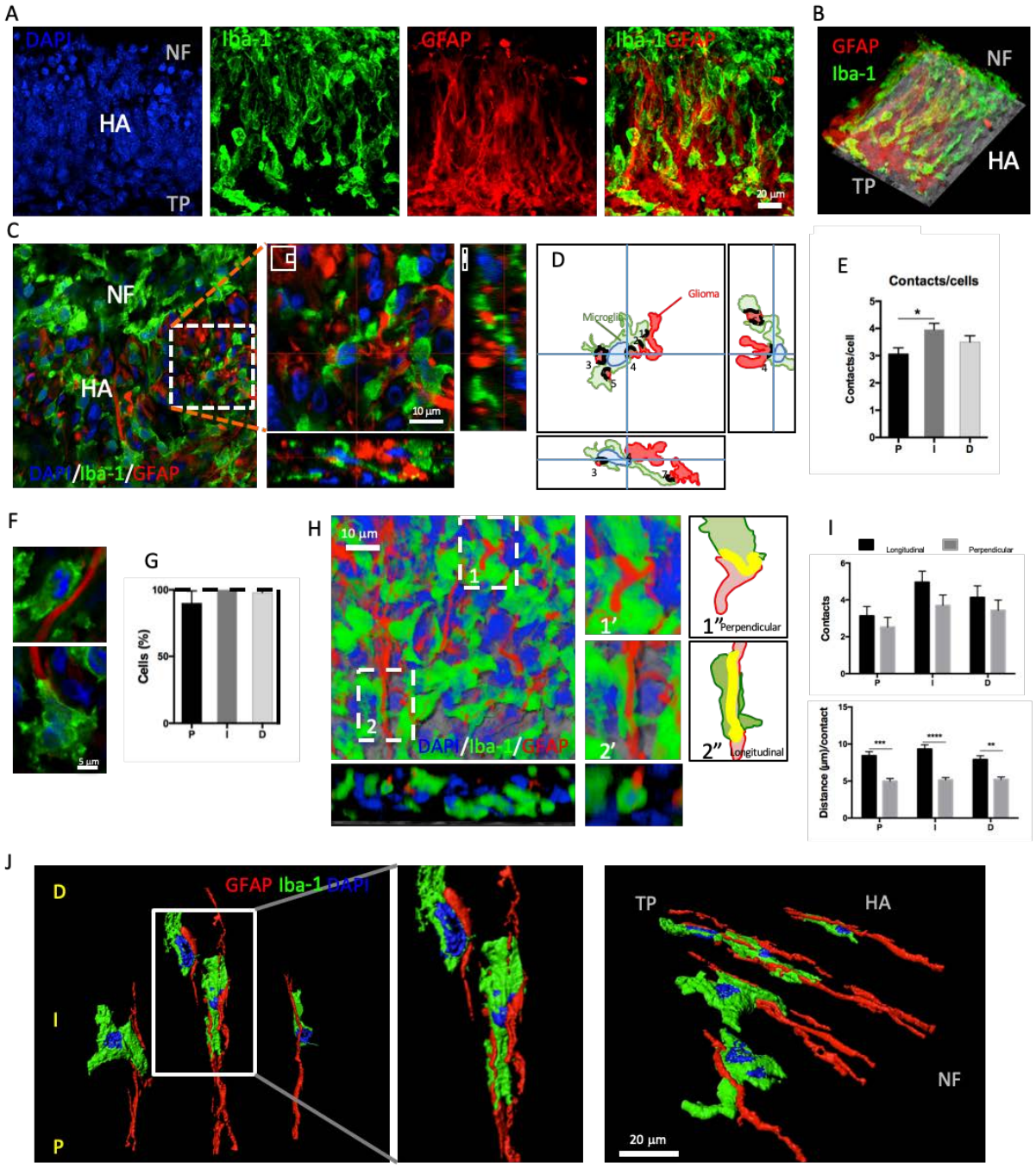

Figure 12. Haptotactic interaction of GAMMs at the human pseudo-palisades. A. Representative PP confocal scanning of nuclei (DAPI), GAMM (Iba-1) and malignant glioma cells (GFAP) at the HA limited by the NF and TP. B. 3D reconstruction of the image shown in A. C. Confocal visualization of GAMM at the HA near the NF limit. Higher magnification of broken white square is displayed to the right to show GAMM interacting with malignant cells in different optical planes indicated in orthogonal views at the Z planes. D. Diagram representing the analysis of Iba-1-GFAP interactions based on panel C including the orthogonal views. E. Quantification of the number of interactions with GFAP per Iba-1+ cell at the P, I and D areas. The number of contacts is significantly increased at the I area. F. Representative Iba-1 cells interacting with fibrous GFAP cells at the PPs. G. Quantification of the percentage of Iba-1 cells establishing contacts with malignant GFAP cells at the HA of the PP. H. 3D reconstruction of Iba-1 and GFAP interactions at the HA. Representative perpendicular (1) and longitudinal (2) interactions are indicated in white broken line squares which are shown in higher magnifications in 1' and 2'. Orthogonal view at the level of the longitudinal interaction is shown. Illustrations of perpendicular and longitudinal interactions are shown in 1" and 2". I. Quantification of the number and distance of longitudinal and perpendicular contacts at the P, I and D areas. J. 3D reconstruction of TAMM within the HA of a human PP in apposition to GFAP fibrils. Zoom from white rectangle in is shown. Oblique view is shown in image on the right.

Microglial phagocytic events increase at the P regions of the HA

Since the haptotactic migration of GAMMs at the PPs is polarized towards the NF, we wondered about the physiological relevance of reaching this area. Considering the scavenging and phagocytic capacity of GAMMs, we explored and imaged with high-resolution the phagocytic events along the PPs. We observed events of GAMMs phagocytosing pyknotic nuclear material (**Figure 13 A-C**) and $GFAP^{+}$ fragments (**Figure 13 D, 14**). Phagocytic GAMMs, detected by Iba-1 immunolabeling, were identified by having a $DAPI\text{-}^{low}$/$Iba\text{-}1^{+}$ nucleus, and contained a contiguous $Iba\text{-}1^{-}$ space, the phagosome, containing $DAPI\text{-}^{high}$/$Iba\text{-}1^{-}$ elements, $GFAP^{+}$ material, (**Figure 13 and Supplementary Video 13**) or even both at the same time (**Figure 14 and Supplementary Video 14**). Careful examination of the samples and quantification showed a differential frequency of phagocytic events within the three areas of the HA, being significantly higher at the P area (**Figure 13 H**). These results indicate that GAMMs actively cross the HA of the PPs searching for cellular elements to be engulfed and eliminated.

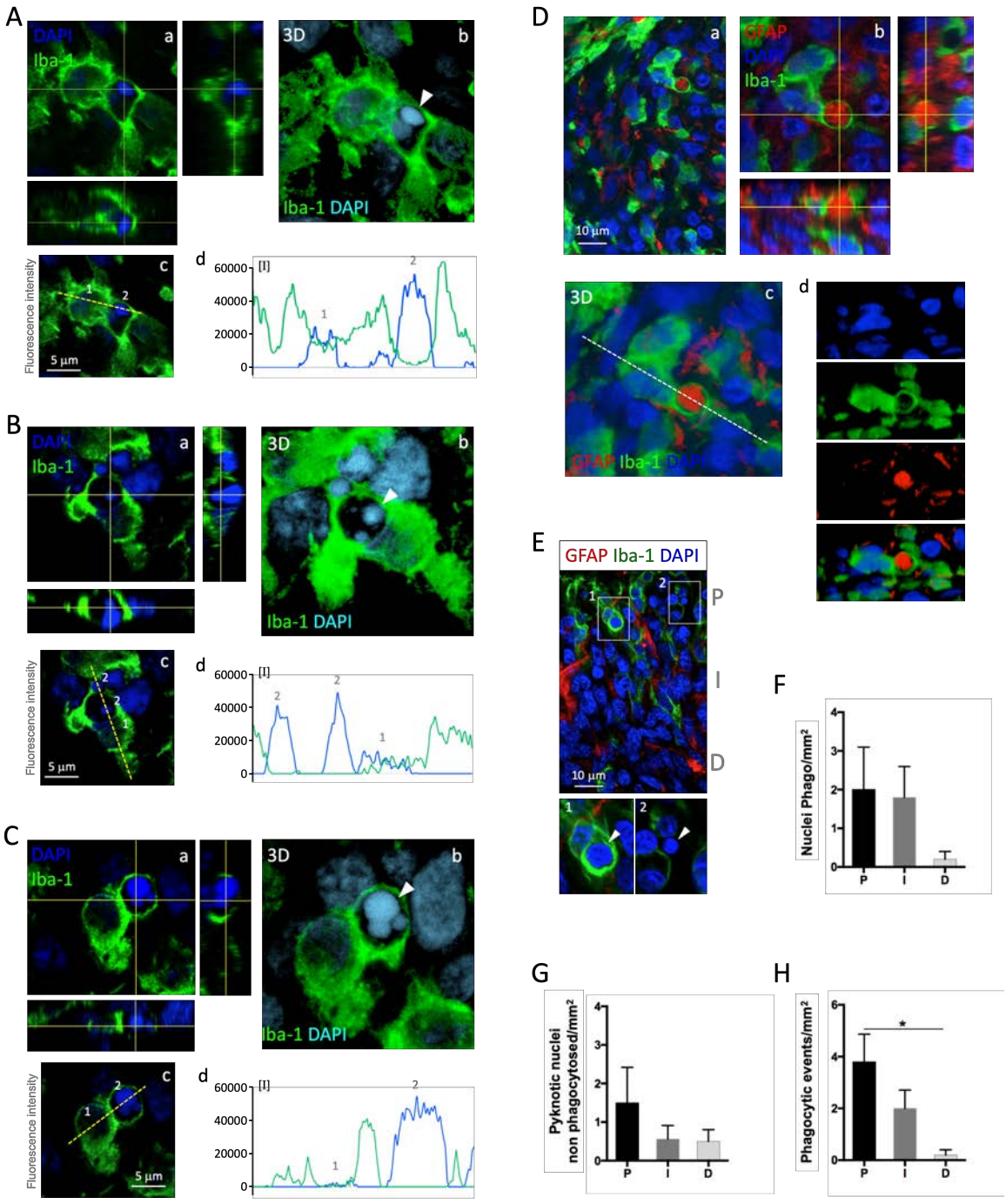

Figure 13. GAMM increase phagocytic capacity at the NF proximity. A. Engulfing GAMM at the human PPs evidenced with Iba-1 and DAPI. Nuclei with pyknotic characteristics could be seen in Iba-1- space. Orthogonal views evidenced the engulfing along the z stack (a). 3D reconstruction at central clipping plane show the phagosome containing pyknotic nuclei (arrowhead) surrounded by Iba-1 (b). Analysis of relative fluorescence intensity was measured along yellow broken line (c). Plot profile from c is shown in d. Nuclei (normal, 1 and pyknotic, 2) are indicated in the profile plot (d). Analogous examples of phagocytosis are shown in B and C (In plot profiles 1 is for regular nucleus and 2 for pyknotic nuclei). D. Phagocytosis of GFAP+ material at the human PPs. Confocal overview of the HA stained for Iba-1, GFAP and DAPI (a). Detail of a phagocytic event from the P region of the HA and orthogonal views at the indicated planes (b). 3D visualization at central clipping plane showing GFAP material at the phagosome (c). Lateral view of the phagocytic event from clipping plane shown in c with white broken line (d). E. Example of a HA of a PP indicating the P, I and D areas. Pyknotic nuclei can be detected phagocytosed (1) or isolated (2), especially at the P and I regions. F. Quantification of phagocytosed nuclei in P, I and D. G. Quantification of isolated pyknotic nuclei in P, I and D. H. Estimation of the frequency of phagocytic events in P, I and D.

P65 NF-κB is not translocated in glioma-associated microglia/macrophages

Being p65 NF-κB a key molecule in triggering inflammation and, potentially, mediating phagocytosis, we decided to check if it was expressed and translocated in GAMMs in human GBM samples. Although phagocytosis was clearly taking place (**Figures 13-14**), p65 expression was not evident at the NF but only expressed at the TP (**Figure 15 A**) of PPs by non-myeloid cells. Precisely, we took a closer look at phagocytosing cells and saw that $MHCII^+$ cells phagocytosing pyknotic nuclei did not express p65 NF-κB (**Figure 15 B**). In order to further confirm this and amplify the staining, DAB immunohistochemistry was also performed (**Figure 15 C, D**). While p65 NF-κB was expressed in elongated cells with a tumor cell-like morphology and with no MHCII expression, MHCII was highly expressed in rounded/ameboid GAMMs. Moreover, in the regions where both markers were clearly present we could see poor, if any, p65 expression in $MHCII^+$ cells with no p65 nuclear translocation, what could suggest that they may have lost their proinflammatory identity, having their phagocytic capacity impaired.

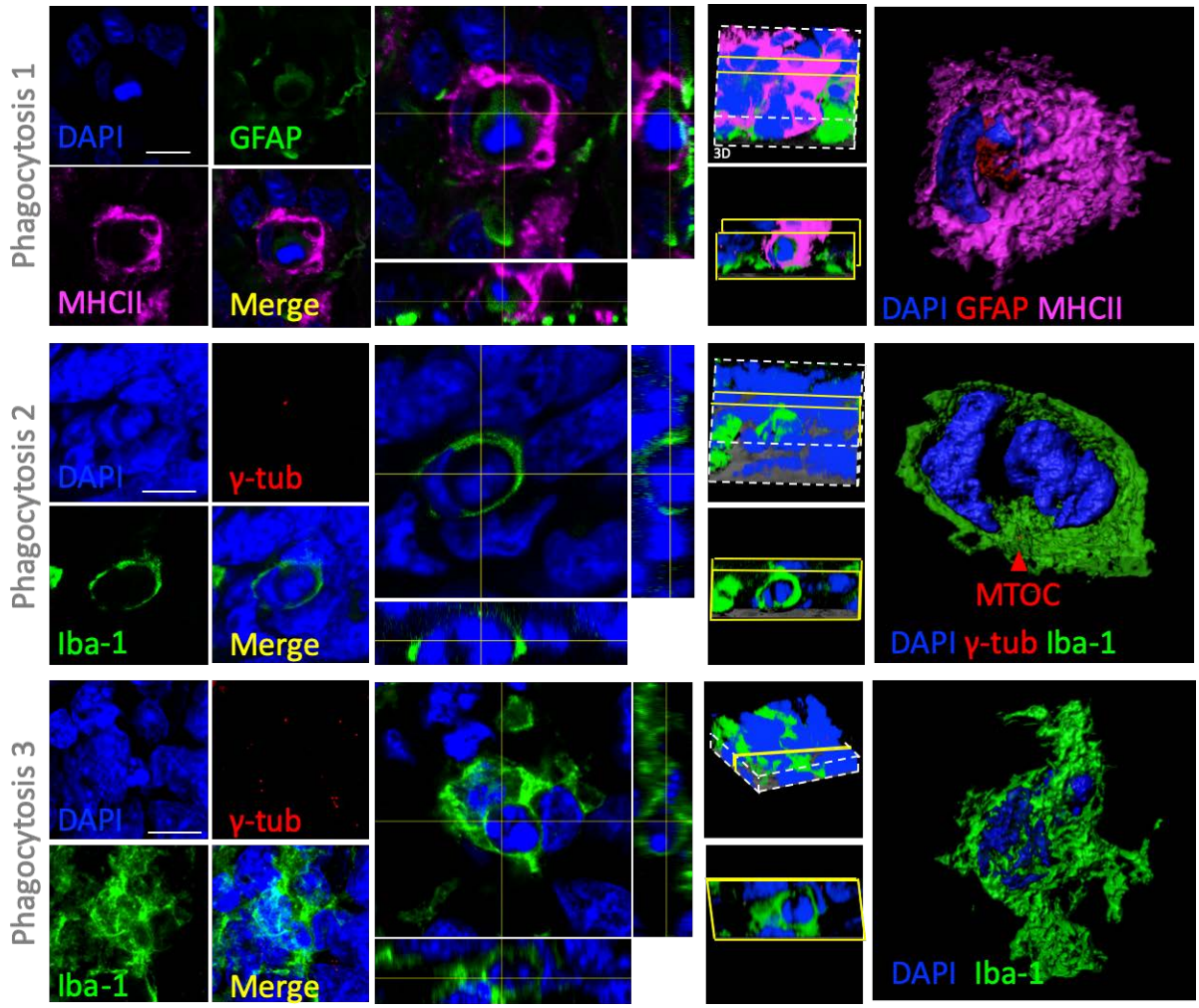

Figure 14. GAMMs are able to effectively phagocytose in human GBM. Three different examples showing high resolution events of phagocytosis (in case of phagocytosis 1: DAPI, in blue, GFAP in green, MHCII in magenta and the merged imaged; in case of phagocytoses 2 and 3: DAPI in blue, γ-tubulin in red, Iba-1 in green and the merged image), the orthogonal views of the Z-stack, and two different 3D reconstructions (the first one with a double clipping plane to better visualize the phagosome and the second one with isosurfaces to isolate the events) with different 3D visualization softwares demonstrate that these myeloid cells are able to engulf cells in GBM, even cells which are still expressing the cytoskeletal protein GFAP, presumably glioma cells. MTOC labelling did not revealed a particular polarizing position.

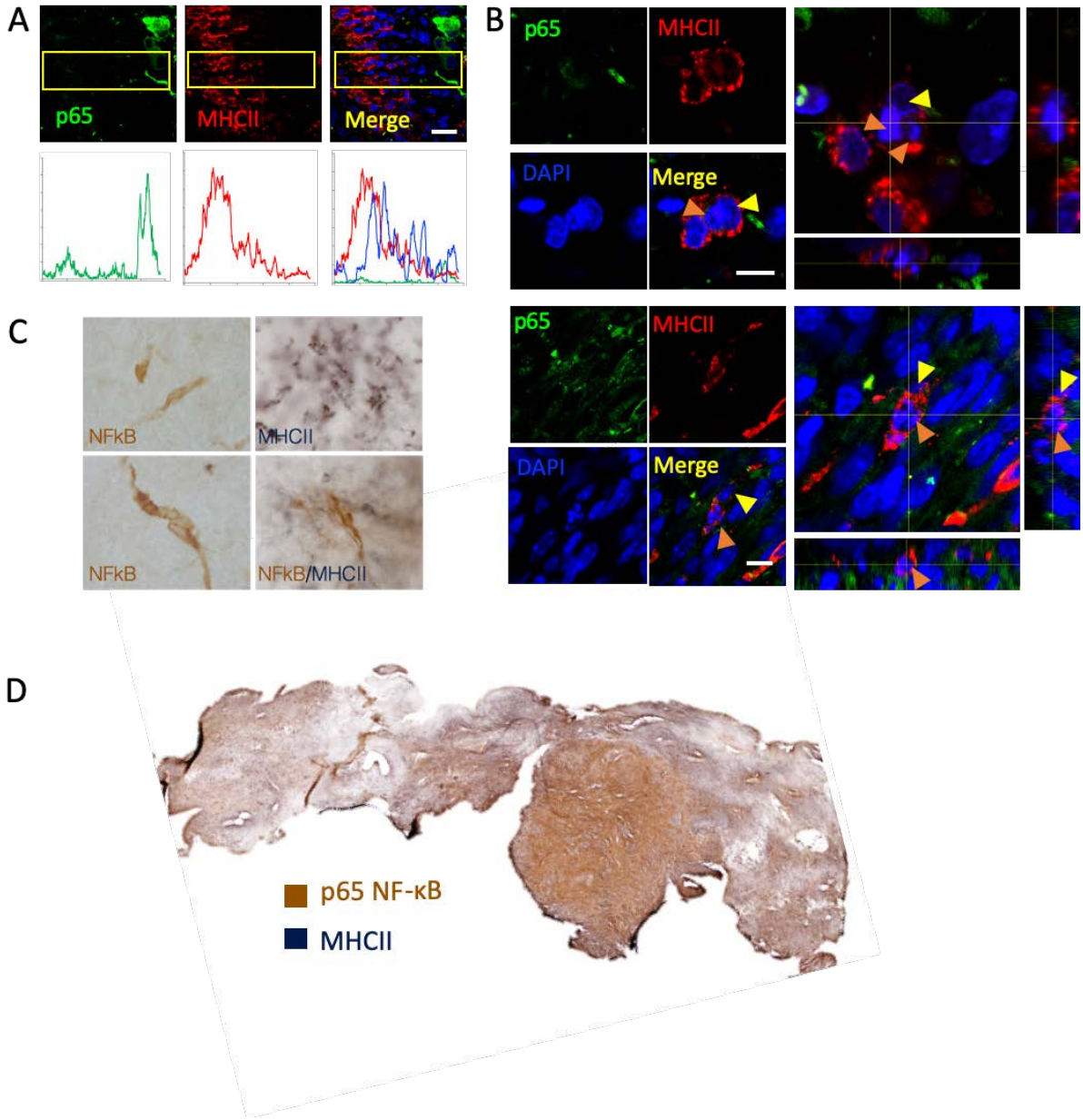

Figure 15. GAMMs do not translocate p65 NF-κB. A. Single slices and fluorescence profile plots show that MHCII+ cells (red) within PPs do not translocate p65 signaling molecule (Green) while gemistocytic cells near the TP do express the signaling molecule. Scalebar=25 um. B. MHCII+ cells digesting pyknotic nuclei show no p65 expression, while neighboring cells are p65+. Scalebars = 10 um on the single slices; orthogonal views displayed at the right side. Orange arrowheads point at pyknotic nuclei while the microglial nuclei are pointed out with yellow arrowheads. C. Close up images of a human GBM slice display NF-κB in brown within cells with tumor-like morphology; while MHCII+ cells in black are rounded. Cells that express MHCII do not show a clear expression or nuclear translocation of NF-κB. Pictures are taken at 100X D. Mosaic of pictures of a human tumor slice stained by immunohistochemistry displaying NF-κB in brown and MHCII in dark blue.

NF-κB is translocated upon classical microglial activation

As p65 seemed not to be translocated even in phagocytic GAMMs, we decided to further study p65 NF-κB translocation in cell cultures under a classic pro-inflammatory stimulus. For this means, we made use of BV-2 microglial cells, and in a very straightforward experiment we targeted p65 translocation through the canonical pro-inflammatory insult with the molecule LPS; while Ibu was used as anti-inflammatory control (**Figure 16**). LPS treatment induced a clear NF-κB expression and nuclear translocation, corroborating the classical signaling of the pro-inflammatory response that it is well known to accelerate the phagocytic responses. While Ibu alone caused no changes in the amount of material colocalized if compared with control, the differences were statistically increased ($p<0.05$) if compared with LPS treatment. Finally, the combinatory treatment of LPS and Ibu significantly increased the material of p65 NF-κB and DAPI co-localized if compared with the control and the treatment with Ibu alone (**Figure 16 C)**. Regarding the cells' surface area, the combination of LPS and Ibu increased it if compared to every other treatment (**Figure 16 D**), measured from the staining of the key cytoskeletal protein α-tubulin; but as depicted in the Venn diagrams, this treatment also increased the surface area occupied by the nuclei and the p65 signaling molecule. This way, even though ibu alone did not provoke p65 NF-κB translocation, the combination of ibu and LPS induced an apparently more severe response than the treatment with LPS alone. However, it remains unclear if the former reflects any biological implication in this scenario.

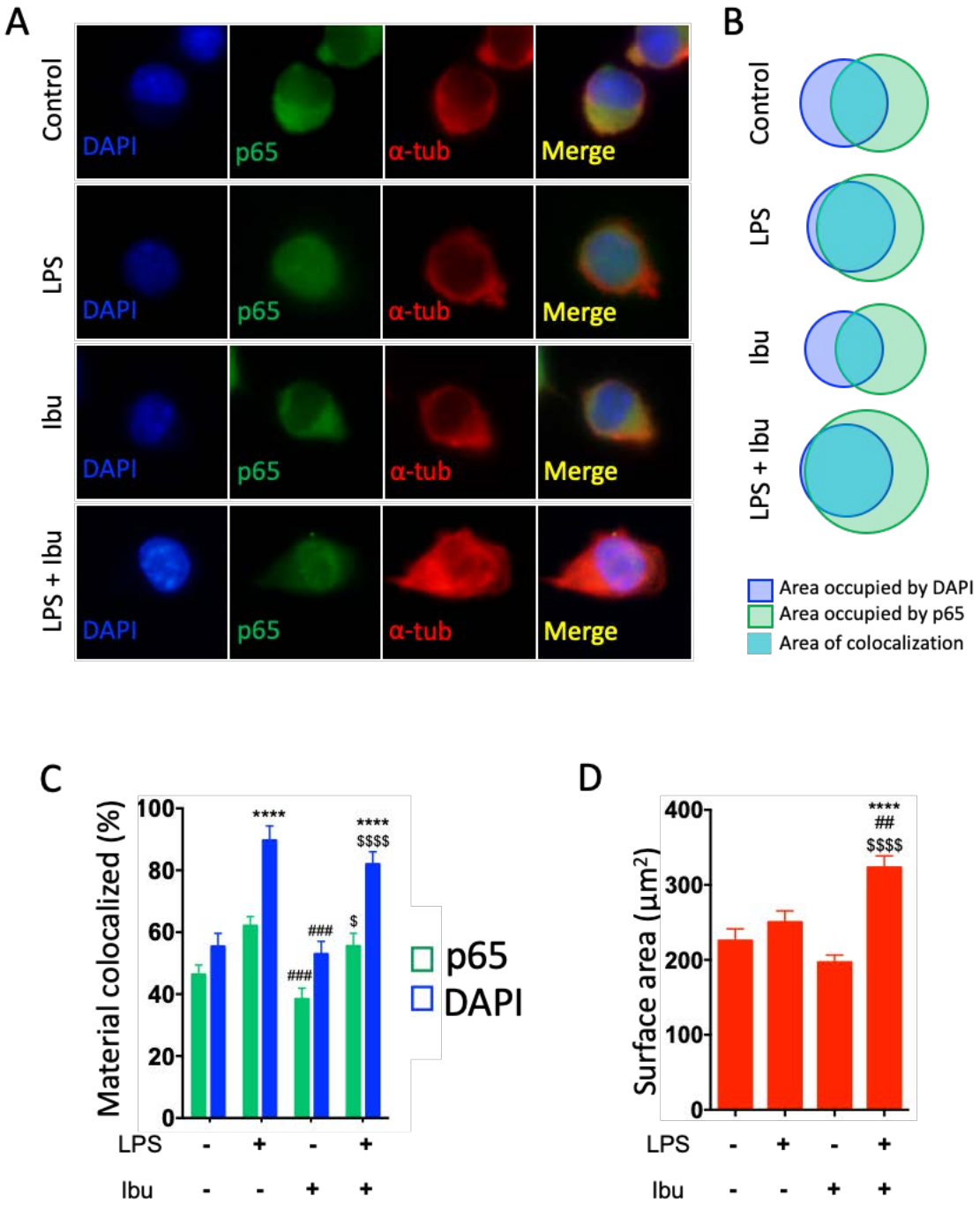

Figure 16. LPS stimulation translocates p65 NF-κB in microglial cells. A. Immunofluorescence images of microglial cells under the different treatments show that p65 is translocated after LPS stimulation even if the anti-inflammatory molecule ibuprofen is added. B. Proportional symmetrical Venn diagrams represent of the amount of DAPI (blue) and p65 (green) colocalizing (cyan intersection). C. Bar chart shows LPS increases the percentage of DAPI colocalizing with p65 NF-κB, when added alone as well as with ibuprofen (* vs control; # vs. LPS; $ vs Ibu; one symbol indicates $p<0.05$; three symbols $p<0.005$ and four symbols $p<0.001$) D. Cells co-treated with LPS and ibuprofen increase their surface area, calculated by measuring the area occupied by α-tubulin (**** $p<0.001$ vs control; ## $p<0.01$ vs LPS; $$$$ $p<0.001$ vs Ibu).

Primary microglia eliminate C6 glioma cells upon priming through p65 NF-κB pathway

Because cell lines show a number of limitations, we started a new series of experiments with primary cultures. Therefore, in furtherance for studying the role of p65 in phagocytosis and its promotion in glial-derived environments, we set up an in vitro model in which primary microglia was extracted from neonatal rats, activated; and presented to C6 glioma cells. Activation was performed by means of a single co-stimulatory dose of LPS and IFN -γ, and presented to either C6 glioma cells or healthy secondary astrocytes as a theoretically negative control for phagocytosis (**Figure 17 A**). Nitrite secretion by microglia into the cells' supernatant and thus activation was confirmed by means of the Griess assay (**Figure 17 B**). Moreover, when staining the cells for p65 NF-κB we saw that upon LPS/IFN-γ co-stimulation the molecule was indeed translocated to the microglial nucleus (**Figure 17 D**). Furthermore, interestingly, activation of microglia prior to the co-culture with healthy astrocytes might positively affect astrocytes, as they were more abundant when microglia had been pre-treated with either LPS or IFN alone (**Figure 17 C**). Contrasting with the co-culture with secondary astrocytes, the co-stimulus did provoke a decrease of C6 cell percentage when co-cultured with activated microglia (**Figure 17 C**), corroborating the elimination of tumor cells in pro-inflammatory conditions. Moreover, when examining the co-culture in which microglial cells were co-stimulated and presented to C6 cells, we observed $GFAP^+$ material inside microglial cells in large $OX42^-$ spaces, accompanied by the orientation of the microglial nucleus towards that space, suggestive of a phagosome (**Figure 17 E**). Thus, these results indicate that activation of the p65 NF-κB pathway induces a decrease of C6 cells by microglial phagocytosis. Noteworthy, our images revealed p65 NF-κB translocation to the nuclei of microglial cells upon activation, especially during the initiation of the contact and during the formation of the phagocytic synapse, before the actual phagocytosis was taking place (**Figure 18 A, B**). However, at this final moment, during digestion, p65 NF-κB was not observed translocated to the nucleus (**Figure 18 C**). These observations suggest that activated nitrite-synthetizing microglia, through the translocation of p65 NF-κB, are able to increase their phagocytic potential to eliminate C6 glioma cells, but probably p65 translocation is no longer required in the final stages of the phagocytic process.

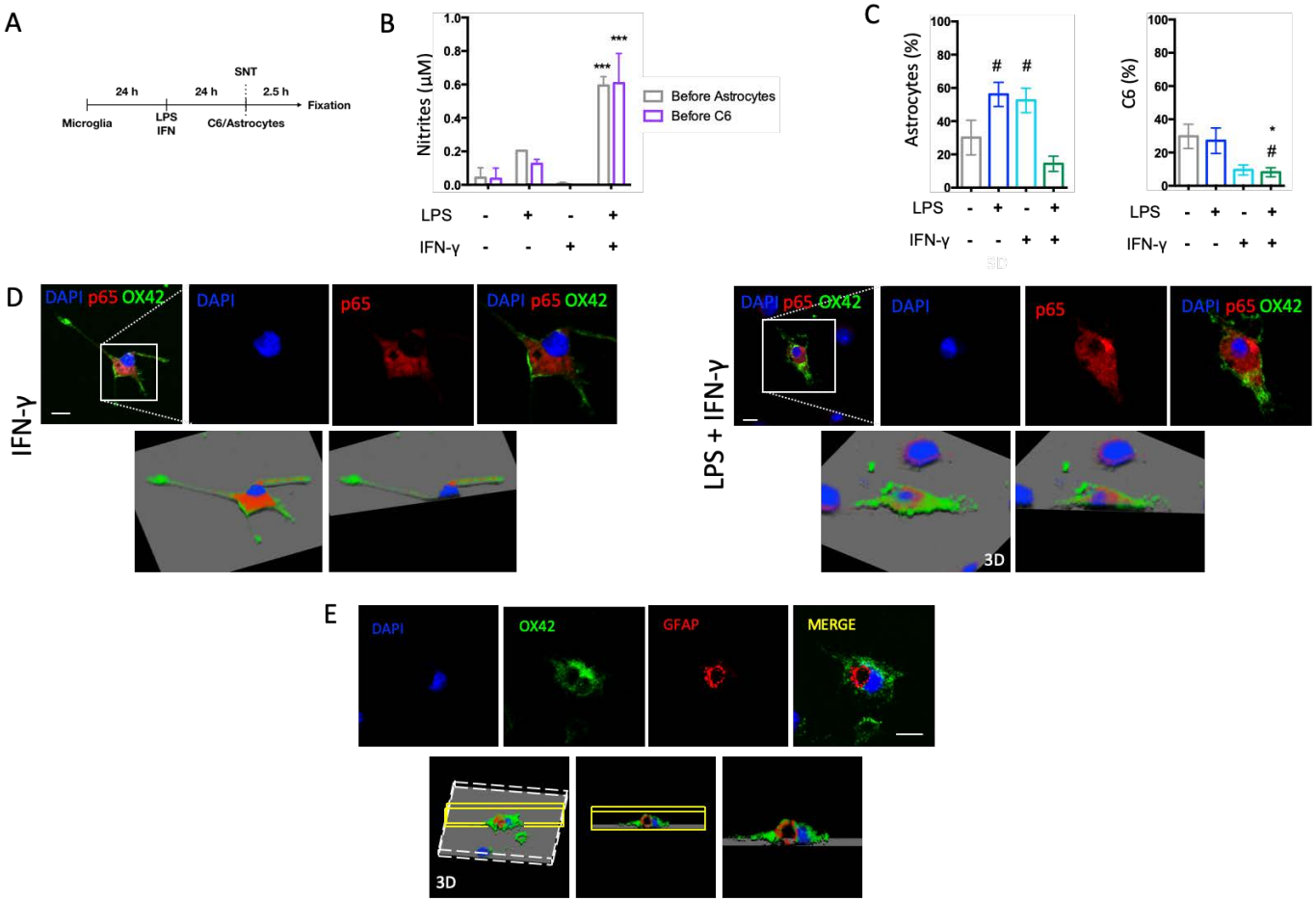

Figure 17. Activated primary microglia decrease C6 cell percentage. A. Schematic showing the experimental design in which microglia are activated by a co-stimulatory dose of LPS and IFN-γ and then co-cultured with either C6 glioma cells or with secondary astrocytes before fixation at 2.5 h. Supernatant (SNT) was extracted before adding the C6/astrocytes with new medium, in order to use it for the Griess test (B). B. Griess test confirms the activation of microglia upon LPS and IFN-γ stimulation, as nitrites detected are significantly higher in this condition. *** $p<0.005$ vs. all conditions within the same co-culture. C. Quantification of GFAP+ cells shown as increase in the percentage of astrocytes when microglia is pre-treated with LPS or IFN alone (# $p<0.05$ vs. LPS + IFN-γ) while the number of C6 cells is significantly decreased when microglia is co-treated with LPS and IFN-γ before co-culture (*$p<0.05$ vs. control; # $p<0.05$ vs. LPS). D. Staining for p65-NF-κB further confirms activation of microglia upon co-treatment with LPS and IFN- γ. Maximum projection of all the channels, a zoom in of a single slice showing the nucleus (blue) and p65 (red) and the merged image with OX42 (green), 3D rendering and 3D rendering with clipping plane are shown. E. Maximum projection of a 10 um-confocal stack of an OX42+ cell co-treated with LPS and IFN with GFAP material inside an OX42- space, with its 3D reconstruction, along with the same reconstruction with a double clipping plane (yellow) and the zoom in to better visualize the GFAP inside the putative phagosome. Scale bars =10 um.

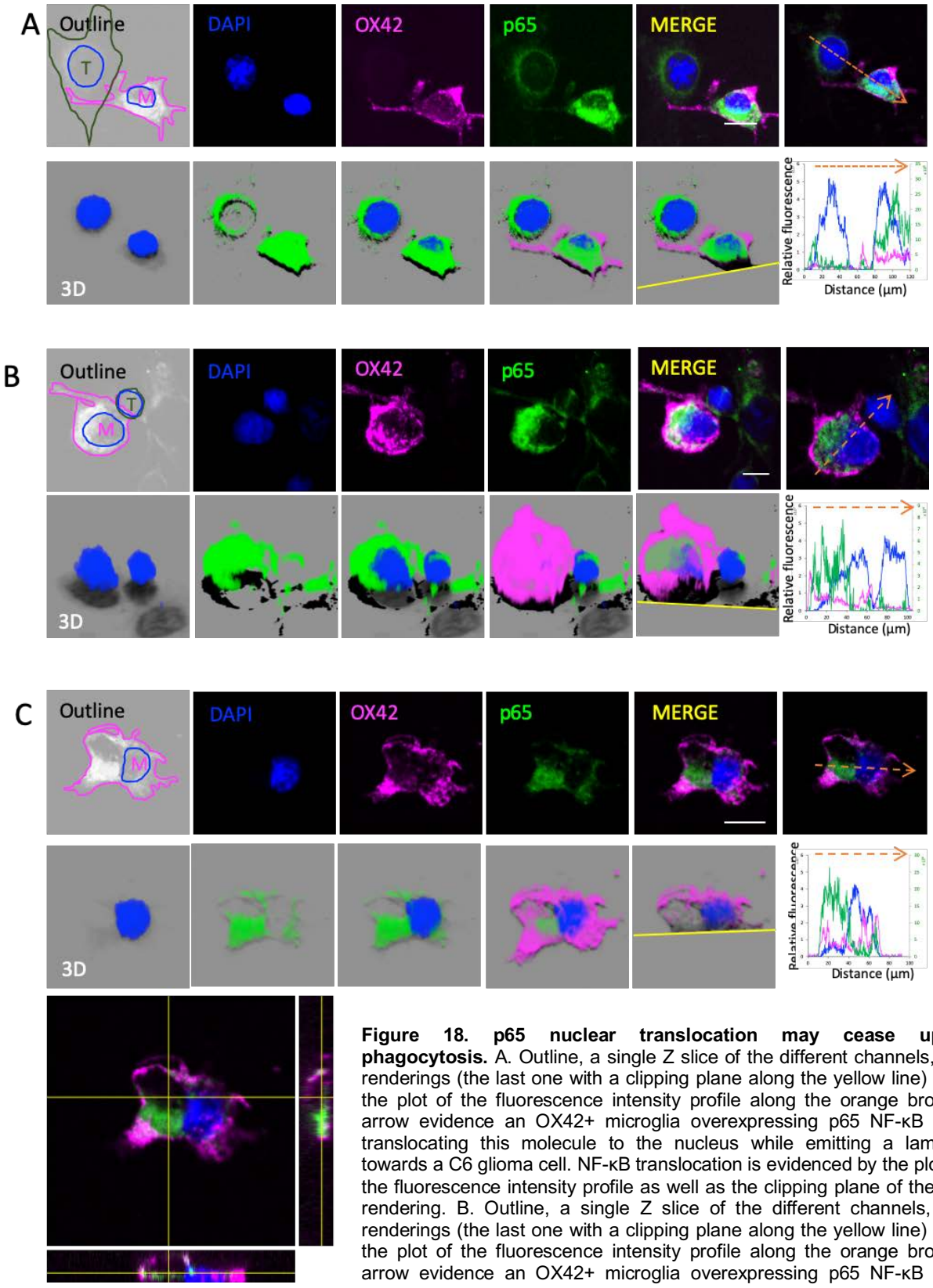

Figure 18. p65 nuclear translocation may cease upon phagocytosis. A. Outline, a single Z slice of the different channels, 3D renderings (the last one with a clipping plane along the yellow line) and the plot of the fluorescence intensity profile along the orange broken arrow evidence an OX42+ microglia overexpressing p65 NF-κB and translocating this molecule to the nucleus while emitting a lamella towards a C6 glioma cell. NF-κB translocation is evidenced by the plot of the fluorescence intensity profile as well as the clipping plane of the 3D rendering. B. Outline, a single Z slice of the different channels, 3D renderings (the last one with a clipping plane along the yellow line) and the plot of the fluorescence intensity profile along the orange broken arrow evidence an OX42+ microglia overexpressing p65 NF-κB and partially translocating this molecule to the nucleus while forming a phagocytic cup upon a C6 glioma cell. Partial NF-κB translocation is evidenced by the plot of the fluorescence intensity profile as well as the clipping plane of the 3D rendering. C. Single slices of confocal images of a microglial cell with a putative phagosome, as well as the orthogonal views of the stack, show that while there is this $OX42^-$/p65 $NF\text{-}\kappa B^-$/$DAPI^-$ space, p65 NF-κB is not greatly translocated to the cell nucleus. 3D rendering and rotation are shown to better visualize the phagosome, as well as a more intense rendering with a clipping plane displaying the $OX42^-$/p65 $NF\text{-}\kappa B^-$/$DAPI^-$ space. Scale bars =10 µm.

Primary glia priming is order dependent and does not increase phagocytosis.

Given that secondary astrocytes respond to the activation of primary microglia, we designed an experiment in which the coculture was done between primary mixed glia and C6 cells. Prior to this presentation, glia was stimulated with classical pro-inflammatory compounds to boost phagocytosis, namely LPS and IFN-γ; but also with the canonical anti-inflammatory cytokine IL-4. Again, glial activation was indirectly confirmed by means of the Griess test, by measuring the amounts of nitrites in the supernatants in which cells grow; and also by the change in $OX42^+$ cell surface area (**Figure 19**). Upon activation, nitrite production was increased compared to the control, independently if the pro-inflammatory stimuli were received before or after the anti-inflammatory compound, IL-4. However, when applying the proinflammatory stimuli in the first place and the anti-inflammatory as the secondary stimulus (**Figure 19 C, D**), the nitrite production reached 50% when compared with the stimuli being placed in the inverse order (**Figure 19 A, B**), suggesting that IL-4 only partially halted glial activation. When measuring the area of $OX42^+$ cells, the effect of decreased OX42 area was more dramatic when applying the anti-inflammatory stimulus as the secondary agent.

We quantified the amount of phagocytoses, and the number of C6 glioma cells (**Figure 19 B, D**). These results suggest that the order of the stimuli does not affect the outcome in this scenario. Therefore in these experiments of mixed glial cultures, although cells respond to the stimuli (as measured by Griess assay and OX42 expression), microglia do not do so by increasing the phagocytosis of tumor cells, as in none of the cases the amount of phagocytoses increased and no statistically significant reduction in the number of C6 cells was seen. These results nourish the idea of the importance of the microenvironment for glioma cells clearance by GAMMs, since the presence of non-myeloid glia may alter the final response.

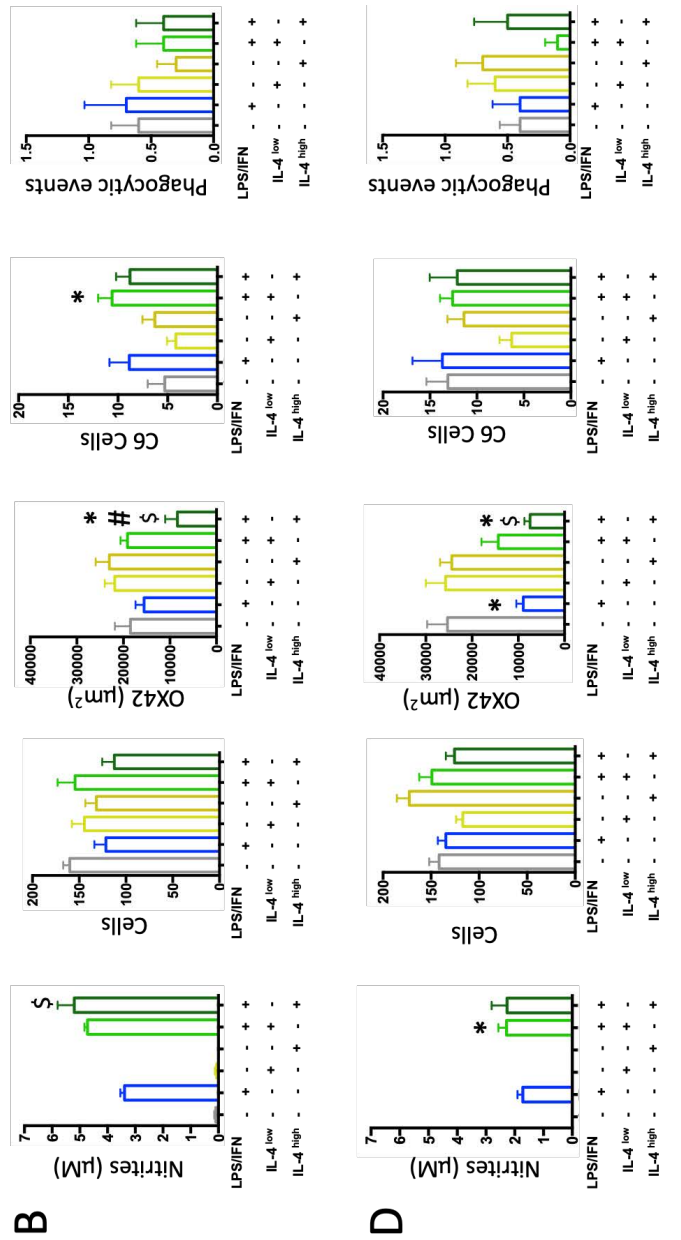

Figure 19. Primary microglia in mixed cultures do not effectively eliminate C6 glioma cells. A. Experimental design of the primary mixed culture (PMG) receiving the anti-inflammatory stimulus (IL-4) 24h before the proinflammatory insult (LPS/IFN), to then extract the supernatant (SNT) to prove activation and be co-cultured with C6 cells for 3h and then fixed. B. Quantifications of nitrite secretion, total number of cells, area of OX42, number of C6 cells and phagocytoses per image, suggesting that astrocytes in the culture are buffering the phagocytic response of microglial cells towards C6 glioma cells. C. Experimental design of the primary mixed culture (PMG) receiving the pro-inflammatory stimuli (LPS/IFN) 24h before the anti-inflammatory one (IL-4 at either 20 or 100 µM), to then extract the supernatant (SNT) to prove activation and be co-cultured with C6 cells for 3h and then fixed. D. Quantifications of nitrite secretion, total number of cells per image, area of OX42 per image, number of C6 cells, and number of phagocytoses per image where microglia respond to the pro-inflammatory stimulus essentially by decreasing their surface area, but not by phagocytosing C6 cells. P<0.05 * compared vs untreated; # compared with only LPS/IFN-γ treatment; $ compared with LPS/IFN-γ IL-4 ^{high}.

BV-2 microglial cells actively search for target cells

Since BV-2 microglial cells are a highly phagocytic cell line, we set up new experiments to analyze the interaction of microglia and GL261 glioma cells. We had the technical drawback of finding a reliable antibody to distinguish BV-2 cells from GL261 cells. Thus, in a pursue to study the phagocytic interaction and the synaptic interface, we stained the cell lines with two different CellMask™ Plasma Membrane Stains and also attempted at the light-momentum method. By time-lapse analysis using brightfield microscopy we can observe BV-2 microglial cells under standard conditions, confirming that they are always scanning their microenvironment frequently emitting long filaments. Although some filaments seem more motile than others, they can easily move and contact other cells (**Figure 20 A, B**). When co-cultured with GL261 glioma cells, BV-2 cells are able to contact them (**Figure 20 C**), and through the binding of small filaments, they firmly attach and get closer in a short period of time (**Figure 20 D**). However, BV-2 cells are not only interacting with apparently healthy GL261 cells, but also to dying cells, as ascertained by the use of the NucGreen™ Dead 488 ReadyProbes™ Reagent. This technique allowed us to visualize BV-2 cells contacting and forming a presumed phagocytic cups over non-myeloid dying cells (**Figure 20 E**).

BV-2 cells phagocytose dying GL261 cells

For the analysis of this co-culture, we used the green channel to see if the cells being phagocytosed were dead, by means of the NucGreen™ Dead 488 ReadyProbes™ Reagent in combination with CellMask™ Plasma Membrane Stains. In this set up, BV-2 microglial cells, once they contact their target, they approach and polarize towards it. (**Figure 21 A**). Here, the small filaments previously shown with higher magnification (**Figure 20 D)** are not visible, presumably due to the lower magnification and the lipidic nature of the staining, as these structures are rich in actin (81). However, they are probably present at least up to the stage of the flat interface (**Figure 21 B**) as higher magnification images showed (**Figure 20 D**). Images of microglia-target interactions

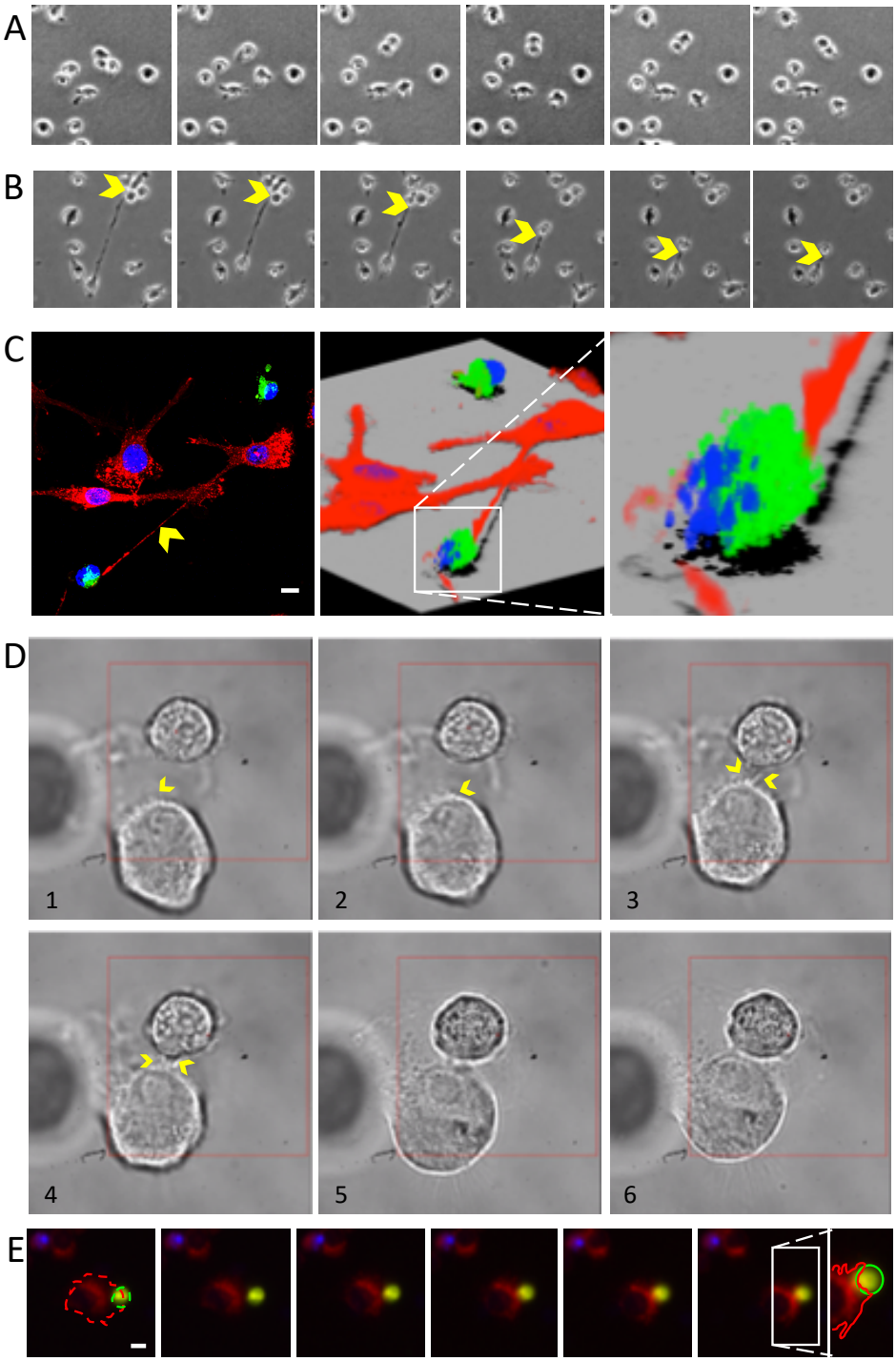

Figure 20. Target search and contact establishment between BV-2 and GL261 cells. A. Time-lapse imaging of a BV-2 cell culture showing that these cells constantly scan their microenvironment and move by means of short filopodia. Yellow arrowheads pointing at microglial cells at this state . Time between frames is 10 minutes. B. BV-2 cell culture time lapse also shows that these cells sometimes quickly launch long filopodia, which they can use to move long distances in a short period of time. Yellow arrowhead pointing at the cell which travels the greatest distance in the shown frames. Frames are 10 minutes apart from each other. C. Maximum projection of a confocal image shows a BV-2 cell (red) emitting a filopodium (yellow arrowhead) of around 100 um towards a GL261 cell (green). Nuclei are counterstained in blue with NucBlue live Readyprobes Reagent. Scale bar =10 um. 3D rendering corroborates the contact between the cells. D. The light-momentum method allowed us to place a GL261 cell (outlined in green) near a BV-2 cell (outlined in red), and record the interaction. In this sequence of images which lasts 6:13 minutes it can be seen how the BV-2 cell approaches, polarizes its cytoplasm and lamellipodium towards the target cell and establishes a close apposition by attaching to it through several small filaments (yellow arrowheads). E. Sequence of fluorescence imaging shows a BV-2 cell (red, outlined) approaching a dead nucleus (green, outlined) and establishing a putative phagocytic cup around it. In this case the images are taken every 5 minutes. Scale bar= 10 um.

frequently revealed a lamella being positioned under dying GL261 suggesting a preceding step of the engulfing process. We also observed flat interface interactions resembling immunological synaptic interactions as well as telling images of phagocytic cup formation, which is defined as a semicircular engulfment of dying cells (**Figure 21 C**). These sets of images suggest the potential sequence that may happen during elimination of target cells by BV-2 microglia, being; the initial approximation, phagocytic synapse establishment, and phagocytosis of the target (**Figure 21**).

Engulfment then starts by the formation of the phagocytic cup, where BV-2 cells embrace and project a lamella under the dying GL261 cell (**Figure 21 C**). Interestingly, although we have seen dead nuclei being digested inside the BV-2 cells (**Figure 21 D**), hardly no events of an undergoing engulfment after the phagocytic cup have been spotted, what suggests that this step may occur rapidly.

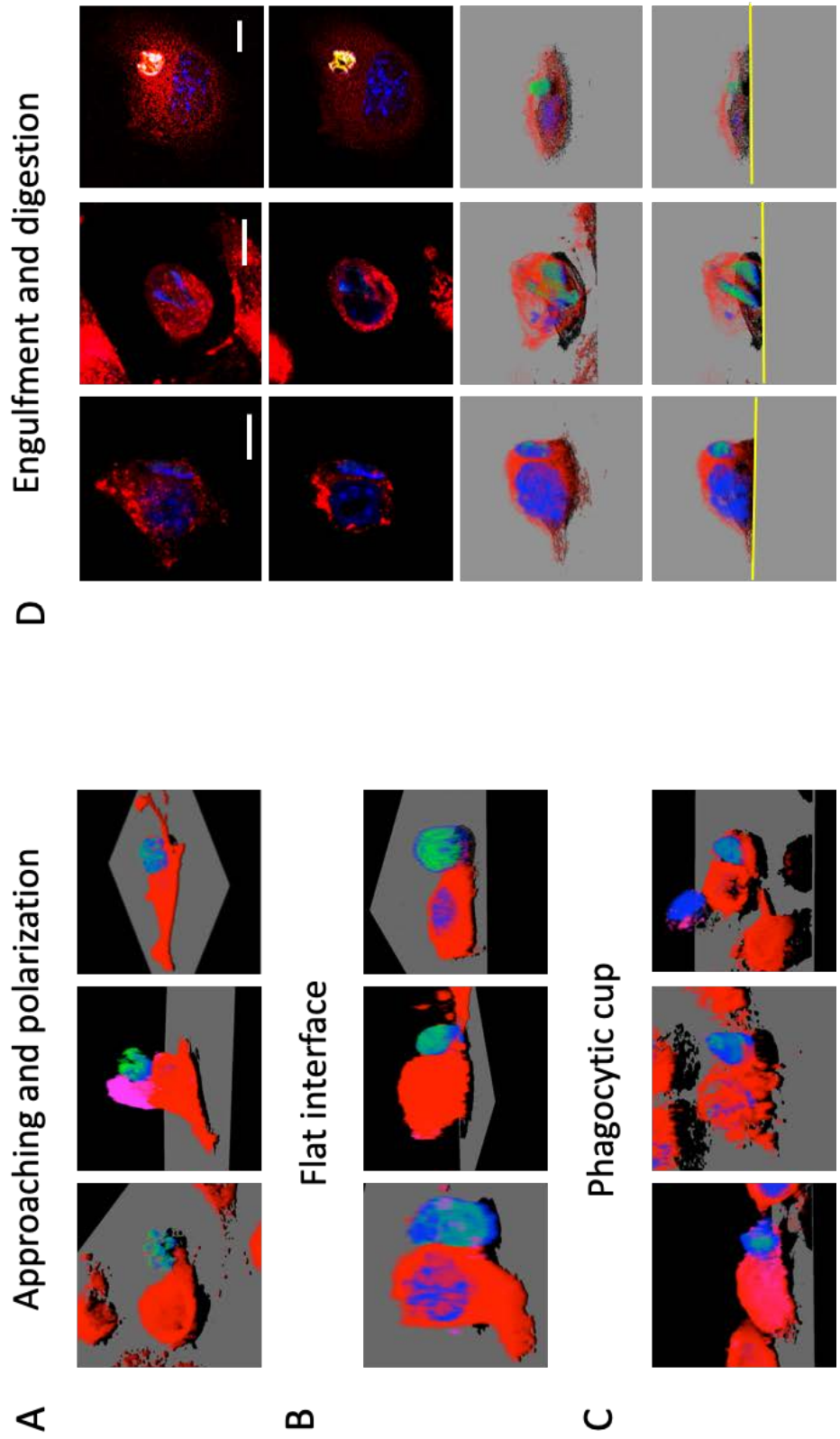

Figure 21. BV-2 microglial cells phagocytose dying GL261 cells. A. BV-2 microglial cells (red) recognize dying targets (GL261 cells in magenta expressing the cell death green probe in their nuclei). Oriented filopodia and polarizing membrane to the target can be appreciated. B. In the events where the target is at all means attainable, the phagocytic synapse is recognizable by the flat interface established between interacting cells. C. BV-2 microglial cells potentially initiate the engulfment through the formation of a phagocytic cup, while also attached to the substrate. D. In events when the engulfment is seemingly completed and the target is surrounded by the microglial cell, we can see pyknotic nuclei inside an apparent phagosome. A, B, and C through 3D renderings show three different gliapses each, while D also displays three events, but in this case with maximum projections, a single Z slice with the microglial nucleus and the dying cell being phagocytosed, a 3D rendering of the image, and this rendering with a clipping plane showing the phagocytosed nucleus completely surrounded by microglial membranes.

BV-2 microglial cells phagoptose living GL261 cells

Importantly, this co-culture set up allows the differentiation of live and dying cells and therefore primary phagocytosis or phagoptosis can be explored. We found the NucGreen probe sometimes absent from the target nucleus, while the cell membrane remained unscathed, proving the target cell was still alive (**Figure 22**). This way, we can see BV-2 cells in contact and polarized towards GL261 cells (**Figure 22 A**), establishing flat interfaces (**Figure 22 B**) and creating phagocytic cups (**Figure 22 C**). At these two last stages, microglial cells are completely polarized towards the target but they are also anchored to the substrate through short filaments (**Figure 22 C**). As aforementioned, in some cases we found nuclei being digested that did not express the cell-death marker NucGreen, suggesting that GL261 cells while being engulfed may die in the process, but they did not have the possibility to include the NucGreen probe into their nuclei as being included in a membrane form (or protected) phagosome. This set of images suggests that the process of phagocytosis may involve these steps although not always involving the target cell dying or being dead.

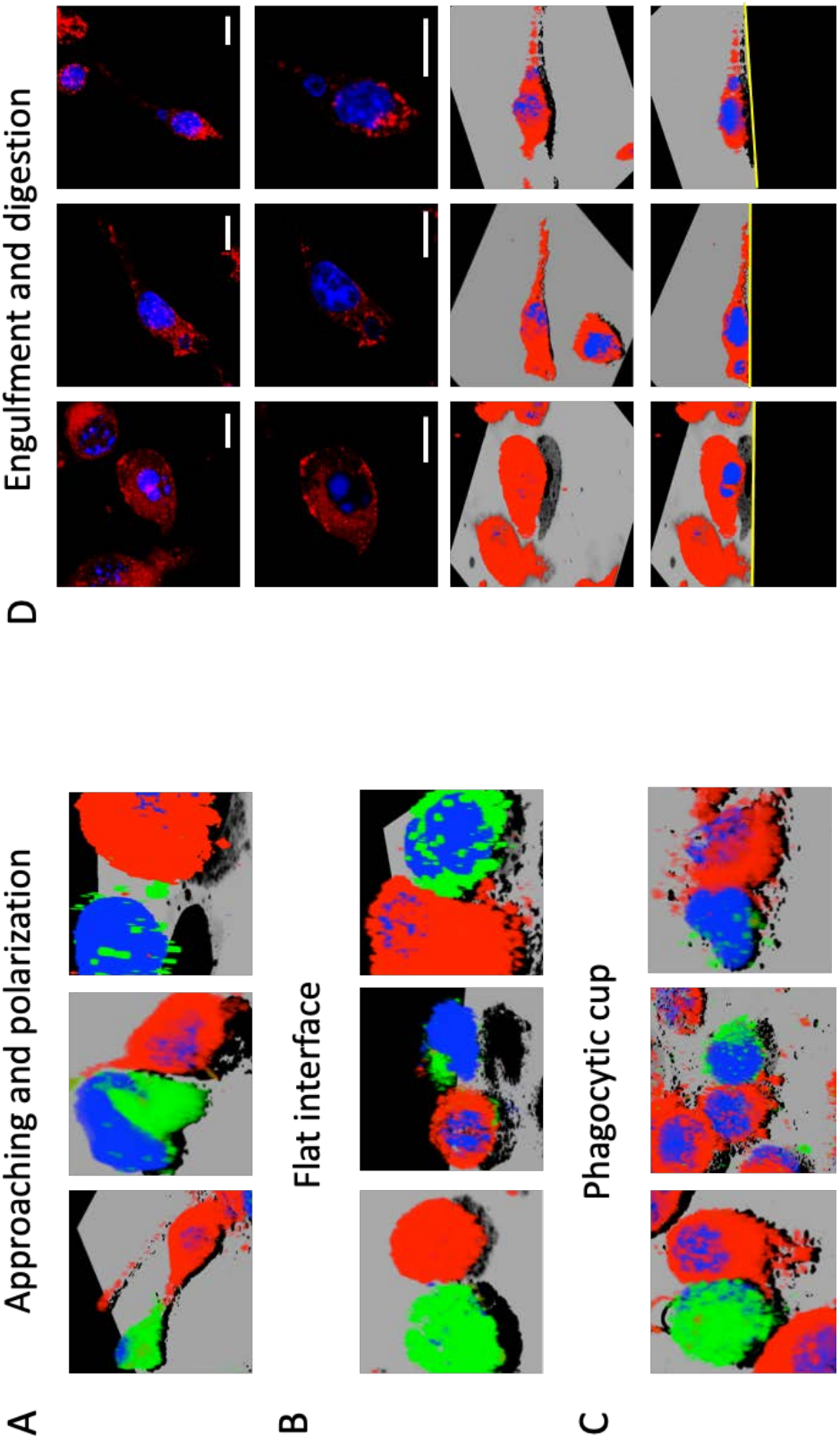

Figure 22. BV-2 microglial cells phagocytose living GL261 cells. A. BV-2 microglial cells (red) recognize their target (GL261 cells in green). In this presumed initial interactions, their filopodia and membrane appear to be polarized to the target. B. Once the target cell has been reached, the synapse is recognizable by the interface, often flat, established between the interacting cells. C. BV-2 microglial cells form phagocytic cup surrounding living glioma cells. This cup appear to be very rich in lipids as evidenced by the red staining. D. In events of completed engulfment the target is completely surrounded by the microglial cell, we can see pyknotic nuclei inside an apparent phagosome. A, B, and C through 3D renderings show three different gliapses each, while D also displays three events, but in this case with maximum projections, a single Z slice with the microglial nucleus and the cell being phagocytosed, a 3D rendering of the image, and this rendering with a clipping plane (yellow line) showing the phagocytosed nucleus completely surrounded by the microglial membranes.

Visualization of molecular clusters at the microglial phagocytic interface

Because CD11b is a critical integrin in the adhesion of microglia, and CD16/32 is a key receptor in the stimulation of phagocytosis in microglia and macrophages, we wanted to analyze whether a specific segregation or clustering occur at the interface with glioma cells. This way, by using immune-cytofluorescence, and 3D reconstructions we analyzed the distribution of the integrin CD11b and Fc-γRs CD16/32 within the BV-2 microglial cells in the potential stages of phagocytosis described before. In cells with motile stage, or potentially approaching towards a target cell, CD11b (**Figure 23**) and CD16/32 (**Figure 24**) appear to be highly expressed in the rear of the cell. The accumulation of these molecules could be confirmed by the visualization of the green channel in rainbow spectrum colors, where the high fluorescence is displayed in white and red colors. Moreover, when plotting the fluorescence profile along a line longitudinally crossing the entire microglial cell body, we observe the highest fluorescence peak at the trailing part of the cell. This result suggests that both, CD11b and CD16/32 may not be required for the early recognition of the target.

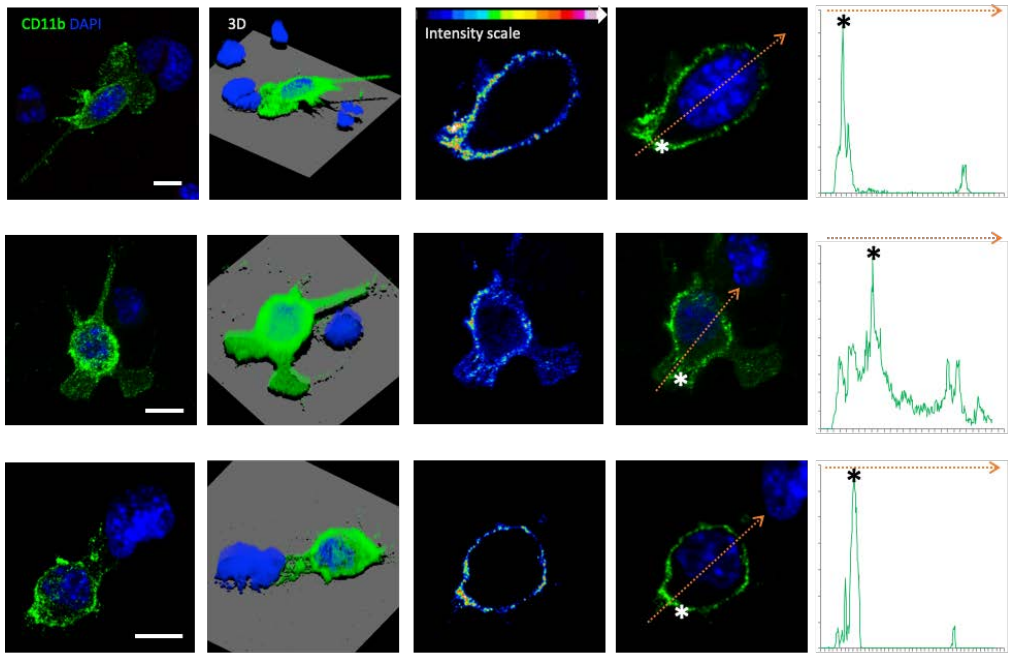

Figure 23. CD11b distribution within BV-2 cells when reaching a target cell. Maximum projection (Scale bar = 10 um), 3D reconstruction and zoomed in single Z slice in rainbow spectrum and in green and blue are shown (from left to right, respectively) to visualize the distribution of the integrin CD11b in three different BV-2 cells approaching their corresponding target cell. A profile plot of the relative fluorescence of the protein along the orange arrow is displayed, where we can see the maximum peak at the rear of the cell (*), confirming the high fluorescence evidenced by the rainbow spectrum in red and white in the same place.

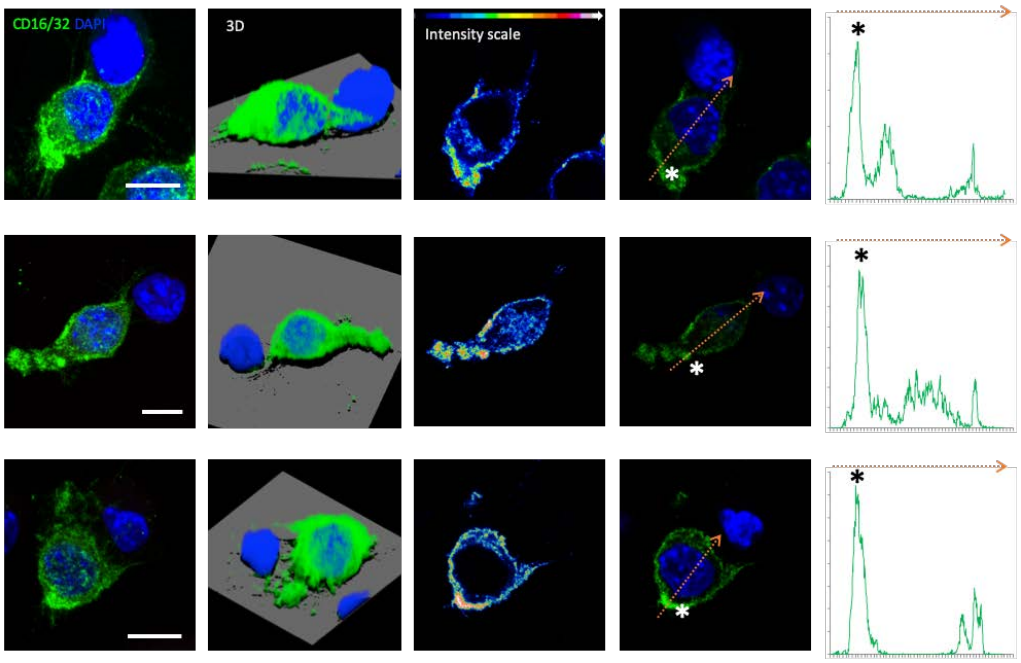

Figure 24. CD16/32 distribution within BV-2 cells when reaching a target cell. Maximum projection, 3D reconstruction and a single Z slice in rainbow spectrum and in green are shown (from left to right, respectively) to visualize the distribution of the opsonic receptor CD16/32 in three different BV-2 cells approaching potential target cells. A profile plot of the relative fluorescence of the protein along the orange arrow is displayed, where we can see the maximum peak at the rear of the cell (*), confirming the high fluorescence evidenced by the rainbow spectrum in red and white in the same place. Scale bar= 10 um.

However, when BV-2 cells are visualized in a clear interacting manner with glioma cells, the CD11b integrin and the CD16/32 receptor are distributed and clustered at the interface. In events where a flat interface was formed with the target cell, CD11b **(Figure 25)** and CD16/32 **(Figure 26)** were polarized towards the target and appeared accumulated at the peripheral area of the interaction forming a ring of clusters each, resembling the T cells' pSMAC. This is clearly displayed on the periphery of the contact, while there might also be a central accumulation of the receptors, as seen by fluoresce intensity plots, but the image resolution at z is not sufficient to confirm this in a 3D basis. Further, rainbow spectrum of the green channel in a single central slice allows us to see CD11b and CD16/32 accumulation in the outer part of the contact. Although considering the potential variation of the fluorescence at this resolution, a peak of CD11b seemed to consistently appear at the center of the interface, as revealed by the plot of the green fluorescence along the flat interface in the same slice.

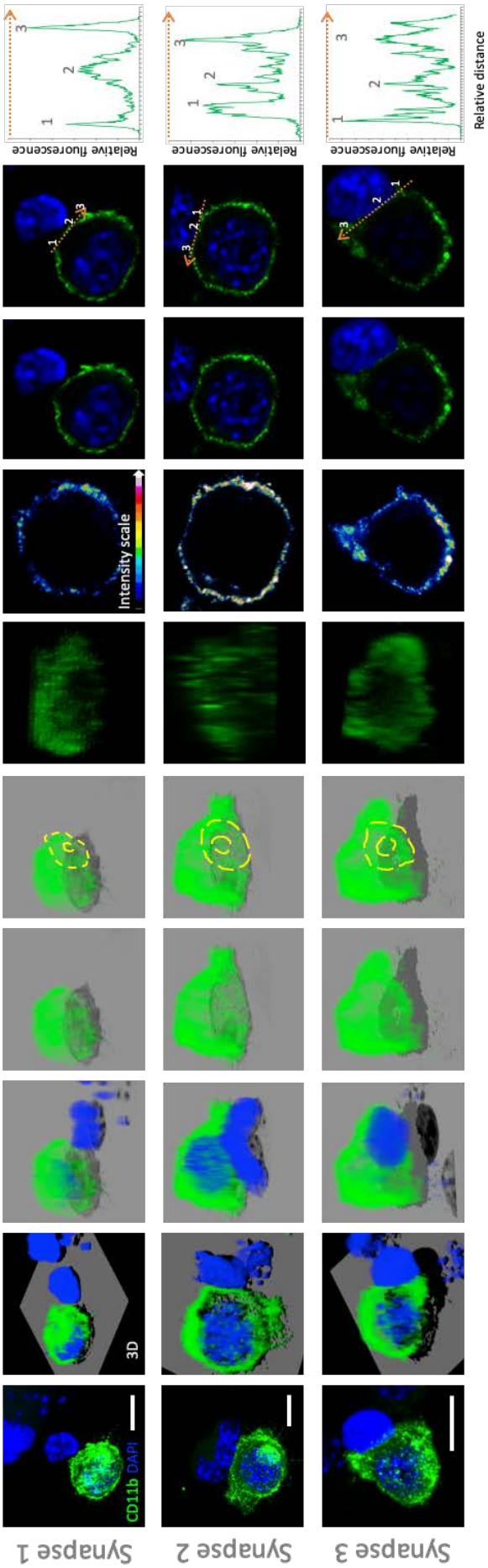

Figure 25. CD11b at interacting interface forms a peripheral ring. Three different phagocytic synapses of BV-2 microglial cells contacting their respective targets are shown with their maximum projections (scale bar=10 um). Moreover, the 3D reconstructions clearly shows a flat interface between the microglial cells and the target glioma cells, and by means of a rotation of this image and a double clipping plane we can observe how the receptor is organized in a ring shape around the interface, while it also seems clustered in the central part of the interacting area. The peripheral ring is very easily seen with the rainbow spectrum, and in the fluorescence profile plot of the green channel (1 and 3), while the central cluster is better confirmed by the fluorescence profile plot along the orange broken arrow (2).

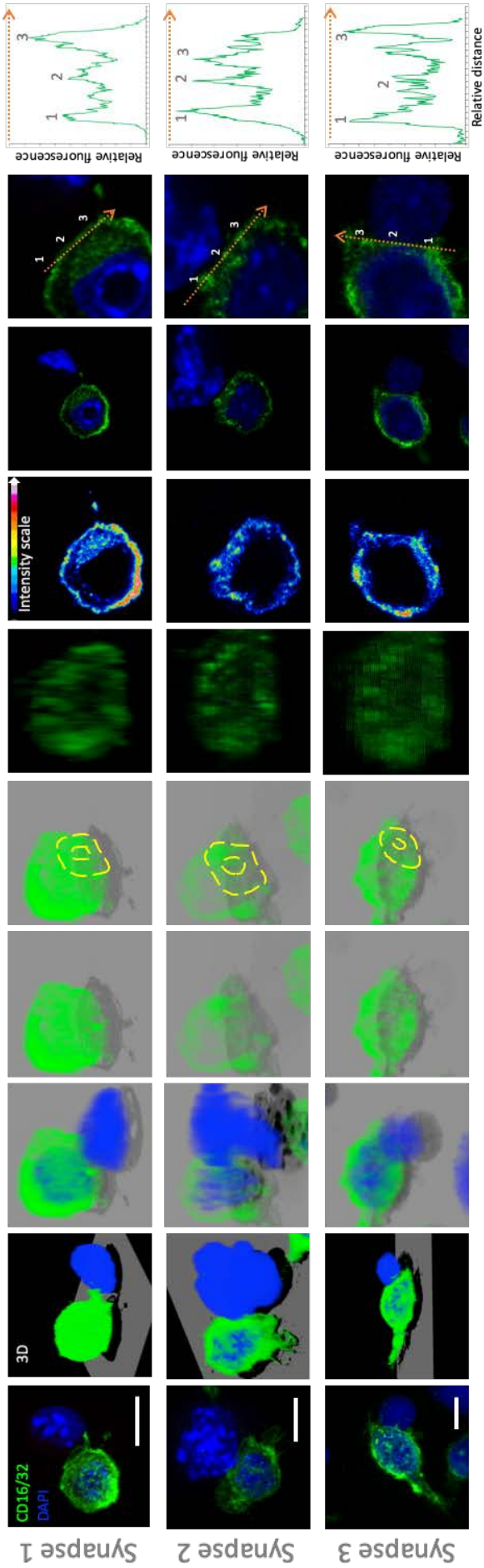

Figure 26. CD16/32 distribution within microglia-glioma interfaces of phagocytic synapses. Three different gliapses are displayed, firstly with the maximum projections of the fluorescence (Scale bar = 10 um), followed by two rotated and zoomed in 3D reconstructions where a flat interface is clearly detectable, first from a lateral view, then from an oblique view. The latter is shown with only the CD16/32 staining, so the target does not interfere with the vision of the flat interface which is also outlined displaying the areas of highest fluorescence within the interface. By rotating and zooming in again; and using two clipping planes we are able to see just the interface, where CD16/32 appears to be distributed in a ring shape. CD16/32 fluorescence in a 16-color spectrum shows within the flat interface, the accumulation of the receptor in the borders of the interface and another variable cluster at the centre. This is further demonstrated by the fluorescence plot of the green channel along the orange broken arrows drawn along the flat interfaces.

In the events where microglial phagocytic cups are formed with glioma cells, a high concentration of the receptors at the periphery of the contacting surface was also displayed (**Figure 27-28**). 3D reconstructions revealed a similar ring-like structure as found in flat interface interactions, as evinced with the double clipping plane in the 3D reconstructions. The appearance of these three dimensional arrangements suggests that the segregation and clustering of CD11b and CD16/32 receptors might be critical in the dynamics involved in the uptake of glioma cells by microglia.

These results suggest that CD11b and CD16/32 are recruited to the interface when a clear interaction between the effector cell and the target cell is formed (as seen in flat interface and phagocytic cup events). Probably, both proteins are not involved in the initial encounter with the target, but on a later stage when the microglial cell has settled to phagocytose. Thus, these receptors may be critical to trigger the effective elimination. Moreover, both studies involving the molecular clustering of CD11b and CD16/32 suggest that microglia entirely rearrange its cellular structure to potentially eliminate target glioma cells by phagocytosis and these events may be specifically targeted to promote phagocytosis in vivo.

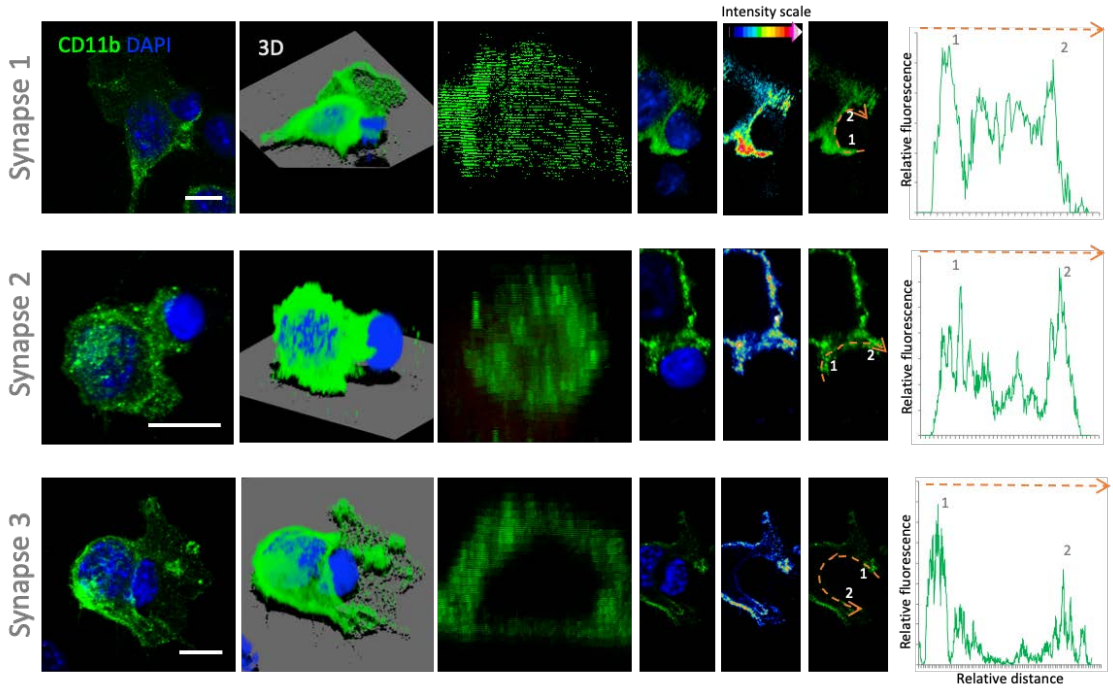

Figure 27. CD11b distribution during the phase of the phagocytic cup. Three different phagocytic synapses during the formation of a phagocytic cup are displayed, and by the maximum projection of the fluorescence, we can see CD11b is highly expressed in the external limits of the cup. The 3D reconstructions better display the arrangement of the cup surrounding the target nucleus, while displaying a concentric structure similar to the one seen in the flat interface events. This is easily seen with the rotation and double clipping plane, evincing the peripheral ring. Rainbow spectrum of the green channel uncovers the high fluorescence in the phagocytic cup especially at the borders, while the fluorescence profile plot of the same channel lets us see the fluorescence peaks of the peripheral ring (1,2) along the orange broken arrow drawn on the phagocytic cup.

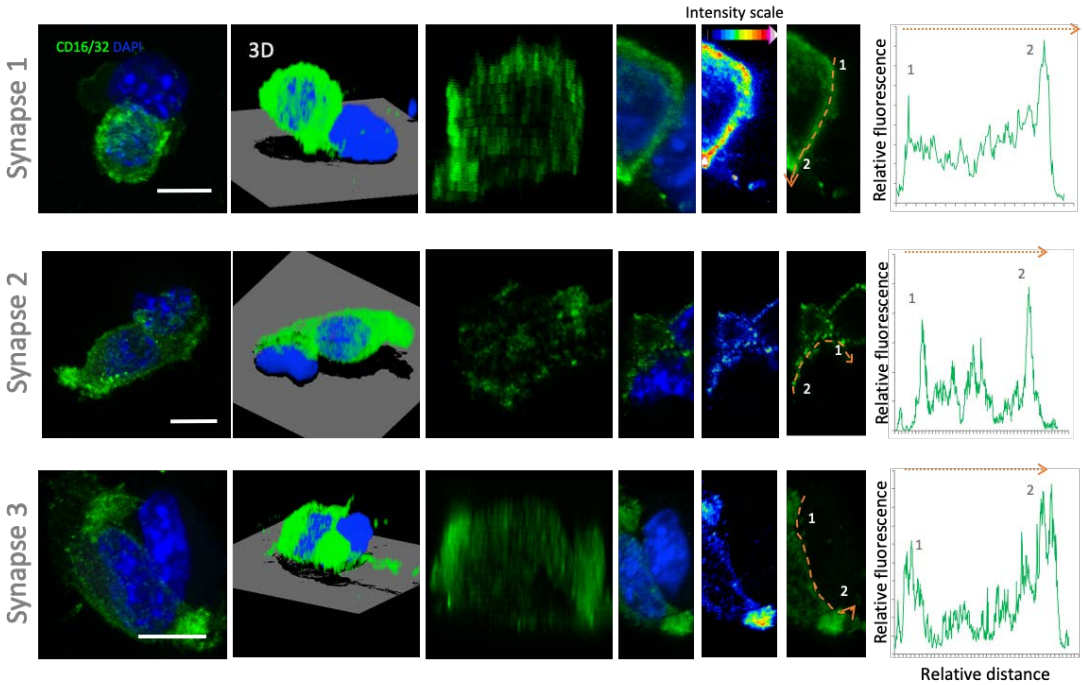

Figure 28. CD16/32 distribution at the phagocytic cup. Three different phagocytic synapses during the formation of the phagocytic cup are displayed, firstly by the maximum projection of the fluorescence, where we can see the target cell being surrounded by the structure of the microglial cup. The 3D reconstruction better displays the cytoplasm surrounding the target nucleus, while a rotation and double clipping plane evinces a peripheral ring of clustered CD16/32. Rainbow spectrum of the green channel uncovers the high fluorescence in the borders of the phagocytic cup, while the fluorescence profile plot of the same channel lets us see the fluorescence peaks of the peripheral ring (1,2) along the orange broken arrow.

Study of the safety of CD47 and SIRPα blockade in Glioma mouse model

In order to test a therapeutic strategy in vivo in immune-competent, syngeneic and orthotopic glioma model, since we demonstrated that 1) GAMMs account for the 30% of the cells within GBM human samples and they are able to phagocytose glioma cells; 2) primary microglia and microglial cell lines are able to eliminate glioma cells in a proinflammatory environment; and knowing that 3) murine microglia is able to actively target glioma cells by forming effector phagocytic interfaces; we opted for candidates able to potentiate these phagocytic events. Thus, the ideal signal to be targeted is the anti-phagocytosis interaction SIRPa-CD47. SIRP α is a receptor with an ITIM, what means that when triggered, phagocytosis does not take place. It recognizes CD47, which is expressed on cells as a “don’t-eat-me” molecule, and is described to be overexpressed in glioma cells including GL261 (154). For this reason, we thought that the best option would be to use neutralizing antibodies

against these receptors, to see if cells expressing SIRP α, such as microglia/macrophages, would eradicate the tumor cells which overexpress CD47. We independently tested both strategies (anti-SIRPα and anti-CD47) separately to decide which one is the safest and more effective for the animals in our immune-competent model. Importantly, we only used the systemic approach (i.p. injection) in order to reinforce and value the less invasive therapeutic intervention. One week after tumor implantation, a first dose of blocking antibody (either anti- SIRP α or anti-CD47) was administered to the mice (i.p.), and the second dose of the same blocking antibody was injected seven days later in the same way (**Figure 29 A**). Animals were monitored throughout the experiment, their bodyweight noted and when they reached the endpoint parameters, mice were sacrificed. Most importantly, although not statistically different, some of the anti-SIRPα-treated animals showed an extension of their survival in contrast with anti-CD47 treated animals, which showed a very poor survival rate (**Figure 29 B**). As a telling example, the first mouse to be sacrificed was one animal treated with CD47 blocking antibody. However, blocking SIRP α tended to extend the mice's life about 10 days. Although some additional experiments, as increasing the number of animals, should be done to strongly corroborate this encouraging result, targeting SIRPa seems more effective in this GBM model.

We relied on bodyweight as a general parameter of the mice's wellbeing (**Figure 29 C**). Generally, mice augmented their bodyweight the first two weeks after tumor implantation, however, there was a turning point where mice started losing weight, never gaining it back. This weight loss was significantly higher in anti-CD47 treated animals if compared with the control group, while anti-SIRP α treatment had the opposite effect, being the bodyweight curve significantly higher in treated animals if compared with the control group. This CD47 neutralization raises safety concerns since it worsened the prognosis of mice bearing a GL261 brain tumor, while SIRPα blockade seemed to avoid, or at least delay, the general deterioration seen in untreated mice.

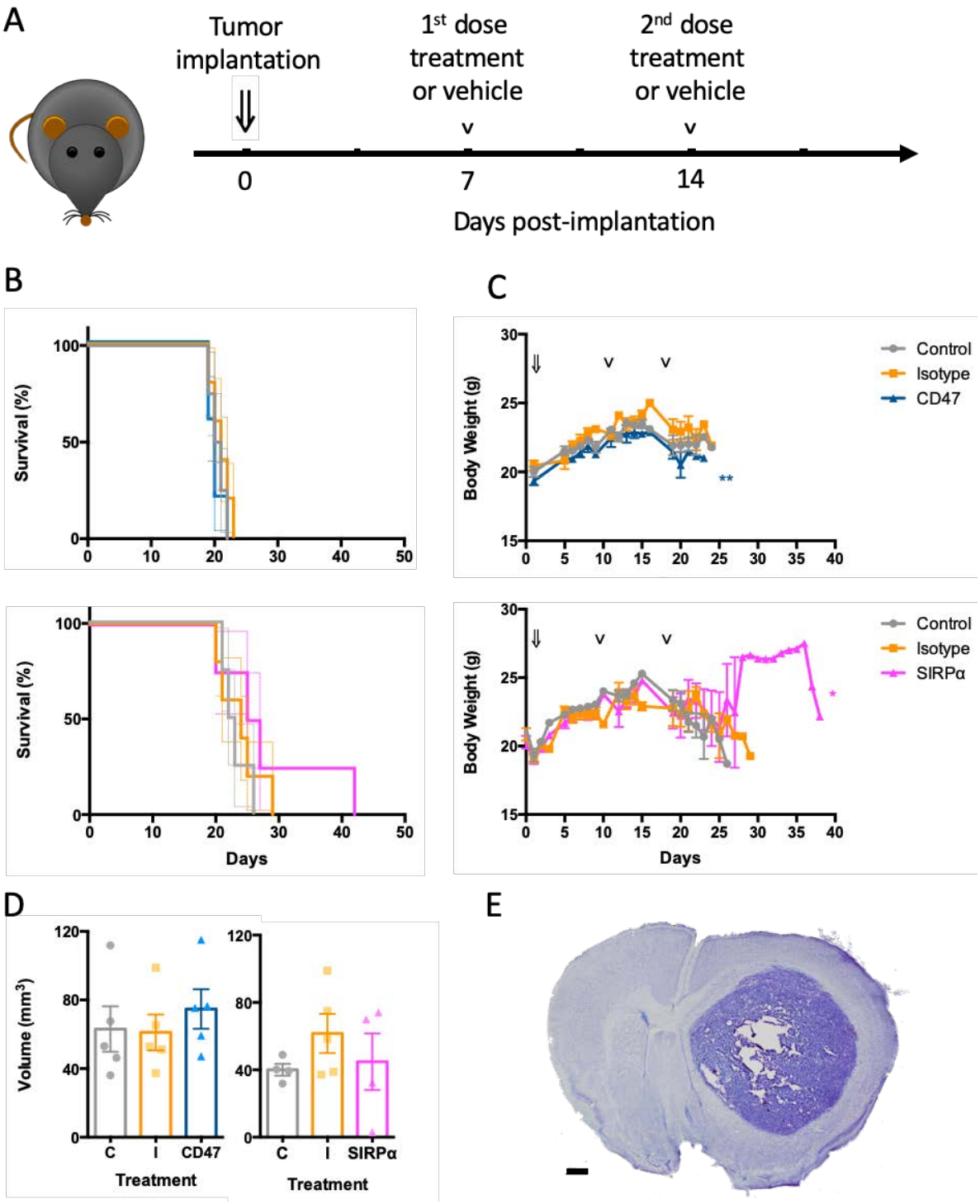

Figure 29. Blocking SIRPa induces a better outcome than blocking CD47 in immunocomptent glioma mouse model. A. Schematic showing striatal GL261 tumor implantation and subsequent treatment schedule (on days 7 and 14) using checkpoint blockade antibodies anti-CD47 or anti-SIRPα. B. Kaplan-Meier curves showing percent survival (mean ± SEM) of tumor-bearing mice (n=4-5/group) intraperitoneally treated with either the blocking antibody (anti-CD47 in blue; anti-SIRPα in pink), a rat IgG isotype (yellow), or saline vehicle (gray). Anti-SIRPα treated animals showed longer survival than anti-CD47 treated animals, although Log-rank analysis showed no significance when comparing curves. C. Bodyweight progression of the animals as a reflection of their overall health state, arrowheads indicate the treatment days (7 and 14) after tumor implantation (on day 0, arrow). *P<0.05; **P<0.01 vs. isotype. D. Scatter dot plot representing mean ± SEM (n=4-5/group) of the tumor volume measured by the Cavalieri method. Kruskal-Wallis test showed no statistically significant differences between groups. D. Mosaic of 20X brightfield images of a Nissl-stained section used to measure the volume of the tumor. Scalebar=500 µm.

By measuring the area of tumors in the slices of a whole series stained by Nissl staining (**Figure 29 E**), we calculated the volume of the tumors (**Figure 29 D**) by the Cavalieri principle, turning out to be the volume no different among treatments at the time of sacrifice. Moreover, this staining revealed a large area of necrosis in the tumor core in all cases.

The spleen was also extracted, measured and weighed as a general indicator of the mice's immune state (**Figure 30**). Although there was a general tendency of smaller spleens in animals treated with both immunotherapies, there was not enough evidence to state that the treatment had a significant effect in the splenic length, weight nor in the organ's organosomatic index.

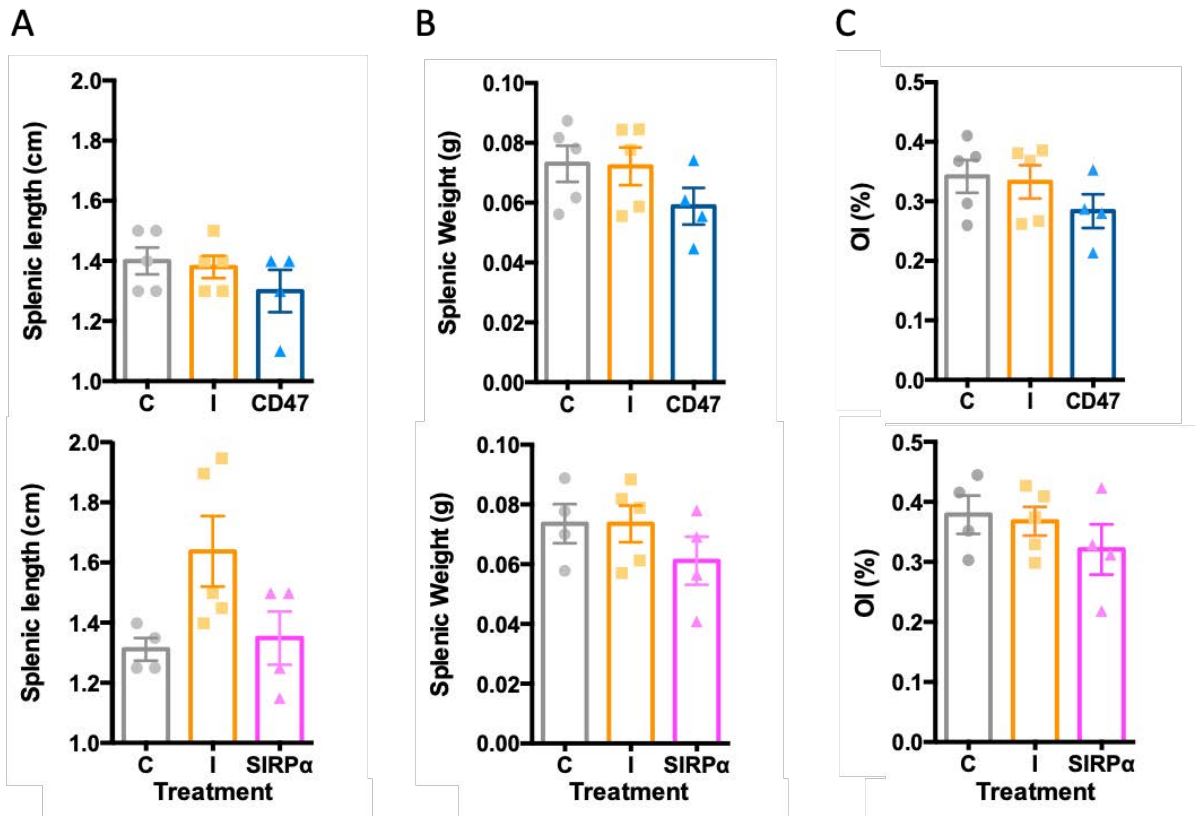

Figure 30. Treatment with anti-SIRPα or anti-CD47 do not show apparent reduction of the spleen of GBM induced animals. A. Scatter dot plot of the length of the spleens before intracardiac perfusion. Kruskal-Wallis test shows no evidence to assume differences between treatments. B. Although a tendency to be reduced, scatter dot plot of the weight of the spleens before the mice's death does not display an evident change in the weight of the organ in the different groups. C. Scatter dot plot of the organosomatic index (OI), obtained by dividing the weight of the spleen by the mouse's final bodyweight x100, does not display a significant difference among treatments.

SIRP α neutralizing antibodies, as opposed to CD47, decreases cellularity at the core of murine glioma

As cellularity is a crucial factor for evaluating the aggressiveness of the tumor, we analyzed this factor after both immune-therapeutic approaches. Some extensions of tumorigenic tissue were found missing, probably due to necrotic areas, or the chaotic nature of the vasculature, or both. Avoiding blank necrotic areas, we took sampling images in different areas of the tumor, which we categorized as tumor core (the central part of the tumor) or tumor periphery, which would potentially correspond to the invading/growing areas.

Quantification of cells within these two areas displayed no differences in the treatment with anti-CD47 vs corresponding controls (**Figure 31 A, C**). However, the treatment with SIRP blocking antibody showed a significant reduction in the cellularity in the tumor core, in comparison with its control group (**Figure 31 B, D**). This decrease of cellularity in the core after SIRPα blockade is compatible with a more efficient phagocytic activity of GAMMs. Interestingly, assuming that the invading areas occur in the periphery of the tumor, it is logical to speculate that the core may represent older parts of the tumor where the phagocytic activity by GAMMs and tumor cell elimination has already taken place.

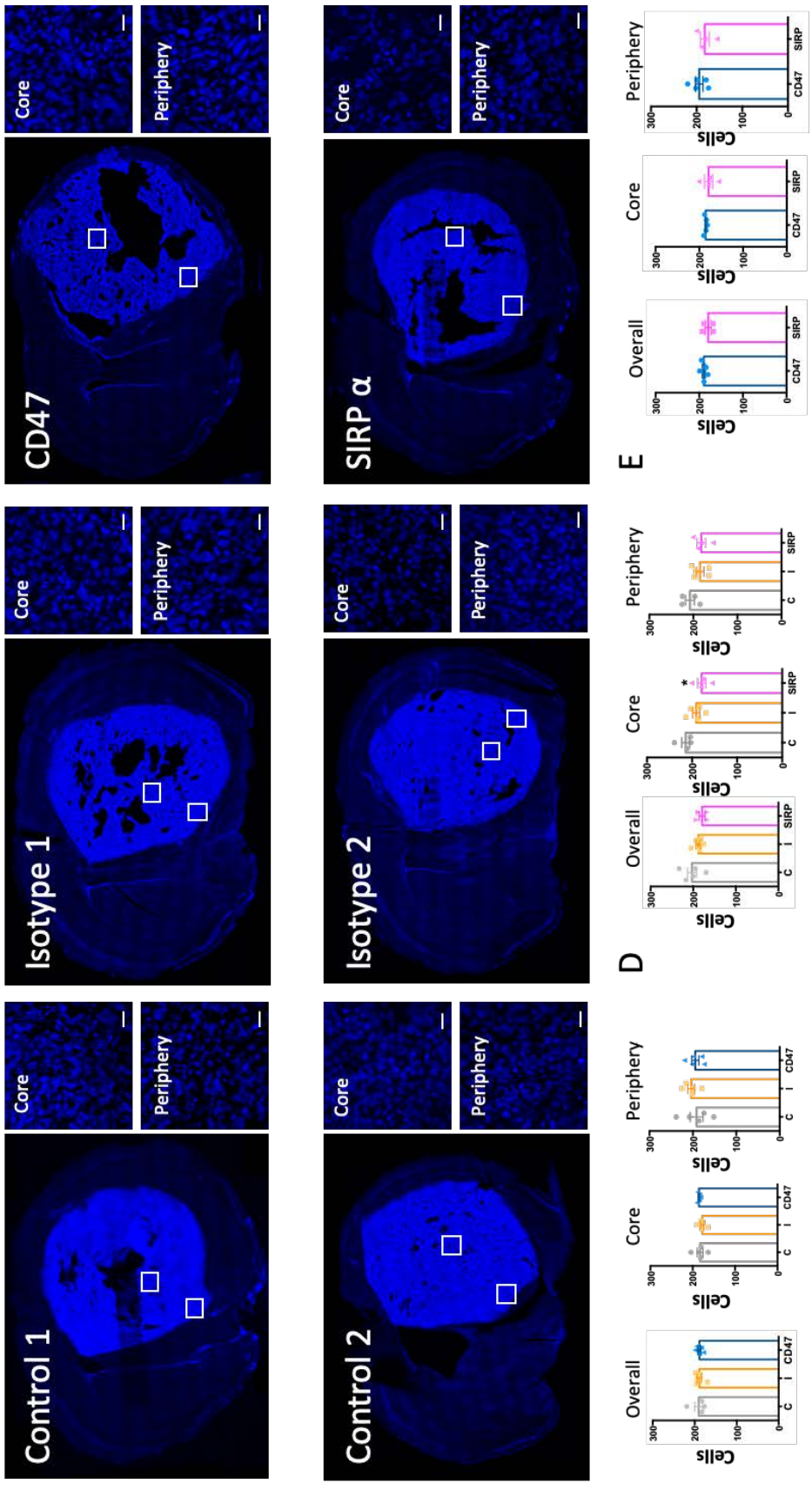

Figure 31. Blocking SIRP α reduces cellularity at the core of the tumor in GL261 glioma model in vivo. DAPI staining was imaged at 10X to make mosaics of single slices of the induced murine glioma, and in high-resolution confocal microscopy to be able to quantify cellularity in the anti-CD47 (A) and the anti-SIRP α (B) experiments (Scale bar=20 um). The number of cells per slice is shown in the entire tumor (overall) regardless of zones; and in the tumor core and periphery distinctly, in both CD47 (C) and SIRP experiments (D), and comparing both treated groups only (E). *p<0.05 vs C.

CD47 and SIRP α neutralizing antibodies do not affect microglia/macrophage numbers in murine glioma

To rule out whether the therapeutic efficiency was due to an increase of GAMMs, or that SIRPα blockade modified infiltration, Iba-1 staining was performed to count individual cells. High Iba-1 immunoreactivity was observable even outside de presumable tumor, for instance along the corpus callosum, what evidences a high immune reaction and inflammation across other nearby regions of the brain (**Figure 32 A, B**). However, we centered our detailed study to the actual tumor areas.

In the first place, we counted the amount of Iba-1 cells and found that although both immunotherapies tend to slightly increase the numbers of these immune cells, this result was not found to be statistically significant (**Figure 32 C, D**). Moreover, as we had also quantitated the total amount of cells, we were able to calculate the percentage of cells which are GAMMs within the tumor, and found that this number was ranged from 5 % to 15 % in the CD47 experiment; and from 6 % to 22 % in the SIRP α experiment. In general, the percentage of GAMMs in the induced mouse tumor was found to be comparable to those in the human tumor nearest to the TP in the D region of the HA (previously shown in **Figure 5**).

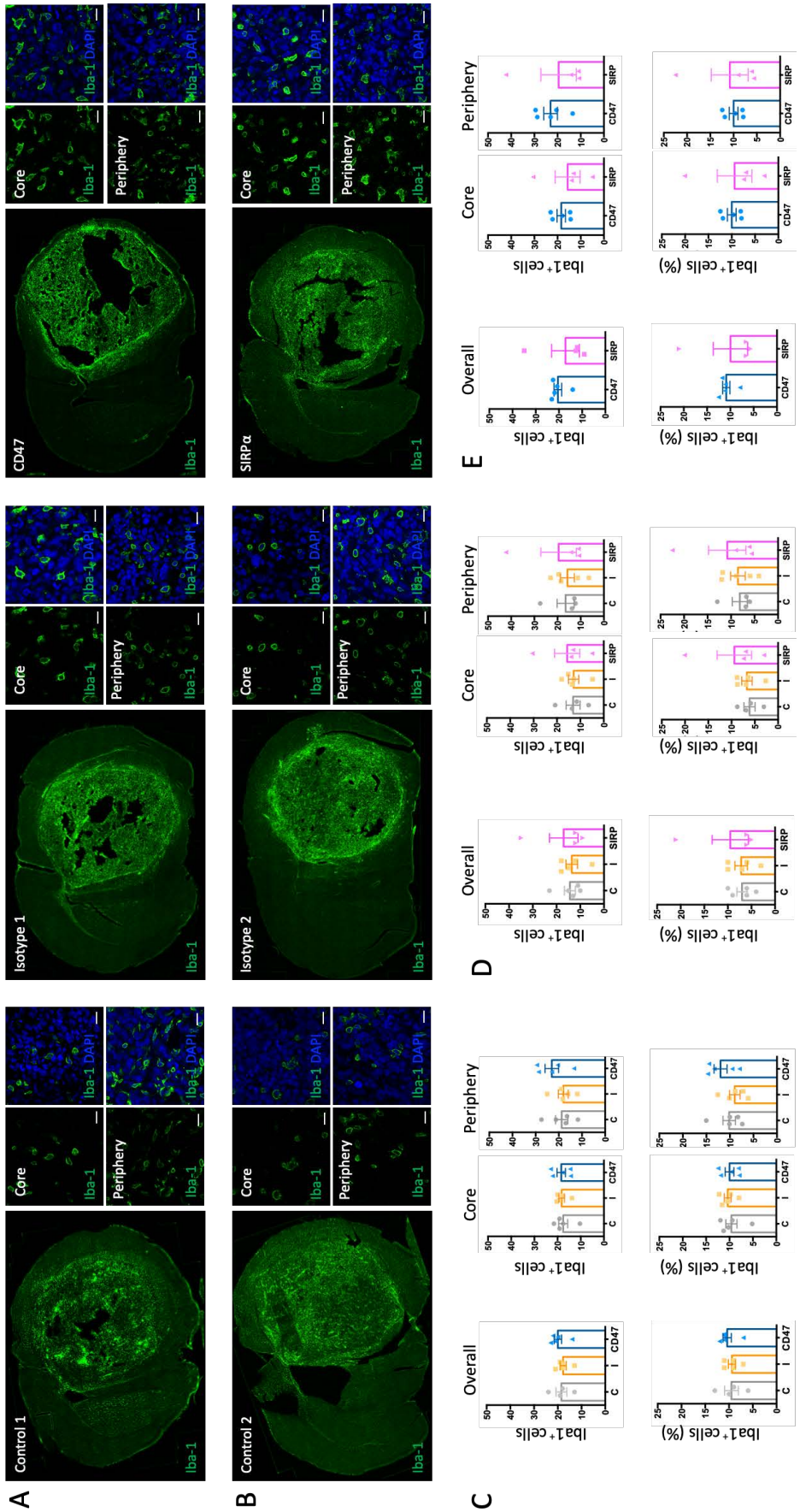

Figure 32. Treatment with anti-CD47 and anti-SIRPα do not change the numbers of GAMMs in GL261 tumors. Iba-1 staining was imaged at 10X to make mosaics of single slices of the tumors, and in high-resolution confocal microscopy was conducted to be able to discriminate GAMMs and quantitate them in the anti-CD47 (A) and the anti-SIRP α (B) experiments (Scale bar=20 um). The number of cells per slice is shown in tumor as a whole (Overall) regardless of zones; and in the tumor core and periphery distinctly, in both CD47 (C) and SIRP experiments (D), and comparing both treated groups only (E). No changes were seen in any of the comparisons.

Microglia/macrophages in GL261 tumors efficiently phagocytose

Iba-1 staining was also imaged in high resolution in order to visualize phagocytosis. This careful analysis of GAMMs in murine glioma revealed events that were resembling the interactions described in vitro: infiltrated GAMMs were able to bind non-myeloid cells and establish a very close apposition to potentially engulf them. In frequent cases, we could see Iba-1$^+$ cells contacting a target nucleus and establishing a synaptic interface, often in a flat disposition and showing a particular clustering of the calcium-binding protein at the interacting surface. To characterize the interacting cells, we identify PU.1$^+$ /Iba-1$^+$ cells as GAMMs and PU.1$^-$/Iba-1$^-$ as the target cells (**Figure 33**). In the events with a clear interface with the target, Iba-1 was disposed forming a peripheral ring in the external area of the interaction and in some cases with an increased accumulation at the center that suggested the formation of a possible central cluster. We also detected events were PU.1$^+$ /Iba-1$^+$ cells were forming a phagocytic cup towards PU.1$^-$/Iba-1$^-$ cells. In these cases, the Iba-1 rich interacting cup showed accumulation at its peripheral limits, as well as a potential central cluster. We could also see the orientation of the GAMM's nucleus, with the nuclear indentation towards the target, which usually host the MTOC and Golgi apparatus, which strongly suggested the active orientation of the cell toward the target (**Figure 34)**. We have also visualized events of phagocytosis using this set up of immunolabeling, in which a nucleus, usually with pyknotic features, was seen inside of a phagosome of a PU.1$^+$ /Iba-1$^+$ cell (**Figure 35**). With these markers we were able to distinguish the non-myeloid origin of the target being phagocytosed. Most often phagosomes contained one pyknotic nucleus, sometimes apparently fragmented, per GAMM, which suggests a one-to-one phagocytic event. However, and interestingly, we have also spotted events of several phagosomes with multiple nuclei within one single GAMM, which questions whether multiple phagocytoses may also take place at the same time by a single GAMM.

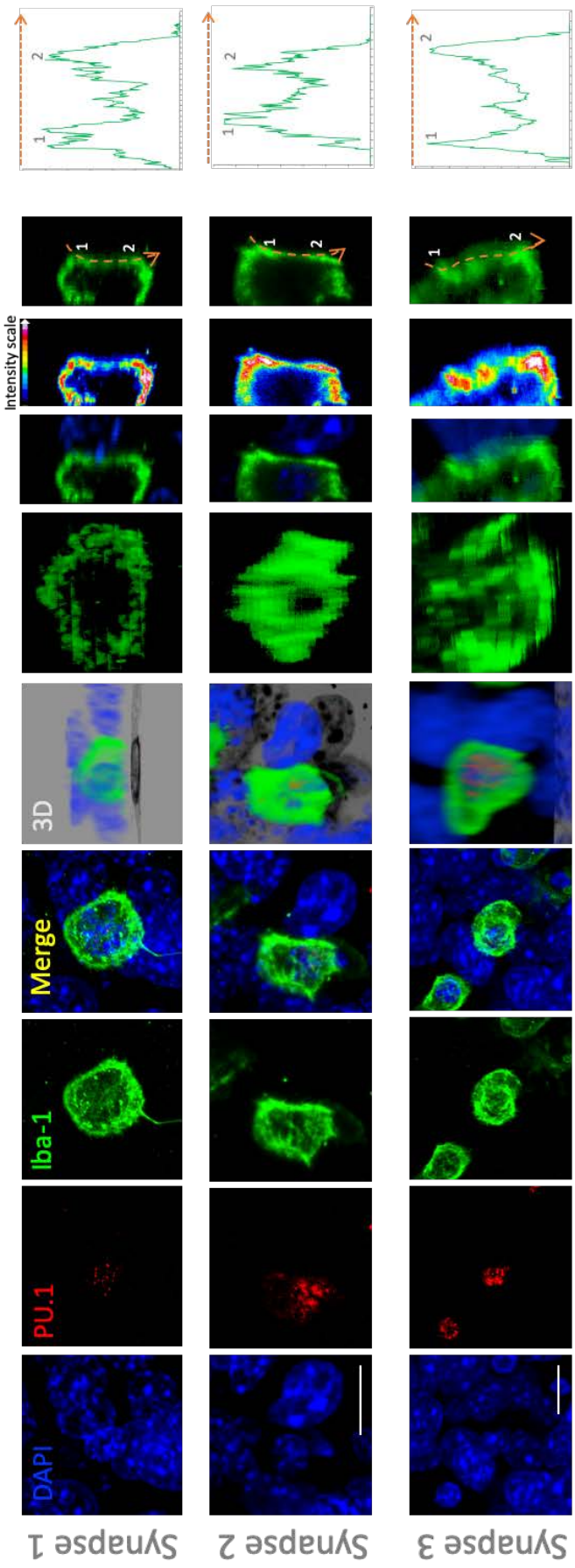

Figure 33. GAMMs cluster Iba-1 peripherally at the flat interface. Three different interacting synapses are shown in which microglia/macrophages closely bind their target cell and establish a flat interface. For all three synapses we show the maximum projection of the fluorescence, for DAPI (blue), PU.1 (red), Iba-1 (green) and their merged image (Scale bar = 10 um). Next, a 3D reconstruction with rotation is shown to better visualize the flat interface and a double clipping plane, with rotation and zoom in is performed to show the peripheral ring formed by the molecule. A single slice where the flat interface is more patent is also shown in rainbow spectrum, where blue is the least intense and white the most intense, and displays the higher distribution of the molecule in the external borders of the interface. The same slice is also shown in green, where the orange broken arrow indicates the area taken to draw the fluorescence intensity plot, where the peripheral ring corresponds to peaks 1, 2.

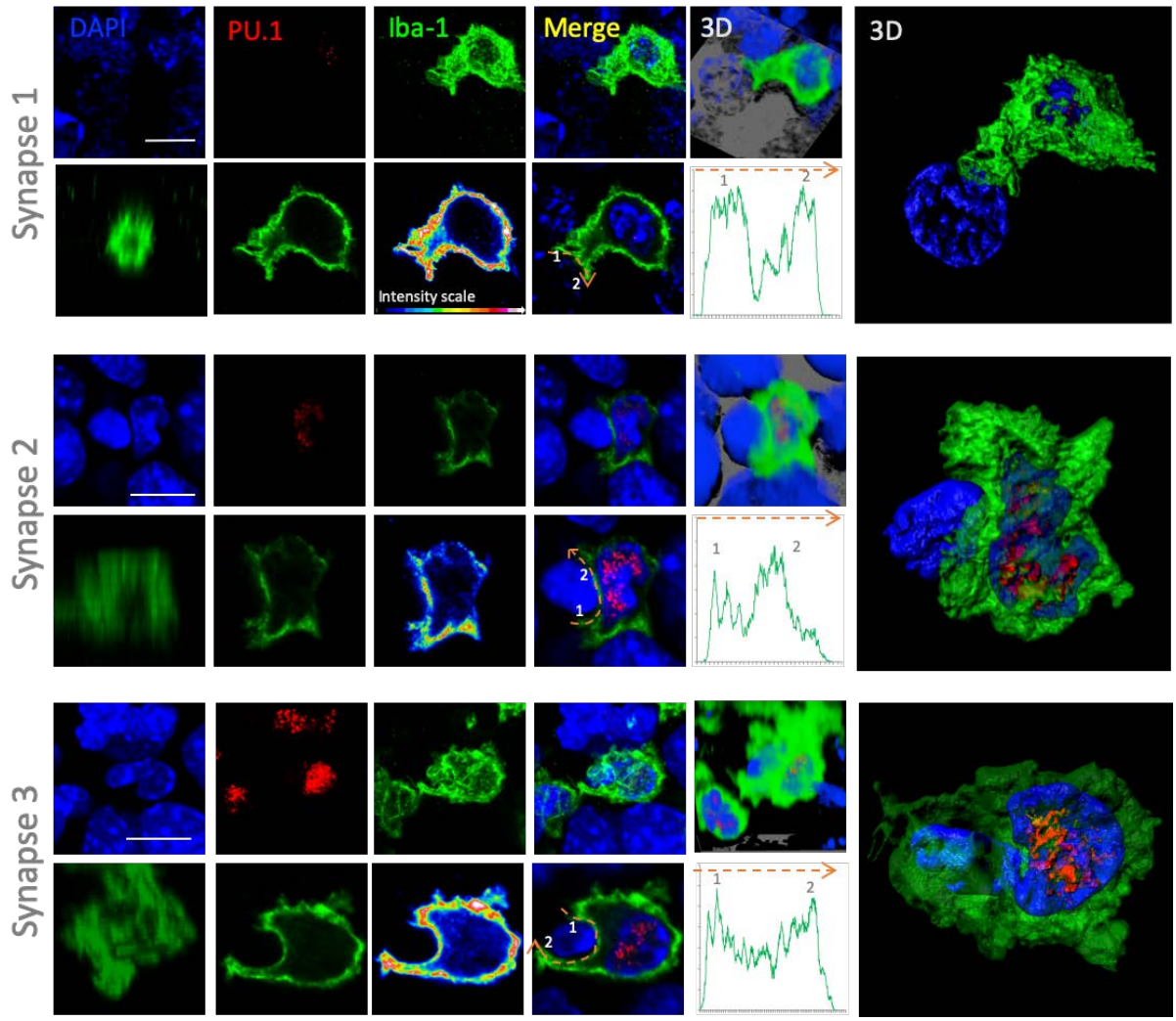

Figure 34. Iba-1 molecule is clustered at the phagocytic cup. Three different phagocytic synapses are shown in which microglia/macrophages surrounding non myeloid target cells. For the three phagocytic synapses we show the maximum projection of the fluorescence, for DAPI (blue), PU.1 (red), Iba-1 (green) and their merged image (Scale bar = 10 um). Next, two 3D reconstructions with rotation are show to better visualize the interaction between cells and in two cases the pyknosis of the target nuclei. A double clipping plane is also shown, where the reminiscence of a peripheral ring and central cluster of Iba-1 can be seen. A single slice is also shown in rainbow spectrum, where blue is the least intense and white the most intense, and displays the higher distribution of the molecule at the sides of the interface, in the phagocytic cup. The same slice is also shown in green, where the orange broken arrow indicates the area taken to draw the fluorescence intensity plot of the interface, where the peripheral ring corresponds to peaks 1 and 2.

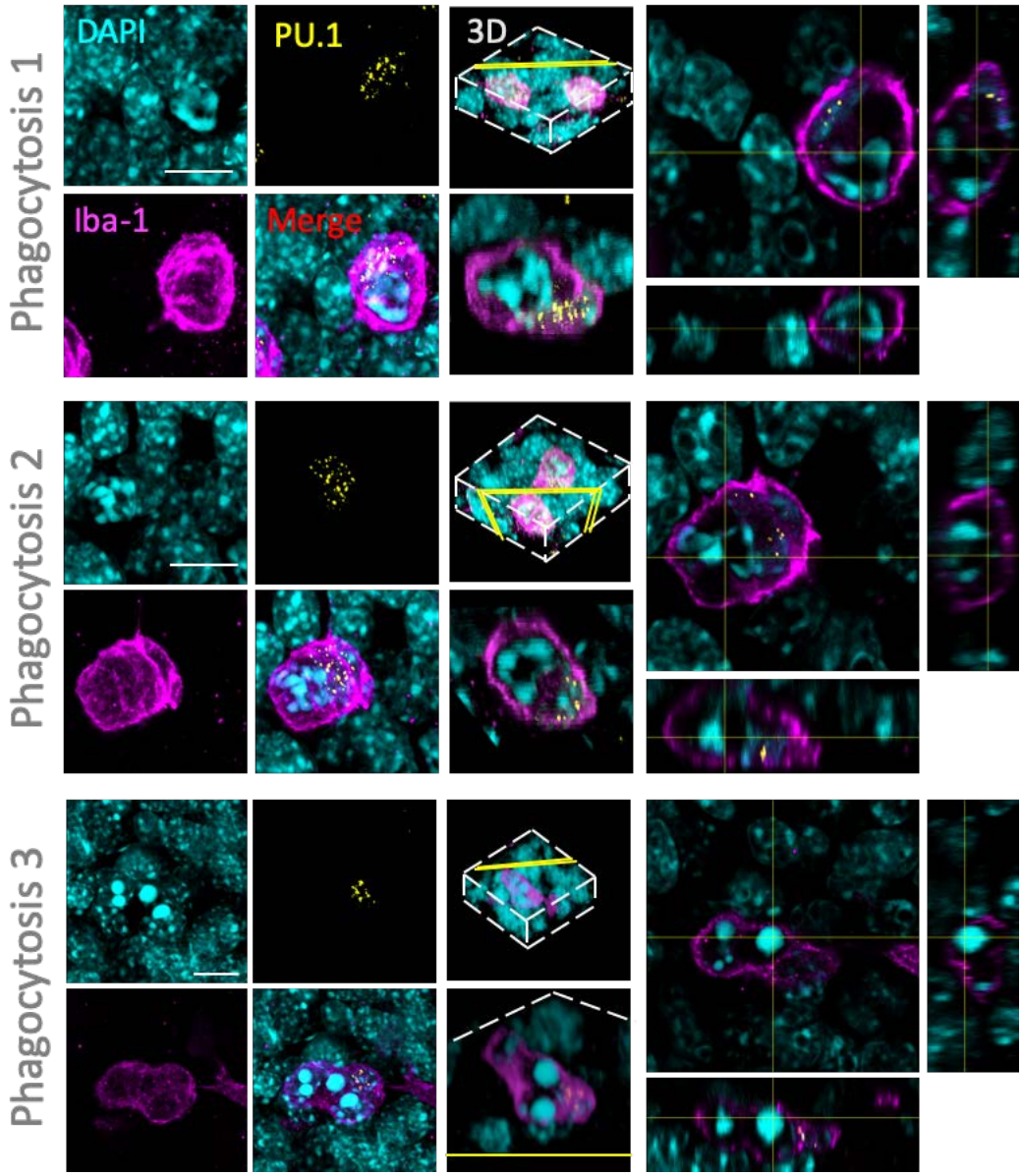

Figure 35. Microglia/macrophages effectively phagocytose in murine glioma. Maximum intensity projections for the nuclear counterstain (DAPI, cyan), and the myeloid markers PU.1 (yellow) and Iba-1 (magenta) are shown along with the merge (Scale bar= 10 um). The confocal Z- stack is reconstructed in 3D and with a double clipping plane we can discern, inside the Iba1^{+} cytoplasm, the myeloid nucleus positive for both markers, and the nuclei being phagocytosed in a space which is negative for Iba-1. Orthogonal views of the same image show the nuclei being phagocytosed completely surrounded by the effector cell.

Blocking SIRP effectively increases the phagocytic capacity within tumors

Therefore, knowing GAMMs in GL261 tumors hold their phagocytic capacity, we quantified the amount of remaining phagocytoses at the moment of the animal's death to see if the immunotherapy with neutralizing antibodies against CD47 / SIRP α affected this important feature. Detailed quantification, considering the periphery and core of the tumor, showed that phagocytoses occurred among all groups (**Figure 36**), treated and untreated, and that although blocking either receptor seemed to boost phagocytosis (in the core of the tumor in the case of CD47 blockade (**Figure 36 C**) and overall in the case of SIRP α (**Figure 36 D**), data did not reach significant differences. Furthermore, as we had observed active phagocytic GAMMs at this state, we calculated the ratio of phagocytosis by dividing the number of phagocytoses by the total number of $Iba1^+$ /$PU.1^+$ cells. While this ratio did not significantly vary among the internal experimental groups, which may be expected considered the different experimental time-point, we observed a significant increase of the phagocytosis ratio in the peripheral parts of the tumor in anti-SIRPα treated animals compared with animals treated with anti-CD47 (**Figure 36 E**). These results strongly suggest that a systemic immunotherapy targeting the SIRPa-CD47 axis may have a completely different output depending on which of the receptors is blocked. Our analyses indicate that it is more effective to act upon the effector cell, by blocking SIRPa, than upon the target cell, by blocking CD47. Finally, and taking into account that GAMM infiltration is not increased by the treatment, our study advocates that blocking SIRPa effectively increases GAMMs' phagocytic capacity.

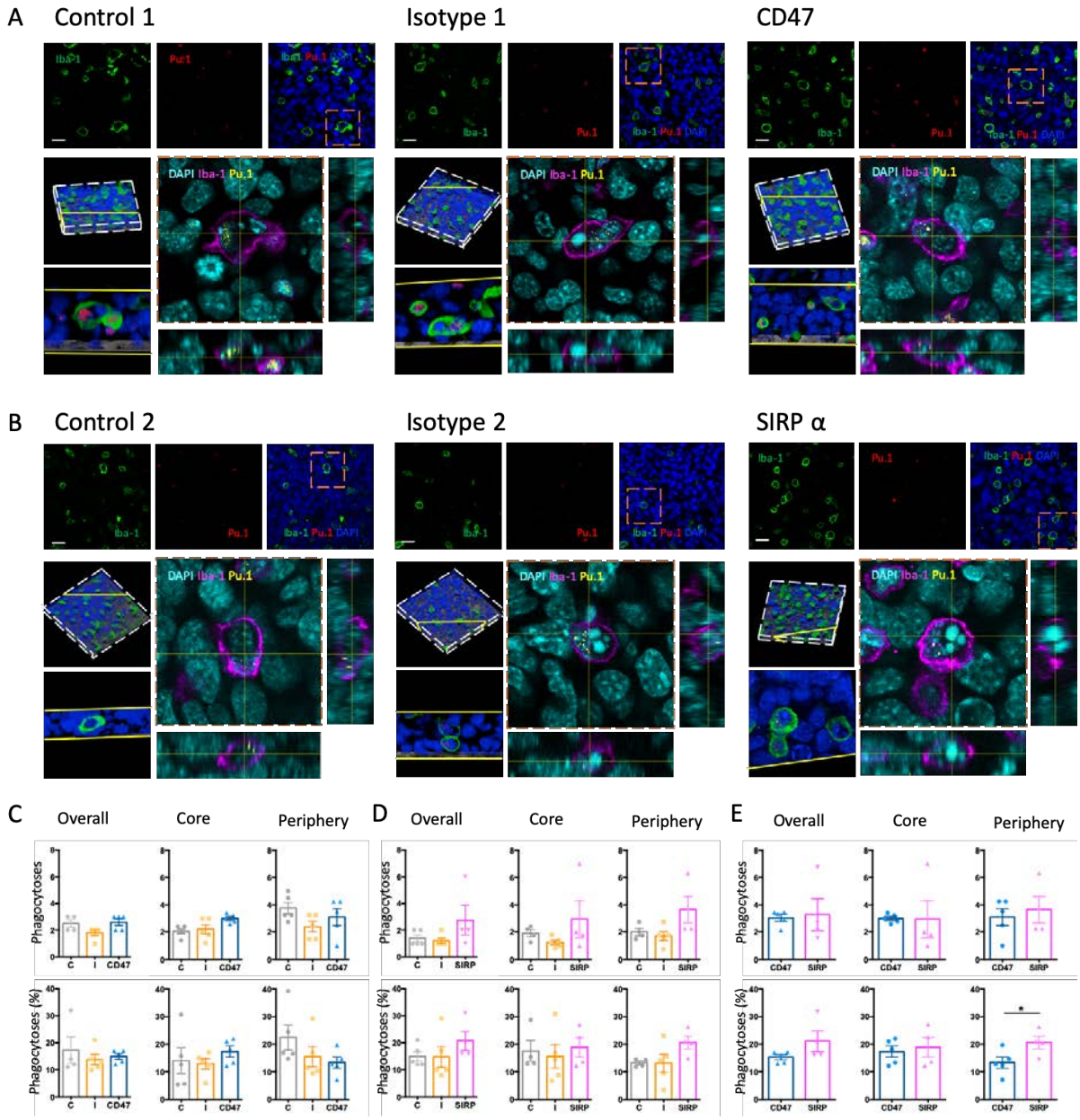

Figure 36. SIRP α neutralizing antibody promotes phagocytosis in the tumor periphery. Phagocytic events are found among all experimental groups, in the CD47 (A) and the SIRP α neutralization (B) experiments. An example of phagocytosis is shown in each one of them, first by a single confocal Z slice of the green (Iba-1) and red (Pu.1) channels; as well as these and merged with blue (DAPI). Next, a 3D reconstruction is displayed with the location of the double clipping plane (yellow lines) displayed on the bottom. Orthogonal views evince the nuclei (cyan) inside the Iba-1 (magenta) cytoplasm, one being phagocytosed and the other one being from the microglial cell (expressing PU.1 in yellow). C. Quantification of the phagocytoses per image in the CD47 experiment, taking into account all images (overall) but also classifying them depending on the area found (periphery or core). The phagocytoses counted were also divided between the number of Iba-1 cells to have the percentage. The same is shown for the SIRP α experiment (D). Comparison of only the two treated groups is displayed in panel E. Kruskal-Wallis statistical test was performed in C and D, and Student's T-test in E. * $p<0.05$

General Discussion

The first relevant contribution of this thesis is the discovery of GAMMs populating and traveling through PPs to phagocytose tumor debris (155), as it had never been reported before, and challenging a previous and highly cited publication that had denied the presence of an immune component in this GBM hallmark (156).

As PPs are areas that are thought to contribute to tumor invasion and expansion, the understanding of the GAMMs' behavior in this hypoxic microenvironment presented in our results might shed light to the way these cells facilitate the development and maintenance of GBM. In this context, we described a high expression of the receptor CD163 in GAMMs traveling across the PP, which indicated the anti-inflammatory nature of these cells here (60). GAMMs at this environment become elongated probably by the phenomenon of traveling itself but also potentiated by the hypoxia, as we have seen this condition makes microglial cells undergo a kinetic morphology; while a hypoxic gradient stimulates the persistence of the cells by increasing their Euclidian distance in vitro (**Figure 11**). Moreover, the presence of the centrifugal GFAP fibers at the PP appears to grant a substrate for tumor-associated GAMMs to successfully reach the focus of the lesion, where MHCII expression emerges, at the necrotic border (**Figures 3E, 4B-C**). In tumor microenvironments it has already been described that specific physical changes like the fibrillary disposition may directly intervene in the invasiveness (157), but now it is the first time reported in GBM's PPs. Furthermore, as CD163 is a receptor in the anti-inflammatory spectrum, it is expressed as expected where there are malignant glioma cells, this is, not in the necrotic border, but in the I and D regions (**Figure 5**). Additionally, PPs are putatively formed in the context of a vessel collapse (156), where there might be erythrocyte lysates such as hemoglobin/haptoglobin complexes, precisely the ligand of CD163 scavenger receptor expressed by GAMMs. This receptor specifically binds the hemoglobin/haptoglobin complex; therefore, it is logical to suggest that it may also intervene in the polarization towards the focus. Once GAMMs arrive to the area where the phagocytosis takes place, mainly in the P regions, the cells skew their phenotype to express MHCII, which is considered as belonging to the proinflammatory spectrum.

Further, we help elucidate the motility of GAMMs in GBM by the analysis of the samples but also with experimental modeling in vitro. We decipher the orientation and the haptotactic mechanism of microglial migration towards the necrotic focus (**Figures 10 and 12**), and by means of cell cultures we confirm the centrifugal escape of glioma cells away from the hypoxic source (**Figure 11**), as previously described by others (156). However, microglia do not escape from the hypoxic environment but responds to this gradient by increasing their cellular persistence (**Figure 11**). Considering the location at the PP, this result suggests that microglia adopt this behavior while skewing towards an anti-inflammatory phenotype. This anti-inflammatory spectrum may be protumoral, while the hypoxic area and damage may expand. Then, in this microenvironment GAMMs might interact with GFAP fibers which point out the direction of the hypoxic origin and follow their oriented path. Altogether, these factors suggest that GAMMs may be in a tumor-permissive mode along the PPs. In addition, they probably must repolarize towards a phagocytic phenotype when reaching the necrotic focus, recognize, phagocytose and digest the targets, all of which may be crucial for the successful escape and migration of glioma cells towards new areas. This, as well as the containment of the necrosis, the angiogenic capacity of the myeloid cells and the debris clearance might be potential advantages that glioma cells may take for GAMMs infiltrating the necrotic areas, which are related significantly with poor patient survival (158). Altogether, the pernicious presence of microglial cells in GBM still remains paradoxical: as GAMMs have the capacity to phagocytose, it could be expected for them to phagocytose grievous glioma cells, but instead they seem to be favoring the expansion. This could be because their capacity is probably restricted to the areas near the necrotic focus, the opposite direction of the tumor expansion, or at least their phagocytic capacity is not enough to keep up with the fast tumor growth and expansion.

In the present thesis we also demonstrate that GAMM population tends to be increased in the overall tumor, while it is diminished at the vascular infiltration sites as tumor Ki-67 and vimentin expression increase, suggesting that GBM creates an environment to facilitate this colonization by tumor cells (**Figure 3**). This could be due to tumor cells making use of GAMMs for their angiogenic capacity, as malignant glioma cells profit from vessels to invade new areas (62). Therefore the GAMMs may be attracted to the tumor environment but given that that tumor cells invade and self-

renew in vascular areas could result in a potential competition by the latter for this niche displacing the GAMMs from these areas (159). While this is what may happen in perivascular regions, we can see different tendencies in other areas of the tumors. Notwithstanding, in perinecrotic zones excluding the case of PPs, MHCII expression tends to increase (**Figure 3E**), and as we have seen that phagocytosis takes place here, it is logical that GAMMs with phagocytic capacity express more MHCII, an identifying marker within the pro-inflammatory spectrum. Certainly, in order to see if these tendencies become significant, it would be ideal to increase the amount of tumor samples analyzed. Furthermore, p65 NF-κB staining shows no translocation of the signaling molecule in these myeloid cells despite the expression of MHCII, what further confirms the anti-inflammatory effect of the tumor. Beyond, it can even be distinguished an area in which p65 NF-κB is highly expressed while MHCII is not, whereas other surrounding areas are more immunoreactive for MHCII and not for p65. These two areas could correspond respectively to the “tumor nest” and the “stromal” area, being the latter full of myeloid cells which presumably aid the invasion of new areas by the degradation of the extracellular matrix (34). This information is of relevance, as it could be potentially used for therapeutic purposes against GBM, targeting GAMMs. The natural capacity of the tumor to attract immune cells could become positive, if we were able to reprogram the effector cells to phagocytose glioma cells in the tumor nest areas.

As GBM remains incurable, new therapeutic strategies in this immunological spectrum have to be considered. We have seen that GAMMs are effector cells which are able to phagocytose human GBM cells (**Figures 13-14**). Consequently, GAMMs are perfect candidates to eliminate the tumor cells, especially because of their high infiltrating proportion (**Figures 3 and 5**). Thus, this was the main objective for the second part of this thesis: to be able to promote phagocytosis of glioma cells. This goal was explored both in cell cultures, as well as in an immunocompetent murine in vivo model.

Hence, having already established cell cultures, we believed that potentiating a pro-inflammatory signaling, via p65 translocation to the microglial nucleus, might be a successful way to reprogram GAMMs to increase their phagocytic rate in tumorigenic areas. In order to study this, our in vitro experiments comprised primary glia as well as a murine cell line; both co-cultured with same-species glioma cell lines. Thus, we

confirmed that primary rat microglia and BV-2 cells were positive responders to a pro-inflammatory stimulus, visualized by the translocation of p65 to the nucleus (**Figures 16-17**), and they were able to eliminate glioma cells when co-cultured (**Figures 17-18, 21-22**). Firstly, upon LPS administration, p65 translocation to the nucleus was achieved, confirmed by the increase of nitrites in the extracellular medium cells were cultured in and the visualization of the staining in the microscope. When co-treated with LPS and Ibu, p65 translocation and expression seems exacerbated. The possible reason may be because one of the genes expressed when the NF-κB pathway is activated is the *cox-2* gene. Furthermore, the products of the enzyme COX-2 are cyclopentenone prostaglandins, and these have various targets within a cell, such as IκB (160). PGs normally close the feedback loop. Therefore, when they are synthesized NF-κB is not overly translocated. When treating with LPS and Ibu, due to the action of the latter, PGs are not synthesized, therefore the inhibition is inhibited and so IκB is degraded. Thus, the NF-κB complex is free to translocate to the nucleus and probably does not cease to do so. We actually observed that NF-κB does not only translocate to the nucleus, but since it is not inhibited, it is also accumulated in the cytoplasm. This might be either because too much is synthesized and therefore not all of it can get to the nucleus, or because of the existence of dual controls for NF-κB, meaning there is a pathway to increase nuclear levels of NF-κB and another to control inherent transactivation potential (160). To elucidate which of both possibilities is true, future studies need to be done. On the other hand, primary glia cultures suggested that p65 translocation was successful upon administration of LPS and IFN-γ pro-inflammatory molecules, as these cells were polarized towards a phagocytic phenotype, confirmed by the quantitation of nitrites in the supernatants of the cells and further proved by the decreased number of glioma target cells; as well as the visualization of phagocytosis in high resolution confocal imaging. Moreover, when the target had already been engulfed, the translocation of p65 was not obvious (**Figure 18**), what suggests that effector cells might need another pro-inflammatory insult to undergo phagocytosis once again, or maybe that once the phenotype polarization occurs, p65 is not further needed, and cells maintain their phenotype as long as they don't receive an opposing stimulus. For this reason, it will be interesting to further study this process, perhaps by re-administrating pro-inflammatory stimuli to see if p65 translocation can be re-established in these conditions.

We also focused on the importance of the microenvironment to potentiate or avoid the phagocytic capacity of microglia. On the one hand, we did so by the administration of IL-4, which provokes a decrease in macrophage pro-inflammatory response (161), therefore being able to putatively repolarize the effector cells in the culture towards a non-phagocytic phenotype. On the other hand, the culture included astrocytes, better simulating the brain environment in which the tumor may settle. Consequently, we performed co-cultures of primary mixed glia and C6 glioma cells by adding IFN-γ/LPS as pro-inflammatory stimuli and IL-4 as anti-inflammatory in different order and see if the order affected how the microglia phagocytosed the tumor cells (**Figure 19**). However, although nitrite secretion confirmed a response by the glial cells, no clear increase in the phagocytic pattern was observed, probably because astrocytes also express receptors for these molecules, acting as buffer and affecting the environment and the signals microglia receive. For instance, upon LPS stimulation, astrocytes also activate their iNOS and are able to secrete nitrites, therefore the nitrites we quantitated could have been from astrocytic origin besides microglial, plus they might shift the microglial cells towards a tumor-supportive phenotype (162). Thus, these results highlight the importance of the astrocytic environment in the anti-tumoral response of microglia. Although the presence of IL-4 reduces the pro-inflammatory response, IL-4 has been reported to also trigger astrocytes to secrete factors, such as nerve growth factor (163) that could stimulate microglia towards an anti-inflammatory phenotype (164). Therefore, the anti-inflammatory effect of IL-4 in a mixed culture could be due to the astrocytic response as well as the IL-4 administration. Thus, the presence of astrocytes in the culture, as it occurs in the real tumorigenic scenario, could change the final output of the response. In conclusion, the environment of other glial cells should be considered to understand the full inflammatory response in brain tumors and more experiments are needed to be able to determine the final effect of these compounds on microglia to effectively promote phagocytosis of glioma cells.

Another important finding of this thesis is the visualization of phagocytic events of microglia towards entire glioma cells as targets. Studies of phagocytosis in vitro are usually done with opsonized beads (165), erythrocytes (166,167), or other non-eukaryotic cells like yeast (55) or bacteria (168). In our case, we have studied the phagocytosis of whole glioma cells in different set ups. We have done this in the first

place by means of BV-2 and GL261 cell lines, observing the potential steps in which microglia may reach glioma cells and contact them to phagocytose them. Secondly, we also visualize this mode of microglial phagocytosis in an in vivo glioma model, suggesting that this process may be intrinsic to the nature of the effector cells; which includes the recognition of the target, binding with the formation of a flat interface, the engulfment with the formation of a phagocytic cup, and potentially the final digestion (**Figure 37**). Similar steps have recently been categorized in a review by Morioka et al.; in which they term the steps “smell”, “taste”, “ingestion” and “digestion”, yet this analysis is reported in homeostatic conditions and when the targets are dying cells by apoptosis or opsonized erythrocytes (82). Importantly, we report in this thesis that microglial cells in vitro are not only able to phagocytose dying GL261 cells, but also glioma cells that maintained their cell membrane integrity and with no signs of cell death (**Figures 21-22**). Thus, we suggest that BV-2 microglial cells are able to phagocytose dead GL261 cells, which may be something expected, but importantly we also show that a process of phagoptosis may also occur, as phagosomes with pyknotic nuclei without the NucGreen probe included were seen inside microglial cells. What implies that the cell being engulfed had no time to include it in the nucleus, or that it died once inside the myeloid cell. This happened even under stochastic conditions, without treating BV-2 cells prior to glioma exposition, which might be due to the aggressive nature of these cells. Hence, apart from further exploring p65 renewal in these cells, the effectiveness of primary phagocytosis or phagoptosis should be analyzed after pro-inflammatory and anti-inflammatory stimuli.

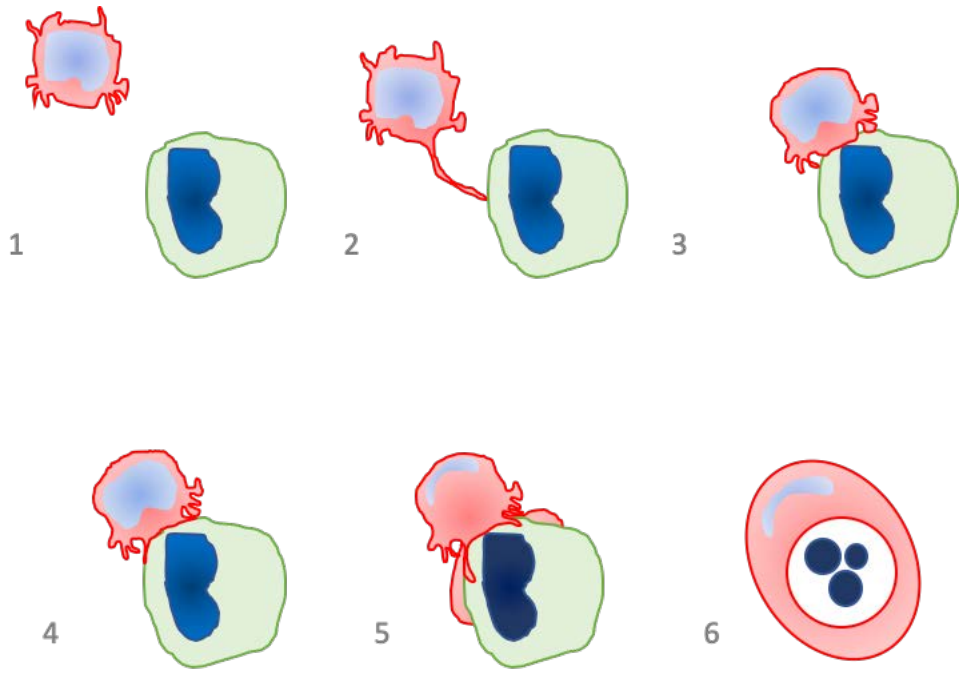

Figure 37. Diagram of the microglial/macrophage phagocytic action. Microglia/macrophages are "resting" while scanning the environment (1); and when they sense their target (2) they polarize towards it and attach with a flat interface (3) while they "decide" if the target must be phagocytosed. When overall signaling favors phagocytosis, they form the phagocytic cup (4) and a lamella protrudes under the target cell while the cup advances in an embracing manner (5) to finally completely surround the target cell and degrade or digest it (6).

Comprehensive visualization of the microglia-glioma interactions revealed particular arrangements of receptors involved in the phagocytic process. We did a detailed analysis of the distribution of the CD11b and CD16/32 receptors, which have been reported to have a role in target engulfment (169–171). We described here a particular distribution of both receptors in BV-2 cells. Both seem to be placed in the trailing uropod while the microglial cell is in a traveling shape (**Figures 23-24**). On the other hand, in cases when microglia reaches its target and an effector-target interface is settled, presumably when the Fc-γR is stimulated (79), they seem to form a peripheral ring at the external part of this interface (**Figures 25-26**). Interestingly, in some cases a potential smaller concentric ring can be slightly appreciated, coherent with reports that describe FcγR II (like CD32) forming concentric activation rings in human monocyte-derived macrophages in vitro (78). However, our analysis did not reach the sufficient resolution to convincingly visualize these additional fine features. Moreover, the analysis of the images suggests that concentric rings might be connected radially with each other since actin and tubulin cytoskeleton may directly intervene in the rearrangement of these molecules at the interface. Albeit, higher

resolution microscopy may be needed to further analyze this disposition. CD11b has been revealed to be required for Fc-γR activation at the phagocytic cup for Src activation, forming high avidity complexes and suffering lateral diffusion to be concentrated in phagocytic cups, also contributing to the adherence of the cell (79). However, in our images, besides visualizing the concentration of the molecule, we can also see the formation of a peripheral ring, which may be relevant for the engulfment of the target cell. This disposition and distribution of the molecules apparently suggests that both receptors (and possibly also Iba-1, as seen in vivo) are not needed for the initial recognition of the target, but it remains a difficult assessment, since they can be paralleled with the position and arrangement of TCR and LFA-1 in T-cells. In other stages, possibly while the phagocyte “decides” if the target should be engulfed or not, the function of both receptors seems to be more patent to keep the activation of phagocytosis, as CD32 and CD11b both contain an ITAM which gets phosphorylated in this process (77). On the other hand, Iba-1 has been described to be needed in the phagocytic cup for membrane ruffling upon phagocytosis, keeping Rac signaling cascade active and thus actin reorganization (172). However, the detailed 3D analysis through the potential steps of phagocytosis herein is novel, being the geometrical disposition of the Iba-1 receptor at the interface, together with CD16/32, and CD11b, an important aspect that reveals the involvement of a complex signaling when targeting glioma cells.

Knowing this information, it is tempting to speculate potential dynamics that occur while the target cell is being engulfed: the microglial cell may pull the glioma cell closer to its center of mass by forces initiated at the rings of clusters, especially by CD11b integrins, so the receptors involved may not only stimulate microglial activation, but also serve as physical anchors. Therefore, microglia may then keep the target close, possibly maintaining stable rings, and forming receptor-rich extensions around the target that may protrude, like arms, embracing it. As the studied receptors are surface receptors that bind the target and are required for activation, they may also be recycled and not engulfed, so the receptor could travel radially probably through actin filaments (172,173), to the periphery to be used, for example, during the formation of the arms that will surround the target cell, explaining the possible maintenance of the structure even during the late stage of the phagocytic cup. Importantly, it is important to consider that these dynamics may only

happen with big targets like entire cells, which might be physically difficult to engulf, while other smaller targets or target cells which are easily engulfed like opsonized particles or non-eukaryotic cells may not precise this elaborate distribution of the receptors and radical polarization of the cell; although some of the signaling could be maintained.

Finally, this thesis provides relevant data regarding two potential immunotherapies for GBM by using a mouse model to promote phagocytosis. Probably both immunotherapies stimulate the phagocytic capacity of GAMMs. However, when neutralizing CD47 with intraperitoneal injections, phagocytosis may occur, aside from the tumor mass, in all peripheral tissues, which may be a detrimental side effect resulting in a poor survival rate, similar to the control groups, an outcome that challenges previous reports (154,174). Presumably if anti-CD47 immunotherapy was given locally (directly in the brain tumor), the effect would have been better. When neutralizing SIRPα, the survival clearly increased in some cases (as an example, there was a mouse that lived almost 30% more than the rest). However, this is a first attempt to analyze the safety and effectiveness of the potential immunotherapy and, therefore, although it is a promising result, it should be replicated to avoid potential experimental variations. In future experiments, in order to confirm the tumor reduction or verify the tumor induction, it would be ideal to analyze the animals by magnetic resonance imaging, before and after the treatment, to establish more strong conclusions about the design of immunotherapy for GBM.

Tumor volume at the time of the sacrifice was not statistically different among treatments. This is expected since the sacrifice was performed when the animals had terminal clinical symptoms, independently if they lived longer or not. Interestingly, there was a tendency of presenting bigger tumor volumes in anti-CD47 treated animals whereas a tendency of reduction was observed with anti-SIRPα treatment. Moreover, although it should be further evaluated, visually the vessel caliber seemed to be different in the CD47 group, which would be compatible with hemolytic anemia induced by the treatment (119). As there may be less erythrocytes reaching the tumor (because they are probably being phagocytosed, for instance in the red pulp of the spleen) (175), intratumoral perfusion has to be stimulated, and this could be done by different mechanisms, like increasing number of vessels, their caliber, or the amount of ramifications. Previous studies of the group show that in human GBM

samples, blood vessels are bigger as the aggressiveness is increased, with a greater disruption of the collagen basement membrane and the endothelium (176). The heterogenicity in tumor associated vessels may provoke also heterogenicity in the tumor parenchyma, probably inducing more perfused and necrotic areas, both contributing to tumor expansion: the former because glioma cells use the vessel wall to travel (62), the latter because as we have seen in the PPs, tumor cells escape from the NF (156).

For both immunotherapies we also measure the spleens as an indirect assessment of the general immune state of the mice. While there was no statistically significant result, immune-treated animals tended to have a mildly smaller spleen, which can be explained by a highly phagocytic environment. This also happens in individuals with sickle cell anemia (177), thus concordant with the possible hemolytic anemia caused by our treatments. Additionally, we analyzed the cellularity, amount of Iba-1$^+$ cells and phagocytosis in all groups. Knowing the importance of the microenvironments, and Iba-1$^+$ cells seeming morphologically different in the tumor core and in the invading periphery (these results will benefit of further investigation), we decided to do the analyses taking into account these two regions. This way, we saw that cellularity was unchanged in CD47 treated animals but importantly was decreased in the tumor core (the potentially “old” part of the tumor) of animals treated against SIRP α. Probably at the tumor core, GAMMs were already in the tumor area when they received the treatment, and, if effective, started phagocytosing upon the first administration. Additionally, systemic SIRPα -blocked monocytes/macrophages may also reach the tumor recruited by the inflammatory response and be more effective engulfing glioma cells. In the case of the CD47 therapy, with the i.p. injection we could have blocked the protein in many other CD47 expressing cells such as erythrocytes, reducing the effective titre, and most probably not an enough amount of blocking antibody reached the tumor. Interestingly, no differences were seen regarding the Iba-1$^+$ cell quantification among the groups suggesting that targeting SIRP α is specifically targeting the phagocytic capacity of the cells, not their infiltration, therefore the GAMMs infiltrating the tumor may be more active and ready to phagocytose. On the other hand, in the case of CD47, myeloid cells are not reaching a sufficient phagocytic activation and are probably benefitting glioma cells with their angiogenic capacity or the remodeling of the extracellular matrix (178).

Importantly for our study, the difference in the phagocytic capacity between anti-SIRPα and anti-CD47 was spotted in the periphery of the tumor, putatively the invasive area and where the first encounter between invading tumor cells and activated or infiltrating GAMMs may happen. In all, although it remains unknown exactly how SIRP α signaling is involved in phagocytosis and its relationship with other receptors (82), we have shown an auspicious treatment against GBM.

In summary, in this thesis we have revealed particular insights on the role of GAMMs in human GBM, particularly in the invading niche of PPs, a hallmark for the most aggressive GBM, where phagocytosis frequently occurs at the necrotic borders. We have effectively visualized the interaction between microglial cells as effector cells and glioma cells as targets. We also showed how to promote microglial phagocytosis of whole glioma cells in vitro and in vivo; and described the mode of microglial/macrophages' action and the disposition of key receptors in phagocytosis. Finally, we have dissected critical differences, for the safety and effectiveness of immunotherapy, between acting on receptors on the tumor cell surface (targeting CD47) and the surface of GAMMs (targeting SIRPα), casting light in this promising intrinsic mechanism of microglia and macrophages, which is phagocytosis, to achieve the clearance this fatal brain tumor.

Conclusions

The main conclusions in this thesis are:

1. There are GAMMs in PPs in human GBM, they express CD163 while traveling to the NF, where they switch their phenotype and express MHCII.
2. GAMMs in the HA of PPs are elongated, similarly to BV-2 cells in hypoxic conditions in vitro.
3. In vitro, glioma cells (GL261) escape hypoxia while microglia (BV-2) gain cellular persistence.
4. Hypoxia and GFAP fibers may contribute to the haptotactic migration of GAMM.
5. Proximal to the NF, GAMM increase their phagocytic capacity phagocytosing even whole $GFAP^+$ cells.
6. GAMM do not translocate p65 NF-κB in human GBM.
7. LPS/IFN-γ co stimulation promotes phagocytosis of C6 glioma cells by primary rat microglia through p65 NF-κB.
8. In vitro, microglia (BV-2) are able to phagocytose both live and dead glioma cells (GL261) suggesting that phagoptosis takes place in these events.
9. CD11b and CD16/32 are highly expressed in the uropod in potentially kinetic microglial BV-2 cells.
10. CD11b and CD16/32 are highly expressed in the periphery of the interacting interface and the phagocytic cup between microglia (BV-2) and glioma ceslls (GL261 cells).
11. Intraperitoneal immunotherapy to promote phagocytosis in murine glioma is more effective when acting upon the effector cells (by blocking SIRP α) than upon target cells (CD47 neutralization).
12. SIRPα neutralization appears to be safer than CD47 neutralization in murine glioma.
13. Neutralizing antibodies against CD47 and SIRP α do not modify GAMM infiltration in vivo.
14. SIRP α neutralization promotes phagocytosis in invading areas of murine glioma and reduces cellularity in the tumor core.

Personal note on future directions:

Finally, I believe immunotherapy is a very promising option to battle GBM especially targeting the most prominent immune cell type infiltrated, the so-called GAMMs. There are always more things one can do, especially in basic science. Initially, to the person that may take over my research I would say the first five feasible things on my to-do list would be to 1) further characterize the action of both neutralizing antibodies, for instance by analyzing the translocation of p65 NF-κB in the effector cells 2) using MRI to follow the tumor growth in murine glioma after treatment; 3) analyze the location of both receptors within the phagocytic synapse as well as the effectiveness of the blocking antibodies in this scenario; 4) analyze microglial dynamics in the invading areas (periphery) and the tumor core, and 5) study in a quantitative way the phagocytic synapse formation when inducing SIRPα or CD47 blockade.

Bibliography

1. Díaz LR, Saavedra-López E, Romarate L, Mitxitorena I, Casanova P V., Cribaro GP, et al. Imbalance of immunological synapse-kinapse states reflects tumor escape to immunity in glioblastoma. JCI Insight. 2018;

2. Louis DN, Perry A, Reifenberger G, von Deimling A, Figarella-Branger D, Cavenee WK, et al. The 2016 World Health Organization Classification of Tumors of the Central Nervous System: a summary. Acta Neuropathologica. 2016.

3. Lim M, Xia Y, Bettegowda C, Weller M. Current state of immunotherapy for glioblastoma. Nature Reviews Clinical Oncology. 2018.

4. Tamimi AF, Juweid M. Epidemiology and Outcome of Glioblastoma. In: Glioblastoma. 2017.

5. Wippold FJ, Lämmle M, Anatelli F, Lennerz J, Perry A. Neuropathology for the neuroradiologist: Palisades and pseudopalisades. American Journal of Neuroradiology. 2006.

6. Walker C, Baborie A, Crooks D, Wilkins S, Jenkinson MD. Biology, genetics and imaging of glial cell tumours. Br J Radiol. 2011;84(SPEC. ISSUE 2).

7. Brat DJ, Castellano-sanchez AA, Hunter SB, Pecot M, Cohen C, Hammond EH, et al. Pseudopalisades in Glioblastoma Are Hypoxic , Express Extracellular Matrix Proteases , and Are Formed by an Actively Migrating Cell Population. Cancer Res. 2004;64:920–7.

8. Lee JH, Lee JE, Kahng JY, Kim SH, Park JS, Yoon SJ, et al. Human glioblastoma arises from subventricular zone cells with low-level driver mutations. Nature. 2018.

9. Preusser M, Lim M, Hafler DA, Reardon DA, Sampson JH. Prospects of immune checkpoint modulators in the treatment of glioblastoma. Nature Reviews Neurology. 2015.

10. Chen L, Zhang Y, Yang J, Hagan JP, Li M. Vertebrate animal models of glioma: Understanding the mechanisms and developing new therapies. Biochim Biophys Acta - Rev Cancer [Internet]. 2013;1836(1):158–65. Available from: http://dx.doi.org/10.1016/j.bbcan.2013.04.003

11. Bao S, Wu Q, McLendon RE, Hao Y, Shi Q, Hjelmeland AB, et al. Glioma stem cells promote radioresistance by preferential activation of the DNA damage response. Nature. 2006;

12. Dean M, Fojo T, Bates S. Tumour stem cells and drug resistance. Nature Reviews Cancer. 2005.

13. Skog J, Würdinger T, van Rijn S, Meijer DH, Gainche L, Curry WT, et al. Glioblastoma microvesicles transport RNA and proteins that promote tumour growth and provide diagnostic biomarkers. Nat Cell Biol. 2008;

14. Pavlyukov MS, Yu H, Bastola S, Minata M, Shender VO, Lee Y, et al. Apoptotic Cell-Derived Extracellular Vesicles Promote Malignancy of Glioblastoma Via Intercellular Transfer of Splicing Factors. Cancer Cell. 2018;

15. Bellail AC, Olson JJ, Hao C. SUMO1 modification stabilizes CDK6 protein and drives the cell cycle and glioblastoma progression. Nat Commun [Internet]. 2014;5(May):4234. Available from: http://dx.doi.org/10.1038/ncomms5234

16. Hamard L, Ratel D, Selek L, Berger F, van der Sanden B, Wion D. The brain tissue response to surgical injury and its possible contribution to glioma recurrence. Journal of Neuro-Oncology. 2016.

17. Barker CF, Billingham RE. Immunologically privileged sites. Adv Immunol. 1978;

18. Bentivoglio M, Kristensson K. Tryps and trips: Cell trafficking across the 100-year-old blood-brain barrier. Trends in Neurosciences. 2014.

19. Bechmann I, Galea I, Perry VH. What is the blood-brain barrier (not)? Trends Immunol. 2007;28(1):5–11.

20. Saunders NR, Dreifuss JJ, Dziegielewska KM, Johansson PA, Habgood MD, Møllgård K, et al. The rights and wrongs of blood-brain barrier permeability studies: A walk through 100 years of history. Frontiers in Neuroscience. 2014.

21. Ehrlich P. Das Sauerstoff-Bedürfnis des Organismus. Eine farbenanalytische Studie. [On the oxygen consumption of the body. A study using intravital dyes.]. Verlag von August Hirschwald, Berlin. 1885;

22. Weed LH. Studies on Cerebro-Spinal Fluid. No. III : The pathways of escape from the Subarachnoid Spaces with particular reference to the Arachnoid Villi. J Med Res [Internet]. 1914;31(1):51–91. Available from: http://www.ncbi.nlm.nih.gov/pubmed/19972194%0Ahttp://www.pubmedcentral.nih.gov/articlerender.fcgi?artid=PMC2094443

23. Louveau A, Smirnov I, Keyes TJ, Eccles JD, Rouhani SJ, Peske JD, et al. Structural and functional features of central nervous system lymphatic vessels. Nature. 2015;

24. Xie L, Kang H, Xu Q, Chen MJ, Liao Y, Thiyagarajan M, et al. Sleep drives metabolite clearance from the adult brain. Science (80-). 2013;

25. Yang L, Kress BT, Weber HJ, Thiyagarajan M, Wang B, Deane R, et al. Evaluating glymphatic pathway function utilizing clinically relevant intrathecal infusion of CSF tracer. J Transl Med. 2013;

26. Iliff JJ, Lee H, Yu M, Feng T, Logan J, Nedergaard M, et al. A Paravascular Pathway Facilitates CSF Flow Through the Brain Parenchyma and the Clearance of Interstitial Solutes, Including Amyloid β. Sci Transl Med. 2015;

27. Cserr HF, Harling-Berg CJ, Knopf PM. Drainage of Brain Extracellular Fluid into Blood and Deep Cervical Lymph and its Immunological Significance. Brain Pathology. 1992.

28. Schetters STT, Gomez-Nicola D, Garcia-Vallejo JJ, Van Kooyk Y. Neuroinflammation: Microglia and T cells get ready to tango. Front Immunol. 2018;

29. Jones KA, Maltby S, Plank MW, Kluge M, Nilsson M, Foster PS, et al. Peripheral immune cells infiltrate into sites of secondary neurodegeneration after ischemic stroke. Brain Behav Immun. 2018;

30. Mrdjen D, Pavlovic A, Hartmann FJ, Schreiner B, Utz SG, Leung BP, et al. High-Dimensional Single-Cell Mapping of Central Nervous System Immune Cells Reveals Distinct Myeloid Subsets in Health, Aging, and Disease. Immunity. 2018;

31. Ousman SS, Kubes P. Immune surveillance in the central nervous system. Nature

Neuroscience. 2012.

32. Kipnis J. Multifaceted interactions between adaptive immunity and the central nervous system. Science. 2016.

33. Morimura T, Neuchrist C, Kitz K, Budka H, Scheiner O, Kraft D, et al. Monocyte subpopulations in human gliomas: Expression of Fc and complement receptors and correlation with tumor proliferation. Acta Neuropathol. 1990;

34. Hambardzumyan D, Gutmann DH, Kettenmann H. The role of microglia and macrophages in glioma maintenance and progression. Nat Neurosci [Internet]. 2015;19(1):20–7. Available from: http://www.nature.com/doifinder/10.1038/nn.4185

35. Han S, Zhang C, Li Q, Dong J, Liu Y, Huang Y, et al. Tumour-infiltrating CD4+ and CD8+ lymphocytes as predictors of clinical outcome in glioma. Br J Cancer [Internet]. 2014;110(10):2560–8. Available from: http://www.nature.com/doifinder/10.1038/bjc.2014.162

36. Ginhoux F, Garel S. The mysterious origins of microglia. Nat Neurosci. 2018;

37. Li Q, Barres BA. Microglia and macrophages in brain homeostasis and disease. Nature Reviews Immunology. 2018.

38. Monier A, Adle-Biassette H, Delezoide A-L, Evrard P, Gressens P, Verney C. Entry and Distribution of Microglial Cells in Human Embryonic and Fetal Cerebral Cortex. J Neuropathol Exp Neurol. 2007;

39. McGrath KE, Koniski AD, Malik J, Palis J. Circulation is established in a stepwise pattern in the mammalian embryo. Blood. 2003;

40. Nimmerjahn A, Kirchhoff F, Helmchen F. Resting microglial cells are highly dynamic surveillants of brain parenchyma in vivo. Neuroforum. 2005;11(3):95–6.

41. Chen Z, Feng X, Herting CJ, Garcia VA, Nie K, Pong WW, et al. Cellular and molecular identity of tumor-associated macrophages in glioblastoma. Cancer Res. 2017;

42. Rock RB, Hu S, Deshpande A, Munir S, May BJ, Baker CA, et al. Transcriptional response of human microglial cells to interferon-γ. Genes Immun. 2005;

43. Sethna MP, Lampson LA. Immune modulation within the brain: recruitment of inflammatory cells and increased major histocompatibility antigen expression following intracerebral injection of interferon-γ. J Neuroimmunol. 1991;

44. Stein M. Interleukin 4 potently enhances murine macrophage mannose receptor activity: a marker of alternative immunologic macrophage activation. J Exp Med. 1992;

45. Lund H, Pieber M, Parsa R, Han J, Grommisch D, Ewing E, et al. Competitive repopulation of an empty microglial niche yields functionally distinct subsets of microglia-like cells. Nat Commun [Internet]. 2018;9(4845). Available from: https://www.ncbi.nlm.nih.gov/pmc/articles/PMC6242869/

46. Sierra A, Abiega O, Shahraz A, Neumann H. Janus-faced microglia: beneficial and detrimental consequences of microglial phagocytosis. Front Cell Neurosci. 2013;

47. Lavin Y, Winter D, Blecher-Gonen R, David E, Keren-Shaul H, Merad M, et al. Tissue-resident macrophage enhancer landscapes are shaped by the local microenvironment. Cell. 2014;

48. Müller A, Brandenburg S, Turkowski K, Müller S, Vajkoczy P. Resident microglia, and not peripheral macrophages, are the main source of brain tumor mononuclear cells. Int J Cancer. 2015;

49. Cronk JC, Filiano AJ, Louveau A, Marin I, Marsh R, Ji E, et al. Peripherally derived macrophages can engraft the brain independent of irradiation and maintain an identity distinct from microglia. J Exp Med [Internet]. 2018;jem.20180247. Available from: http://www.ncbi.nlm.nih.gov/pubmed/29643186

50. Yang I, Han SJ, Kaur G, Crane C, Parsa AT. The role of microglia in central nervous system immunity and glioma immunology. Journal of Clinical Neuroscience. 2010.

51. Neumann H, Kotter MR, Franklin RJM. Debris clearance by microglia: An essential link between degeneration and regeneration. Brain. 2009.

52. Bayerl SH, Niesner R, Cseresnyes Z, Radbruch H, Pohlan J, Brandenburg S, et al. Time lapse in vivo microscopy reveals distinct dynamics of microglia-tumor environment interactions-a new role for the tumor perivascular space as highway for trafficking microglia. Glia. 2016;

53. Hanisch UK, Kettenmann H. Microglia: Active sensor and versatile effector cells in the normal and pathologic brain. Nature Neuroscience. 2007.

54. Li W, Graeber MB. The molecular profile of microglia under the influence of glioma [Internet]. Vol. 14, Neuro-Oncology. 2012. p. 958–78. Available from: http://neuro-oncology.oxfordjournals.org/cgi/doi/10.1093/neuonc/nos116

55. Goodridge HS, Reyes CN, Becker CA, Katsumoto TR, Ma J, Wolf AJ, et al. Activation of the innate immune receptor Dectin-1 upon formation of a ˜ Phagocytic synapse-™. Nature. 2011;

56. Neumann J, Sauerzweig S, Ronicke R, Gunzer F, Dinkel K, Ullrich O, et al. Microglia Cells Protect Neurons by Direct Engulfment of Invading Neutrophil Granulocytes: A New Mechanism of CNS Immune Privilege. J Neurosci. 2008;

57. Mills CD, Kincaid K, Alt JM, Heilman MJ, Hill AM. M-1/M-2 Macrophages and the Th1/Th2 Paradigm. J Immunol. 2000;

58. Mantovani A, Sica A, Sozzani S, Allavena P, Vecchi A, Locati M. The chemokine system in diverse forms of macrophage activation and polarization. Trends in Immunology. 2004.

59. Porta C, Rimoldi M, Raes G, Brys L, Ghezzi P, Di Liberto D, et al. Tolerance and M2 (alternative) macrophage polarization are related processes orchestrated by p50 nuclear factor B. Proc Natl Acad Sci. 2009;

60. Zwadlo G, Voegeli R, Oslhoff KS, Sorg C. A monoclonal antibody to a novel differentiation antigen on human macrophages associated with the down-regulatory phase of the inflammatory process. Pathobiology. 1987;

61. Yang M, McKay D, Pollard JW, Lewis CE. Diverse functions of macrophages in different tumor microenvironments. Cancer Research. 2018.

62. Watkins S, Robel S, Kimbrough IF, Robert SM, Ellis-Davies G, Sontheimer H. Disruption of astrocyte-vascular coupling and the blood-brain barrier by invading glioma cells. Nat Commun. 2014;

63. Dalton DK, Pitts-Meek S, Keshav S, Figari IS, Bradley A, Stewart TA. Multiple defects of

immune cell function in mice with disrupted interferon-γ genes. Science (80-). 1993;

64. Hitchcock PJ, Leive L, Makela PH, Rietschel ET, Strittmatter W, Morrison DC. Lipopolysaccharide nomenclature - past, present, and future. Journal of Bacteriology. 1986.

65. Yang F, Tang E, Guan K, Wang C-Y. IKK Plays an Essential Role in the Phosphorylation of RelA/p65 on Serine 536 Induced by Lipopolysaccharide. J Immunol. 2003;

66. Ren S, Zhang S, Li M, Huang C, Liang R, Jiang A, et al. NF-κB p65 and c-Rel subunits promote phagocytosis and cytokine secretion by splenic macrophages in cirrhotic patients with hypersplenism. Int J Biochem Cell Biol. 2013;

67. Zeiner PS, Preusse C, Blank AE, Zachskorn C, Baumgarten P, Caspary L, et al. MIF Receptor CD74 is Restricted to Microglia/Macrophages, Associated with a M1-Polarized Immune Milieu and Prolonged Patient Survival in Gliomas. Brain Pathol. 2015;

68. Doyle SE, O'Connell RM, Miranda GA, Vaidya SA, Chow EK, Liu PT, et al. Toll-like Receptors Induce a Phagocytic Gene Program through p38. J Exp Med. 2004;

69. Kong L, Ge BX. MyD88-independent activation of a novel actin-Cdc42/Rac pathway is required for Toll-like receptor-stimulated phagocytosis. Cell Res. 2008;

70. Hibbs JB, Taintor RR, Chapman HA, Weinberg JB. Macrophage tumor killing: Influence of the local environment. Science (80-). 1977;

71. Kopatz J, Beutner C, Welle K, Bodea LG, Reinhardt J, Claude J, et al. Siglec-h on activated microglia for recognition and engulfment of glioma cells. Glia. 2013;61(7):1122–33.

72. Savill J, Dransfield I, Gregory C, Haslett C. A blast from the past: Clearance of apoptotic cells regulates immune responses. Nature Reviews Immunology. 2002.

73. Kettenmann H, Kirchhoff F, Verkhratsky A. Microglia: New Roles for the Synaptic Stripper. Neuron. 2013.

74. Galambos R. A glia-neural theroy of brain function. Proc Natl Acad Sci U S A. 1960;

75. Sobota A, Strzelecka-Kiliszek A, G adkowska E, Yoshida K, Mrozinska K, Kwiatkowska K. Binding of IgG-Opsonized Particles to Fc R Is an Active Stage of Phagocytosis That Involves Receptor Clustering and Phosphorylation. J Immunol. 2005;

76. DiLillo DJ, Ravetch J V. Fc-Receptor Interactions Regulate Both Cytotoxic and Immunomodulatory Therapeutic Antibody Effector Functions. Cancer Immunol Res. 2015;

77. Flannagan RS, Jaumouillé V, Grinstein S. The Cell Biology of Phagocytosis. Annu Rev Pathol Mech Dis. 2012;

78. Lopes FB, Bálint Š, Valvo S, Felce JH, Hessel EM, Dustin ML, et al. Membrane nanoclusters of FcγRI segregate from inhibitory SIRPα upon activation of human macrophages. J Cell Biol. 2017;

79. Jongstra-Bilen J, Harrison R, Grinstein S. Fcγ-receptors Induce Mac-1 (CD11b/CD18) Mobilization and Accumulation in the Phagocytic Cup for Optimal Phagocytosis. J Biol Chem. 2003;

80. Griffin FM, Griffin JA, Leider JE, Silverstein SC. Studies on the mechanism of phagocytosis. I. Requirements for circumferential attachment of particle-bound ligands to specific receptors

on the macrophage plasma membrane. J Exp Med. 1975;

81. Flannagan RS, Harrison RE, Yip CM, Jaqaman K, Grinstein S. Dynamic macrophage “probing” is required for the efficient capture of phagocytic targets. J Cell Biol. 2010;

82. Morioka S, Maueröder C, Ravichandran KS. Living on the Edge: Efferocytosis at the Interface of Homeostasis and Pathology. Immunity. 2019.

83. Caron E, Hall A. Identification of two distinct mechanisms of phagocytosis controlled by different Rho GTPases. Science (80-). 1998;

84. Freeman SA, Grinstein S. Phagocytosis: Receptors, signal integration, and the cytoskeleton. Immunol Rev. 2014;

85. Barcia C, Ros CM, Annese V, Carrillo-de Sauvage MA, Ros-Bernal F, Gómez A, et al. ROCK/Cdc42-mediated microglial motility and gliapse formation lead to phagocytosis of degenerating dopaminergic neurons in vivo. Sci Rep [Internet]. 2012;2:809. Available from: http://www.pubmedcentral.nih.gov/articlerender.fcgi?artid=3492875&tool=pmcentrez&rendertype=abstract

86. Ostrowski PP, Grinstein S, Freeman SA. Diffusion Barriers, Mechanical Forces, and the Biophysics of Phagocytosis. Developmental Cell. 2016.

87. Worth RG, Mayo-Bond L, van de Winkel JG, Todd 3rd RF, Petty HR. CR3 (alphaM beta2; CD11b/CD18) restores IgG-dependent phagocytosis in transfectants expressing a phagocytosis-defective Fc gammaRIIA (CD32) tail-minus mutant. J Immunol. 1996;

88. Krauss JC, Poo H, Xue W, Mayo-bond L, Pettyzt HR, Ill FT, et al. Reconstitution of antibody-dependent phagocytosis in fibroblasts expressing Fc gamma receptor IIIB and the complement receptor type 3. J Immunol. 1994;

89. Getahun A, Cambier JC. Of ITIMs, ITAMs, and ITAMis: Revisiting immunoglobulin Fc receptor signaling. Immunological Reviews. 2015.

90. Wang AVT, Scholl PR, Geha RS. PHYSICAL AND FUNCTIONAL ASSOCIATION OF THE HIGH-AFFINITY IMMUNOGLOBULIN-G RECEPTOR (FC-GAMMA-RI) WITH THE KINASES HCK AND LYN. J Exp Med. 1994;

91. Ghazizadeh S, Bolen JB, Fleit HB. Physical and functional association of Src-related protein tyrosine kinases with FcγRII in monocytic THP-1 cells. J Biol Chem. 1994;

92. Hamada F, Aoki M, Akiyama T, Toyoshima K. Association of immunoglobulin G Fc receptor II with Src-like protein-tyrosine kinase Fgr in neutrophils. Proc Natl Acad Sci. 1993;

93. Fitzer-Attas CJ, Lowry M, Crowley MT, Finn AJ, Meng F, DeFranco AL, et al. Fcγ Receptor–Mediated Phagocytosis in Macrophages Lacking the Src Family Tyrosine Kinases Hck, Fgr, and Lyn. J Exp Med. 2000;

94. Park JG, Schreiber AD. Determinants of the phagocytic signal mediated by the type IIIA Fc gamma receptor, Fc gamma RIIIA: sequence requirements and interaction with protein-tyrosine kinases. Proc Natl Acad Sci U S A. 1995;

95. Greenberg S, Chang P, Silverstein SC. Tyrosine phosphorylation of the γ subunit of Fc(γ) receptors, p72(syk), and paxillin during Fc receptor-mediated phagocytosis in macrophages. J Biol Chem. 1994;

96. Jouvin MHE, Adamczewski M, Numerof R, Letourneur O, Vallé A, Kinet JP. Differential control of the tyrosine kinases Lyn and Syk by the two signaling chains of the high affinity immunoglobulin E receptor. J Biol Chem. 1994;

97. Kusner DJ, Hall CF, Jackson S. Phagocytosis of IgG-Opsonized Particles Phospholipase D Regulates Macrophage Receptor-Mediated Activation of γ Fc Fc⁄⁄ Receptor-Mediated Activation of Phospholipase D Regulates Macrophage Phagocytosis of IgG-Opsonized Particles. J Immunol. 1999;

98. Iyer SS, Barton JA, Bourgoin S, Kusner DJ. Phospholipases D1 and D2 Coordinately Regulate Macrophage Phagocytosis. J Immunol. 2004;

99. Tsai RK, Discher DE. Inhibition of "self" engulfment through deactivation of myosin-II at the phagocytic synapse between human cells. J Cell Biol. 2008;

100. Hajishengallis G, Reis ES, Mastellos DC, Ricklin D, Lambris JD. Novel mechanisms and functions of complement. Nature Immunology. 2017.

101. Guo R-F, Ward PA. ROLE OF C5A IN INFLAMMATORY RESPONSES. Annu Rev Immunol. 2005;

102. Ricklin D, Hajishengallis G, Yang K, Lambris JD. Complement: A key system for immune surveillance and homeostasis. Nature Immunology. 2010.

103. Schmidt CQ, Lambris JD, Ricklin D. Protection of host cells by complement regulators. Immunological Reviews. 2016.

104. Kim SH, Carney DF, Hammer CH, Shin ML. Nucleated cell killing by complement: effects of C5b-9 channel size and extracellular Ca2+ on the lytic process. J Immunol. 1987;

105. Zhou MJ, Brown EJ. CR3 (Mac-1, αMβ2, CD11b/CD18) and FcγRIII cooperate in generation of a neutrophil respiratory burst: Requirement for FcγRII and tyrosine phosphorylation. J Cell Biol. 1994;

106. Brown GC, Neher JJ. Microglial phagocytosis of live neurons. Nat Publ Gr [Internet]. 2014;15(4):209–16. Available from: http://dx.doi.org/10.1038/nrn3710%5Cnpapers2://publication/doi/10.1038/nrn3710

107. Barth ND, Marwick JA, Vendrell M, Rossi AG, Dransfield I. The "Phagocytic synapse" and clearance of apoptotic cells. Frontiers in Immunology. 2017.

108. Ravichandran KS. Find-me and eat-me signals in apoptotic cell clearance: progress and conundrums. J Exp Med. 2010;

109. Roerdink F, Wassef NM, Richardson EC, Alving CR. Effects of negatively charged lipids on phagocytosis of liposomes opsonized by complement. BBA - Biomembr. 1983;

110. Yeung T, Terebiznik M, Yu L, Silvius J, Abidi WM, Philips M, et al. Receptor activation alters inner surface potential during phagocytosis. Science (80-). 2006;

111. Vernon-Wilson EF, Aurade F, Tian L, Rowe ICM, Shipston MJ, Savill J, et al. CD31 delays phagocyte membrane repolarization to promote efficient binding of apoptotic cells. J Leukoc Biol. 2007;

112. Dupuy AG, Caron E. Integrin-dependent phagocytosis - spreading from microadhesion to new concepts. J Cell Sci. 2008;

113. Rougerie P, Miskolci V, Cox D. Generation of membrane structures during phagocytosis and chemotaxis of macrophages: Role and regulation of the actin cytoskeleton. Immunol Rev. 2013;

114. Rosales C, Uribe-Querol E. Phagocytosis: A Fundamental Process in Immunity. BioMed Research International. 2017.

115. Ueda M, Graf R, MacWilliams HK, Schliwa M, Euteneuer U. Centrosome positioning and directionality of cell movements. Proc Natl Acad Sci. 1997;

116. Monks CRF, Freiberg BA, Kupfer H, Sciaky N, Kupfer A. Three-dimensional segregation of supramolecular activation clusters in T cells. Nature. 1998;

117. Grakoui A, Bromley SK, Sumen C, Davis MM, Shaw AS, Allen PM, et al. The immunological synapse: A molecular machine controlling T cell activation. Science (80-). 1999;

118. Koh E, Lee EJ, Nam GH, Hong Y, Cho E, Yang Y, et al. Exosome-SIRPα, a CD47 blockade increases cancer cell phagocytosis. Biomaterials [Internet]. 2017;121:121–9. Available from: http://dx.doi.org/10.1016/j.biomaterials.2017.01.004

119. Oldenborg P-A, Gresham HD, Lindberg FP. Cd47-Signal Regulatory Protein α (Sirpα) Regulates Fcγ and Complement Receptor–Mediated Phagocytosis. J Exp Med. 2001;

120. Nayak D, Roth TL, McGavern DB. Microglia Development and Function*. Annu Rev Immunol [Internet]. 2014;32(1):367–402. Available from: http://www.annualreviews.org/doi/abs/10.1146/annurev-immunol-032713-120240

121. Barkal AA, Weiskopf K, Kao KS, Gordon SR, Rosental B, Yiu YY, et al. Engagement of MHC class i by the inhibitory receptor LILRB1 suppresses macrophages and is a target of cancer immunotherapy article. Nat Immunol. 2018;19(1):76–84.

122. Dheilly E, Moine V, Broyer L, Salgado-Pires S, Johnson Z, Papaioannou A, et al. Selective Blockade of the Ubiquitous Checkpoint Receptor CD47 Is Enabled by Dual-Targeting Bispecific Antibodies. Mol Ther [Internet]. 2017;25(2):523–33. Available from: http://dx.doi.org/10.1016/j.ymthe.2016.11.006

123. McCracken MN, Cha AC, Weissman IL. Molecular pathways: Activating T cells after cancer cell phagocytosis from blockade of CD47 “Don’t eat Me” signals. Clin Cancer Res. 2015;

124. Piccione EC, Juarez S, Tseng S, Liu J, Stafford M, Narayanan C, et al. SIRPα-antibody fusion proteins selectively bind and eliminate dual antigen-expressing tumor cells. Clin Cancer Res. 2016;

125. Oldenborg PA, Zheleznyak A, Fang YF, Lagenaur CF, Gresham HD, Lindberg FP. Role of CD47 as a marker of self on red blood cells. Science (80-). 2000;

126. Schürch CM, Forster S, Brühl F, Yang SH, Felley-Bosco E, Hewer E. The “don’t eat me” signal CD47 is a novel diagnostic biomarker and potential therapeutic target for diffuse malignant mesothelioma. OncoImmunology. 2017;

127. Gholamin S, Mitra SS, Feroze AH, Liu J, Kahn SA, Zhang M, et al. Disrupting the CD47-SIRPα anti-phagocytic axis by a humanized anti-CD47 antibody is an efficacious treatment for malignant pediatric brain tumors. Sci Transl Med. 2017;9(381).

128. Liu X, Pu Y, Cron K, Deng L, Kline J, Frazier W a, et al. CD47 blockade triggers T cell–mediated

destruction of immunogenic tumors. Nat Med [Internet]. 2015;21(10):1209–15. Available from: http://dx.doi.org/10.1038/nm.3931

129. Ingram JR, Blomberg OS, Sockolosky JT, Ali L, Schmidt FI, Pishesha N, et al. Localized CD47 blockade enhances immunotherapy for murine melanoma. Proc Natl Acad Sci. 2017;

130. Vonderheide RH. CD47 blockade as another immune checkpoint therapy for cancer. Nat Med [Internet]. 2015;21(10):1122–1123. Available from: http://www.nature.com/doifinder/10.1038/nm.3965

131. Matlung HL, Szilagyi K, Barclay NA, van den Berg TK. The CD47-SIRPα signaling axis as an innate immune checkpoint in cancer. Immunological Reviews. 2017.

132. Malo CS, Huggins MA, Goddery EN, Tolcher HMA, Renner DN, Jin F, et al. Non-equivalent antigen presenting capabilities of dendritic cells and macrophages in generating brain-infiltrating CD8+T cell responses. Nat Commun. 2018;

133. Ziv Y, Ron N, Butovsky O, Landa G, Sudai E, Greenberg N, et al. Immune cells contribute to the maintenance of neurogenesis and spatial learning abilities in adulthood. Nat Neurosci. 2006;

134. Barcia C, Thomas CE, Curtin JF, King GD, Wawrowsky K, Candolfi M, et al. In vivo mature immunological synapses forming SMACs mediate clearance of virally infected astrocytes from the brain. J Exp Med. 2006;

135. Barcia C, Gómez A, Gallego-Sanchez JM, Perez-Vallés A, Castro MG, Lowenstein PR, et al. Infiltrating CTLs in human glioblastoma establish immunological synapses with tumorigenic cells. Am J Pathol [Internet]. 2009;175(2):786–98. Available from: http://www.pubmedcentral.nih.gov/articlerender.fcgi?artid=2716973&tool=pmcentrez&rendertype=abstract

136. Smolders J, Heutinck KM, Fransen NL, Remmerswaal EBM, Hombrink P, ten Berge IJM, et al. Tissue-resident memory T cells populate the human brain. Nat Commun. 2018;

137. Azar GA, Lemaitre F, Robey EA, Bousso P. Subcellular dynamics of T cell immunological synapses and kinapses in lymph nodes. Proc Natl Acad Sci. 2010;

138. Norcross MA. A synaptic basis for T-lymphocyte activation. Ann l'Institut Pasteur - Immunol. 1984;

139. Kupfer A. Signaling in the Immunological Synapse: Defining the Optimal Size. Immunity. 2006.

140. Mitxitorena I, Saavedra E, Barcia C. Kupfer-type immunological synapses in vivo: Raison D'être of SMAC. Immunol Cell Biol [Internet]. 2015;93(1):51–6. Available from: http://www.ncbi.nlm.nih.gov/pubmed/25267483

141. Sharpe AH, Freeman GJ. The B7-CD28 superfamily. Nature Reviews Immunology. 2002.

142. Griffiths GM, Tsun A, Stinchcombe JC. The immunological synapse: A focal point for endocytosis and exocytosis. Journal of Cell Biology. 2010.

143. Ikemizu S, Gilbert RJC, Fennelly JA, Collins A V., Harlos K, Jones EY, et al. Structure and dimerization of a soluble form of B7-1. Immunity. 2000;

144. Pentcheva-Hoang T, Egen JG, Wojnoonski K, Allison JP. B7-1 and B7-2 selectively recruit CTLA-4 and CD28 to the immunological synapse. Immunity. 2004;

145. Chaudhri A, Xiao Y, Klee AN, Wang X, Zhu B, Freeman GJ. PD-L1 Binds to B7-1 Only *In Cis* on the Same Cell Surface. Cancer Immunol Res. 2018;

146. Buchbinder EI, Desai A. CTLA-4 and PD-1 pathways similarities, differences, and implications of their inhibition. American Journal of Clinical Oncology: Cancer Clinical Trials. 2016.

147. Motzer RJ, Tannir NM, McDermott DF, Arén Frontera O, Melichar B, Choueiri TK, et al. Nivolumab plus Ipilimumab Versus Sunitinib in Advanced Renal-cell Carcinoma. N Engl J Med. 2018;378(14):1277–90.

148. Sims JS, Grinshpun B, Feng Y, Ung TH, Neira JA, Samanamud JL, et al. Diversity and divergence of the glioma-infiltrating T-cell receptor repertoire. Proc Natl Acad Sci. 2016;

149. Griess P. Bemerkungen zu der Abhandlung der HH. Weselsky und Benedikt „Ueber einige Azoverbindungen". Berichte der Dtsch Chem Gesellschaft. 1879;

150. Grisham MB, Johnson GG, Lancaster JR. Quantitation of nitrate and nitrite in extracellular fluids. In 1996. p. 237–46. Available from: https://linkinghub.elsevier.com/retrieve/pii/S0076687996680264

151. Nemere I, Kupfer A, Singer SJ. Reorientation of the golgi apparatus and the microtubule-organizing center inside macrophages subjected to a chemotactic gradient. Cell Motil. 1985;

152. Etienne-Manneville S. Actin and microtubules in cell motility: Which one is in control? Traffic. 2004.

153. Hale CM, Chen W-C, Khatau SB, Daniels BR, Lee JSH, Wirtz D. SMRT analysis of MTOC and nuclear positioning reveals the role of EB1 and LIC1 in single-cell polarization. J Cell Sci. 2011;

154. Li F, Lv B, Liu Y, Hua T, Han J, Sun C, et al. Blocking the CD47-SIRPα axis by delivery of anti-CD47 antibody induces antitumor effects in glioma and glioma stem cells. Oncoimmunology. 2018;

155. Saavedra-Lopez E, Roig-Martinez M, Cribaro GP, Casanova P V., Gallego-Sanchez JM, Perez-Vallés A, et al. Phagocytic glioblastoma-associated microglia and macrophages populate invading pseudopalisades. Brain Commun.

156. Brat DJ, Castellano-Sanchez AA, Hunter SB, Pecot M, Cohen C, Hammond EH, et al. Pseudopalisades in Glioblastoma Are Hypoxic, Express Extracellular Matrix Proteases, and Are Formed by an Actively Migrating Cell Population. Cancer Res. 2004;64(3):920–7.

157. Oudin MJ, Jonas O, Kosciuk T, Broye LC, Guido BC, Wyckoff J, et al. Tumor cell–driven extracellular matrix remodeling drives haptotaxis during metastatic progression. Cancer Discov. 2016;

158. Pierallini A, Bonamini M, Pantano P, Palmeggiani F, Raguso M, Osti MF, et al. Radiological assessment of necrosis in glioblastoma: Variability and prognostic value. Neuroradiology. 1998;

159. Calabrese C, Poppleton H, Kocak M, Hogg TL, Fuller C, Hamner B, et al. A Perivascular Niche for Brain Tumor Stem Cells. Cancer Cell. 2007;

160. Poligone B, Baldwin AS. Positive and Negative Regulation of NF-κB by COX-2. J Biol Chem. 2001;

161. Martinez FO, Gordon S. The M1 and M2 paradigm of macrophage activation: time for

reassessment. F1000Prime Rep. 2014;

162. Shen X, Burguillos MA, Osman AM, Frijhoff J, Carrillo-Jiménez A, Kanatani S, et al. Glioma-induced inhibition of caspase-3 in microglia promotes a tumor-supportive phenotype. Nat Immunol. 2016;17(11):1282–90.

163. Brodie C, Goldreich N, Haiman T, Kazimirsky G. Functional IL-4 receptors on mouse astrocytes: IL-4 inhibits astrocyte activation and induces NGF secretion. J Neuroimmunol. 1998;

164. Rizzi C, Tiberi A, Giustizieri M, Marrone MC, Gobbo F, Carucci NM, et al. NGF steers microglia toward a neuroprotective phenotype. Glia. 2018;

165. Pacheco P, White D, Sulchek T. Effects of microparticle size and Fc density on macrophage phagocytosis. PLoS One. 2013;

166. Sambrano GR, Steinberg D. Recognition of oxidatively damaged and apoptotic cells by an oxidized low density lipoprotein receptor on mouse peritoneal macrophages: role of membrane phosphatidylserine. Proc Natl Acad Sci. 2006;

167. Ehlenberger AG. The role of membrane receptors for C3b and C3d in phagocytosis. J Exp Med. 1977;

168. Schulz D, Severin Y, Zanotelli VRT, Bodenmiller B. In-Depth Characterization of Monocyte-Derived Macrophages using a Mass Cytometry-Based Phagocytosis Assay. Sci Rep. 2019;

169. Herter S, Birk MC, Klein C, Gerdes C, Umana P, Bacac M. Glycoengineering of Therapeutic Antibodies Enhances Monocyte/Macrophage-Mediated Phagocytosis and Cytotoxicity. J Immunol. 2014;

170. Indik ZK, Park JG, Hunter S, Mantaring M, Schreiber AD. Molecular dissection of Fcγ receptor-mediated phagocytosis. Immunol Lett. 1995;

171. Lukácsi S, Nagy-Baló Z, Erdei A, Sándor N, Bajtay Z. The role of CR3 (CD11b/CD18) and CR4 (CD11c/CD18) in complement-mediated phagocytosis and podosome formation by human phagocytes. Immunol Lett. 2017;

172. Imai Y, Kohsaka S. Intracellular signaling in M-CSF-induced microglia activation: Role of Iba1. GLIA. 2002.

173. Ohsawa K, Imai Y, Sasaki Y, Kohsaka S. Microglia/macrophage-specific protein Iba1 binds to fimbrin and enhances its actin-bundling activity. J Neurochem. 2004;

174. Zhu H, Yang N, Leiss L, Rygh CB, Enger PØ, Bjerkvig R, et al. CD47 antibody inhibits tumor recurrence in a clinical relevant glioblastoma animal model. J Immunother Cancer. 2015;

175. Bronte V, Pittet MJ. The spleen in local and systemic regulation of immunity. Immunity. 2013.

176. Cribaro GP. Three-dimensional atlas of vascular networks in human glioblastoma . Universitat Autònoma de Barcelona; 2018.

177. Yildiz AE, Ariyurek MO, Karcaaltincaba M. Splenic Anomalies of Shape, Size, and Location: Pictorial Essay. Sci World J. 2013;

178. Roesch S, Rapp C, Dettling S, Herold-Mende C. When immune cells turn bad—tumor-associated microglia/macrophages in glioma. International Journal of Molecular Sciences. 2018.

Supplementary tables

Table 1. Vimentin correlations and liner regressions

	Iba1					MHCII					CD163				
	Correlation		Linear regression			Correlation		Linear regression			Correlation		Linear regression		
Microenvironment	r	p	Equation	R^2	p	r	p	Equation	R^2	p	r	p	Equation	R^2	p
Total	0.2000	0.7139	Y = 0.5998*X + 31.45	0.1551	0.4398	0.3143	0.5639	Y = 2.135*X + 30.71	0.1244	0.4928	0.6571	0.1750	Y = 1.468*X + 11.57	0.4996	0.1163
Parenchyma	0.4928	0.3444	Y = 0.4381*X + 32.46	0.0643	0.6279	0.4058	0.4333	Y = 3.630*X + 22.82	0.2055	0.3666	0.8407	0.0444	Y = 1.292*X + 6.450	0.3068	0.2541
Vascular	-0.8286	0.0583	Y = -1.042*X + 40.67	0.1920	0.3848	-0.2571	0.6583	Y = -0.4892*X + 46.38	0.0176	0.8022	0.6571	0.1750	Y = 1.637*X + 14.61	0.5840	0.0768
Necrosis	-0.3591	0.5000	Y = 1.360*X + 21.06	0.1646	0.4980	0.3189	0.5500	Y = 2.038*X + 31.63	0.2162	0.3527	-0.0289	0.9330	Y = 0.1979*X + 12.05	0.0325	0.7324

Table 2. Ki67 correlations and linear regressions

	Iba1					MHCII					CD163				
	Correlation		Linear regression			Correlation		Linear regression			Correlation		Linear regression		
Microenvironment	r	p	Equation	R^2	p	r	p	Equation	R^2	p	r	p	Equation	R^2	p
Total	0.6768	0.1556	Y = 0.1432*X + 29.51	0.3922	0.1834	0.4708	0.3444	Y = 0.3479*X + 28.11	0.1466	0.4538	0.0	0.9778	Y = 0.1065*X + 13.32	0.1167	0.5075
Parenchyma	0.4030	0.4444	Y = 0.08214*X + 31.64	0.1002	0.5410	0.5224	0.2889	Y = 0.5393*X + 19.79	0.2012	0.3722	-0.0149	0.9778	Y = 0.07671*X + 8.444	0.0480	0.6767
Vascular	-0.0883	0.8444	Y = -0.1514*X + 41.44	0.1796	0.4024	-0.4414	0.3444	Y = -0.2244*X + 50.83	0.1641	0.4255	0.0	0.9778	Y = 0.1367*X + 16.08	0.1808	0.4007
Necrosis	0.7030	0.2667	Y = 0.4000*X + 13.80	0.4979	0.1830	0.3135	0.600	Y = 0.2679*X + 30.86	0.1658	0.4230	-0.4926	0.2889	Y = -0.03025*X + 13.96	0.0367	0.7161

Appendices

Appendix 1

The human tumors were extracted in the General Hospital of Valencia and had the following characteristics:

Table 3. Tumor observations from the General Hospital of Valencia

Patient no.	Date of resection	Ki-67 (%)	Localization (lobe)	Observations (size, others)
1	05/05/2011	30	Left temporal	Medium.
2	08/04/2011	20	Left frontal	Big, relapse.
3	05/07/2011	20	Left parietal	Small
4	21/01/2011	30	Left temporal	Big.
5	17/11/2009	10	Right temporal + frontal	Big
6	08/01/2010	>50	Right temporal + frontal	Medium

Appendix 2

JCI insight

Imbalance of immunological synapse-kinapse states reflects tumor escape to immunity in glioblastoma

Laura R. Díaz,[1,2] Elena Saavedra-López,[1,2] Leire Romarate,[1,2] Izaskun Mitxitorena,[1,2] Paola V. Casanova,[1,2] George P. Cribaro,[1,2] José M. Gallego,[3] Ana Pérez-Vallés,[4] Jerónimo Forteza-Vila,[5] Clara Alfaro-Cervello,[6] José M. García-Verdugo,[6] Carlos Barcia Sr.,[3] and Carlos Barcia Jr.[1,2]

JCI Insight. 2018;3(18):e120757. https://doi.org/10.1172/jci.insight.120757.

Immunology Graphical abstract

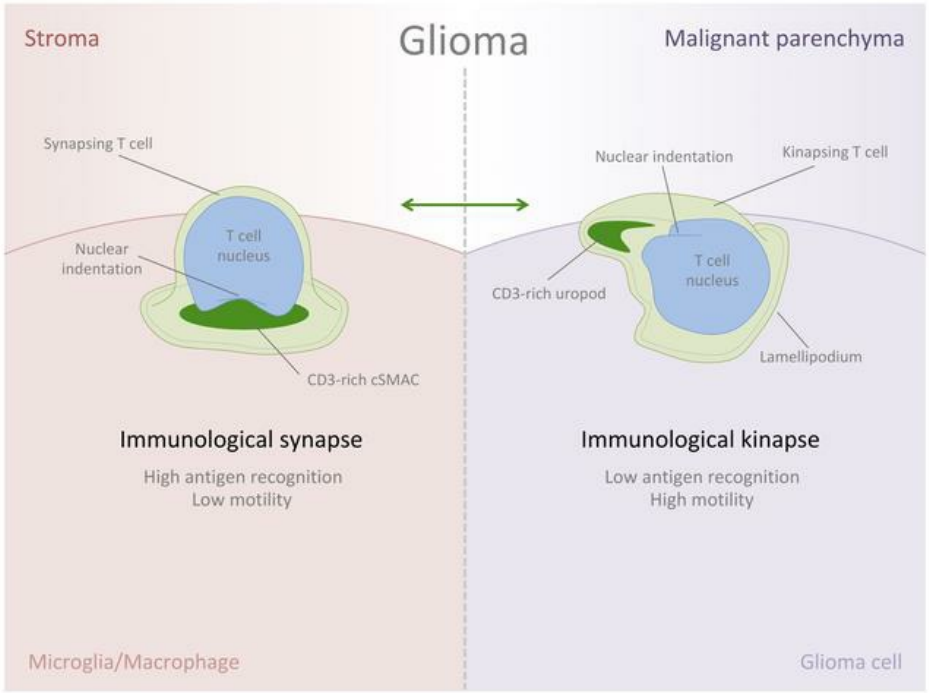

Find the latest version:

http://jci.me/120757/pdf